Joule

CellPress

Article

Wind power production from very large offshore wind farms

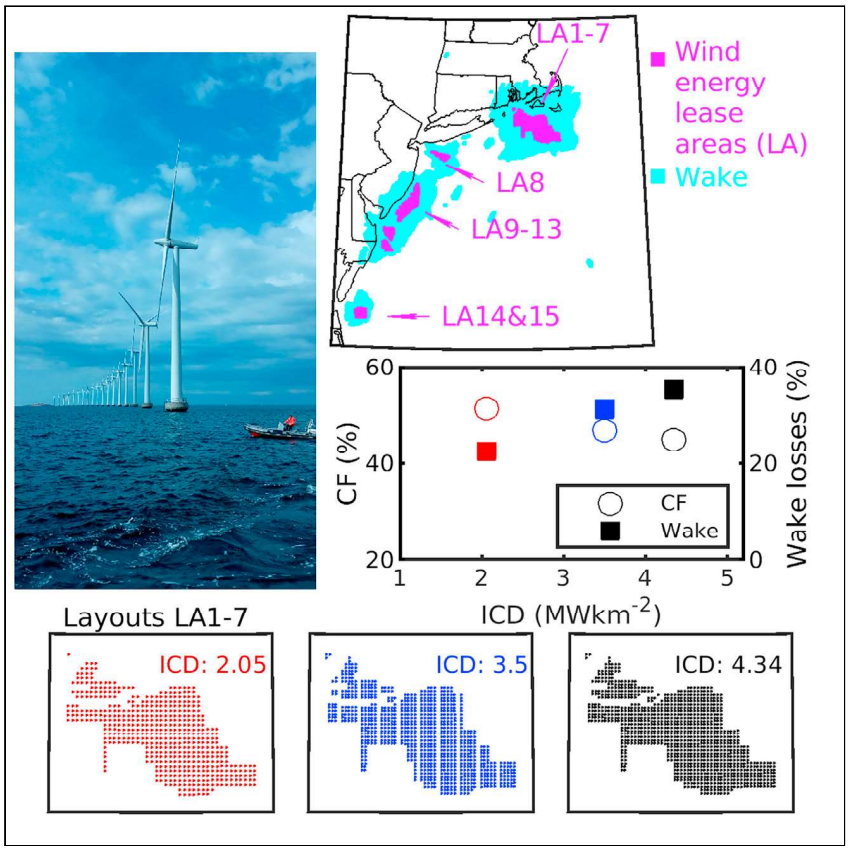

Many countries are planning development of very large offshore wind farms to aid decarbonization of the energy sector. High-resolution numerical simulations are performed to quantify power production (capacity factors [CFs]) and the spatial scale and effects of downstream wakes (areas of disturbed flow) from lease areas that are under development along the U.S. east coast. Descriptions of wake extent and power as a function of prevailing meteorology and wind-farm layout (installed capacity density [ICD]) are presented.

Sara C. Pryor, Rebecca J. Barthelmie, Tristan J. Shepherd

[redacted]@cornell.edu

Highlights

Current U.S. east coast offshore wind lease areas can supply 3% of electricity

On average wakes extend over nearly 3-times footprint of the wind turbine arrays

Power and wakes are nonlinear functions of wind turbine density and meteorology

Guidance is provided for layouts of large offshore wind farms around the world

Pryor et al., Joule 5, 2663–2686
October 20, 2021
https://doi.org/10.1016/j.joule.2021.09.002

Joule

CellPress

Article

Wind power production from very large offshore wind farms

Sara C. Pryor,[1,3,*] Rebecca J. Barthelmie,[2] and Tristan J. Shepherd[1]

SUMMARY

We provide the first quantitative assessment of power production and wake generation from offshore wind energy lease areas along the U.S. east coast. Deploying 15-MW wind turbines, with spacing equal to the European average, yields electricity production of 116 TWh/year or 3% of current national supply. However, power production is reduced by one-third due to wakes caused by upwind wind turbines and wind farms. Under some flow conditions whole wind-farm wakes can extend up to 90 km downwind of the largest lease areas, and the frequency-weighted average area with a 5% velocity deficit is 2.6 times the footprint of the lease areas. Simulations including maritime corridors demonstrate reduction in the wake effects leading to power-efficiency gains and may offer contingent benefits. First-order scaling rules are developed that describe how "wake shadows" from large offshore wind farms scale with prevailing meteorology and wind turbine installed densities.

INTRODUCTION

The move to reduce energy-related greenhouse gas emissions is gathering international momentum fueled by both the urgent need to reduce anthropogenic forcing of climate[1–3] and rapid declines in the cost of renewable generation sources.[4] The government of the United Kingdom has committed to net zero greenhouse gas emissions by 2030. A critical part of that commitment is to deploy 40 GW of offshore wind, sufficient to power every home in the United Kingdom by 2030.[5] The European Commission's long-term strategy for decarbonization assumes the installation of 400 to 450 GW of offshore wind capacity within European waters by 2050.[6] In March 2021, the White House made a commitment to deploy 30 GW of offshore wind as part of a move to reduce U.S. greenhouse gas emissions by 50% from 2005 levels in 2030 and a carbon-pollution-free power sector by 2035 (see White House briefing at; https://www.whitehouse.gov/briefing-room/). China has also committed to increasing the installed capacity of wind and solar power to over 1,200 GW by 2030 from 414 GW in 2019 (see press coverage at https://www.reuters.com/article/climate-change-un-china/chinas-xi-targets-steeper-cut-in-carbon-intensity-by-2030-idUSKBN28M0ND). This unprecedented and rapid expansion of offshore wind energy deployments affords opportunities to reduce anthropogenic climate forcing. It also raises challenges in terms of how to optimally locate wind turbines offshore at the scale required to achieve electricity-generation goals. This article provides timely and critical information to guide both U.S. and global offshore wind-energy deployments.

Estimated technically feasible potential electricity generation from U.S. offshore wind resources exceeds 7,000 Terra-Watt hours per year (TWh/year).[7] This surpasses current total national electricity generation of ~4,000 TWh/year.[8] As of May 2021, the U.S.

Context & scale

Massive upscaling of wind turbine deployments offshore is critical to achieving global and national goals to decarbonize the electricity supply. The excellent wind resource and proximity to large markets along the U.S. east coast mean it is the focus of America's first-phase offshore-wind projects. Thousands of physically larger and higher capacity wind turbines will be deployed over areas of unprecedented scale. The scale of these installations and those planned by other countries raises questions regarding potential reductions of electrical-power-production efficiency due to the operation of wind turbines in disturbed flow (wakes) from upwind wind turbines and wind farms. In this work, guidance is provided regarding the optimal layout of this new generation of wind farms to harness offshore wind resources in a manner that maximizes electricity production and minimizes the levelized cost of energy.

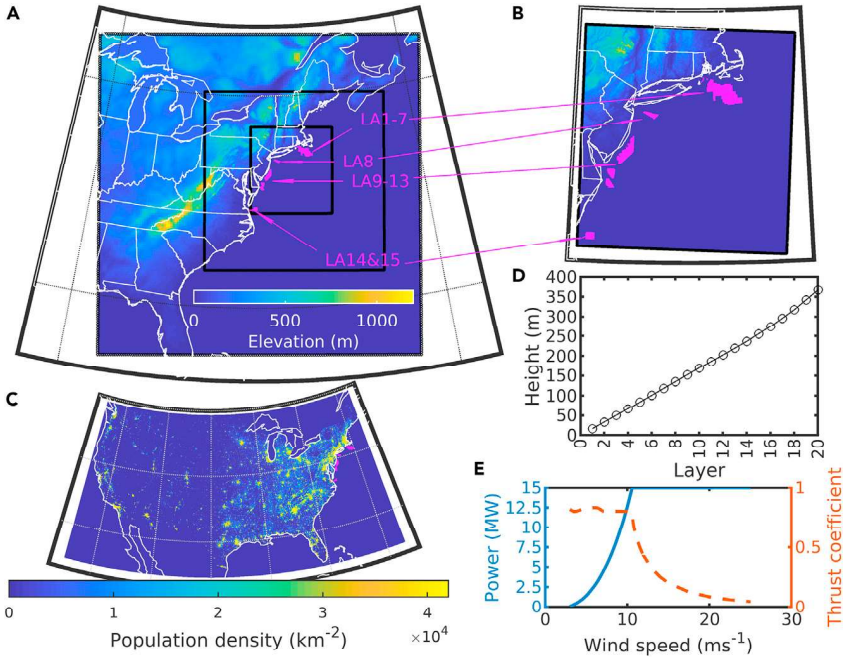

Figure 1. Overview of the simulations with the Weather Research and Forecasting (WRF) model and the locations of offshore wind-farm lease areas (LAs) along the U.S. east coast

(A) The outer WRF simulation domain (d01) has a grid resolution of 16.67 km. The second domain (d02) has a grid resolution of 5.56 km. Two inner domains (d03 and d04) comprise 340 × 361 grid cells and use a grid resolution of 1.85 km. The 15 offshore lease areas analyzed herein are shown by the magenta shading.

(B) The inner-most domain (d03 and d04) showing the lease area (LA) clusters.

(C) Proximity of the offshore lease areas to major demand centers as illustrated by the population density per km^2 according to the 2010 census (https://www.census.gov/data/tables/time-series/demo/popest/2010s-state-total.html) and the location of the 15 offshore lease areas (magenta).

(D) Mean height of the lowest 20 wind-speed levels computed for all water grid cells within d03.

(E) Wind turbine power and thrust coefficients as a function of wind speed (WS) for the IEA 15-MW reference turbine used in this analysis. This wind turbine has a HH of 150 m and rotor diameter of 240 m.[12] Power production begins at 4 ms^{-1} and ceases at WSs > 25 ms^{-1}, thus no power production or thrust coefficients are plotted for WSs outside of the range of 4–25 ms^{-1}.

had one 30-MW offshore wind farm operating at Block Island, Rhode Island, and two research turbines in Virginia.[9] However, the current total U.S. offshore wind pipeline (to 2030) is over 26 GW, much of which is focused on 16 lease areas (LAs) along the east coast[10] (Figures 1A and 1B). Realizing this pipeline would increase current U.S. wind turbine installed capacity (IC) by over 20% and almost double total global offshore installed capacity, which was 28 GW at the end of 2019.[11]

Expansion of the U.S. offshore wind industry represents a substantial financial investment. Data from Germany indicate the total installed project cost for offshore wind turbines of US$ 1,910 per kilo-Watt (kW) during 2019.[13] Projections for fixed bottom offshore wind turbines in the U.S. made in 2019 indicate total capital expenditure of US$ 4,077 per kW.[14] Using these cost estimates, installation of 26–29 GW in the 16 LAs off the U.S. east coast, equates to a direct investment of ~US$ 50 to 120 billion.

The global trend toward increased deployment of wind turbines offshore is associated with declining levelized cost of energy (LCoE), and offshore projects in the mature markets of Germany and the Netherlands are now subsidy free.[13] The

[1]Department of Earth and Atmospheric Sciences, Cornell University, Ithaca, NY 14853, USA

[2]Sibley School of Mechanical and Aerospace Engineering, Cornell University, Ithaca, NY 14853, USA

[3]Lead contact

*Correspondence: [redacted]@cornell.edu

https://doi.org/10.1016/j.joule.2021.09.002

transition to offshore deployments is driven by multiple factors. First, wind speeds are generally higher and more persistent than over land surfaces, leading to higher efficiency of electrical-power production.[11] The variation of electrical-power production from wind turbines with wind speed is described using a power curve (Figure 1E). Power production increases as wind speeds increase from cut-in when power production begins (commonly about 4 ms^{-1}) to a threshold at which the power production reaches the rated power and no longer continues to increase with increasing wind speed. This rated power thus describes the amount of electrical power in watts (i.e., joules per second) a wind turbine generates if it is operating at optimal wind speeds. Due to factors such as lower surface roughness and the absence of orographic barriers, wind turbines deployed offshore generally operate more frequently at rated power than those located onshore. Second, many major urban areas are located in coastal areas, providing nearby load centers for the electricity generated by offshore wind farms. For example, the Boston-Washington corridor, encompassing New York City, has a population over 50 million and is located close to the U.S. east coast offshore LAs (Figure 1C).

A major source of uncertainty in designing offshore wind turbine arrays (wind farms) and optimal spacing between wind farms derives from power-production losses[15,16] and enhanced fatigue loading[17] caused by operation of a wind turbine or wind farm in the wake of an upstream wind turbine or wind farm.[18] Wakes are flow regions behind wind turbines and wind farms that are characterized by lower wind speeds and higher turbulence levels and are caused by the extraction of momentum by wind turbines. The magnitude of these wakes and the downstream distance necessary for them to be eroded by mixing with surrounding high-momentum air is primarily determined by: (1) wind speed across the wind turbine rotor. This determines the efficiency of momentum extraction. The wind turbine thrust coefficient describes the magnitude of the wind-speed reduction and amount of turbulence introduced by the rotor as a nonlinear function of the incident wind speed (Figure 1E).[15] (2) Turbulence from mechanical and thermal sources. The turbulence intensity and the depth of the planetary boundary layer dictate the rate at which kinetic energy can be transferred down the velocity gradient into the wind turbine wake. For a given wind turbine or wind farm, as shown herein, these three atmospheric variables; wind speed, turbulence intensity, and boundary layer depth are largely responsible for dictating the downwind distance necessary for the flow to return to its undisturbed condition, i.e., for the wake to recover.[15,16,19] The rate at which kinetic energy can be transferred in the atmosphere limits the amount of energy that can be extracted by wind turbines per unit of surface area.[20–22] Low transfer rates can reduce power production from wind turbines in the interior of large offshore wind farms to approximately 60% of what would be achievable if all wind turbines experienced undisturbed air flow.[15,16] Low turbulence and planetary boundary layer depths offshore also mean that cumulative wind-farm wakes persist over longer downwind distances[23,24] and that wake-induced power loss within wind farms are also larger than in onshore wind farms.[15,16] (3) Wind turbine spacing: closer spacing means more wind turbines operate in the wake of upstream turbines and thus experience lower wind speeds and generate less electrical power. For example, the Horns Rev I offshore wind farm in Denmark has an IC of 166 MW, a turbine spacing of 7 × 7 rotor diameters (D) and mean reduction in power production due to wakes from upstream turbines impinging on downstream wind turbines (wake losses) of 12.4%.[25] Conversely, Lillgrund, in the coastal waters of Sweden, which has a similar IC (of 110 MW) but uses a smaller distance between wind turbines (a spacing of 3.3 to 4.3 D), exhibits wake losses of 23%.[25] (4) Wind direction: wind direction determines the likelihood that wind turbine wakes within an array interact with each other and whether the wake from one wind turbine array will be advected over another.[23,26]

The number of global offshore wind farms, the size and rated capacity of the wind turbines, and the total IC within individual arrays are increasing. For example, the mean IC of European offshore wind farms doubled from 321 to 621 MW between 2010 and 2019.[27] The largest operating offshore wind array is Hornsea Project One. It has a total IC of 1.2 GW over a deployment area of 630 km^2.[28] Despite the growth in installed capacities, the most recently built European offshore wind farms continued to employ wind turbine spacing of 4 to 11 rotor diameters (D) with a mean of 7.7D.[29] Offshore wind farms operating in Europe have installed capacity densities (ICDs), i.e., the rated power of the installed wind turbines per square kilometer of ground area) of 2.5 to 12 $MWkm^{-2}$.[30] An additional analysis of data from offshore wind farms in Europe indicates mean ICDs of 3 to 7.2 $MWkm^{-2}$, depending on the definition of wind farm areal extent.[31] There has also been a pronounced trend toward deployment of physically larger and higher-rated power wind turbines.[32] These industry trends are causing an increased probability of large wake losses within individual wind farms and an increased probability of wake interactions between offshore wind-turbine arrays.[33,34] Further, a recent meta-analysis identified wake-induced power losses as the primary source of uncertainty in preconstruction estimates of annual energy production from wind turbine arrays and a major contributor to excess project financing costs.[35] Improved understanding of wind turbine and wind-farm wakes is thus essential to ensuring the planned global investments in offshore wind achieve the electricity-generation goals and do so at the lowest possible cost.

The objective of this work is to characterize power production, wind-farm wake intensity and extent, and wake-induced power losses from planned very large offshore wind farms. This work is focused on much larger offshore wind turbine arrays than are currently operational but have a scale equal to those that are anticipated to be developed in the U.S., Europe, and China. It thus extends the literature that has previously focused primarily on smaller wind turbine arrays or has considered the limit case of nearly infinite wind farms. This work also includes an analysis of the sensitivity of power production and wake effects to both wind-farm ICD and meteorology for a wide range of atmospheric conditions that prevail offshore. Two methodological innovations are presented. A flow-scenario method is introduced to efficiently develop robust assessments of power production, wake extent and intensity, and wake-induced power losses. The concept of the normalized wake extent is also introduced and statistical models of this property as a function of prevailing meteorology are developed. The numerical simulations are performed for the existing offshore LAs along the U.S. east coast but the study findings have relevance to the global offshore wind-energy industry.

Offshore wind LAs along the U.S. east coast

LAs for possible offshore wind development in the U.S. are auctioned and managed by the Bureau of Ocean Energy Management (BOEM). The 15 offshore LAs considered here lie along the coasts of the Northeast and Atlantic U.S. states (Figures 1A and 1B[10]). Each has a unique alpha-numeric identifier; OCS-A-NNNN, where NNNN is unique to the LAs. LAs 1–7 are treated as a LA cluster herein. All seven lie within a coherent area along the coast of Massachusetts and Rhode Island and collectively cover 3,675 km^2. These include OCS-A 0487, 0500, 0501, 0520, 0521, 0522 (listed west to east) that are adjacent to one another, while OCS-A 0486 is separated from 0487 by a channel that is 2.4 km wide. LA 8 (0512) is located off the coast of New York state and covers an area of 321 km^2. LAs 9–13 cover a total area of 2,105 km^2. Two of these LAs are adjacent and are offshore from New Jersey (OCS-A 0499 and 0498). They are 23 km north of two LAs east of Delaware (OCS-A 0482 and 0519), that are 11 km north and east of the

sole Maryland LA (OCS-A 0490). These five LAs are not all adjacent but are treated as a cluster here because, as shown herein, under certain flow conditions the wake from these LAs exhibit substantial overlap. LAs 14 and 15 (OCS-A 0483 and 0497) are adjacent, cover an area of 465 km^2 and are located off the coast of Virginia. The final LA, OCS-A 0508, lies further south off the coast of North Carolina. It is not included in the innermost simulation domain and is thus excluded from consideration in this analysis.

The total extent of the LAs considered here is 6,566 km^2. This, and the spatial scale of the individual and contiguous offshore LAs along the U.S. east coast, greatly exceeds that of current European offshore wind farms. However, they are representative of the scale of future wind turbine deployments needed to meet the expressed goals of the United Kingdom, the European Union, the United States of America, and China. Quantifying power losses due to wakes as a function of atmospheric conditions (e.g., wind speed, planetary boundary layer height, and ambient turbulent kinetic energy) and ICD will inform wind turbine array layouts, and aid power-production forecasting and grid-integration planning in both the U.S. and beyond. The close proximity of these current LAs (Figures 1A and 1B) and prospective future LA offerings along the U.S. east coast[36] and the planned expansion of wind turbine deployments in the North Sea[6] further emphasize the need to quantify possible array-array interactions, particularly as adjacent LAs are owned and operated by different companies or consortia.

Simulations with the Weather Research and Forecasting (WRF) model are performed using nested domains resolved with high horizontal and vertical resolution (Figures 1A, 1B, and 1D). The modified Fitch wind-farm parameterization is used to quantify power production and wakes.[37,38] Wind-farm parameterizations such as Fitch seek to treat the bulk aerodynamic effects caused by wind turbines within and downwind of the grid cell(s) in which they are located. An estimate of the power produced by the wind turbine(s) in each grid cell and model time step is computed from the wind turbine power curve (Figure 1E) and the grid-cell-averaged incident wind-speed profile across the rotor plane. The wind turbine(s) within a given grid cell impose a drag force across the rotor plane that is determined by the wind turbine thrust coefficient (Figure 1E) and the incident wind-speed profile. This drag force removes kinetic energy from the flow resulting in a modified wind-speed profile that is advected to adjacent grid cells. Turbulent kinetic energy is added to the flow at a rate proportional to the fraction of kinetic energy extracted by the wind turbine and not converted into electrical power. It too is advected into adjacent grid cells. The wind-farm parameterization thus requires information regarding wind turbine physical dimensions, along with power and thrust coefficients that are often held confidential by wind turbine manufacturers. Therefore, the International Energy Agency (IEA) reference turbine[12] is employed, having a similar hub height (HH) and rotor diameter (D) to the G.E. Haliade-X 13-MW wind turbine (HH $\sim$ 140 m, D $\sim$ 220 m) that has been selected for LA 1.

The methodology used to efficiently generate a robust assessment of likely power production and wake losses from the U.S. east coast LAs is derived from earlier work on wind-resource assessment.[39] We identify dominant modes of relevant atmospheric flow conditions and then perform simulations for real 5-day periods that reflect those flow scenarios (Figure 2). The results from these simulations are weighted by the frequency with which each flow scenario occurs to derive climatologically representative power-production and wake statistics. The flow scenarios are abbreviated using the following nomenclature: WDWS (where WD is the wind direction and WS is the wind speed e.g., NE4-10 for northeasterly flow in the

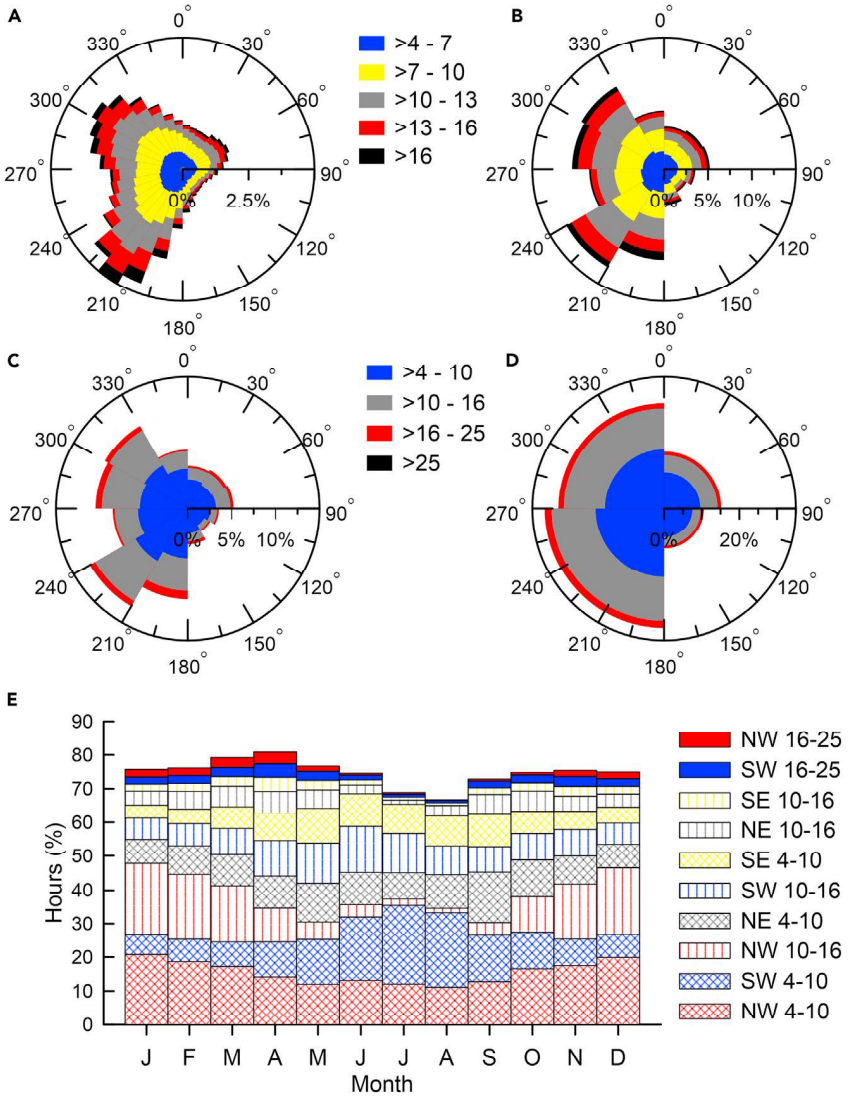

Figure 2. Overview of hourly wind speeds and directions at 100 m height in lease area 8 and the aggregation approach used to define the flow scenarios and characterize their frequency and seasonality

(A) Wind rose of all ERA5 hourly observations from 1979–2018 for the grid cell containing lease area 8 (Figures 1A and 1B) wherein the wind speeds (WSs) are discretized into 3 ms^{-1} classes for all values above 4 ms^{-1}, and wind directions (WDs) are discretized into 10° classes.

(B) As in (A) but using 30° wind direction sectors.

(C) As in (A) but for WSs in 6 ms^{-1} classes.

(D) As in (A) but using 90° wind direction sectors.

In each (A–D), the radial axis denotes the percentage of hours with wind speeds between 4 and 25 ms^{-1} that fall into the specified flow class. The ten most frequently observed combinations of wind direction and speed (denoted by WDWS) are (in rank order); SW4-10, SW10-16, NW4-10, NW4-10, NE4-10, SE4-10, NE10-16, SE10-16, SW16-25 and NW16-25.

(E) Frequency of the flow scenarios by calendar month as a percentage of hours in each month. The flow scenarios are ordered by frequency with the most frequent at the bottom. Red shading denotes northwesterly (NW) flow, blue for southwesterly (SW), black for northeasterly (NE), and yellow for southeasterly (SE) flow. Crosshatching indicates wind speeds (WS) of 4 to 10 ms^{-1}, vertical lines denote WS between 10 and 16 ms^{-1}, and the solid shading indicates WS between 16 and 25 ms^{-1}.

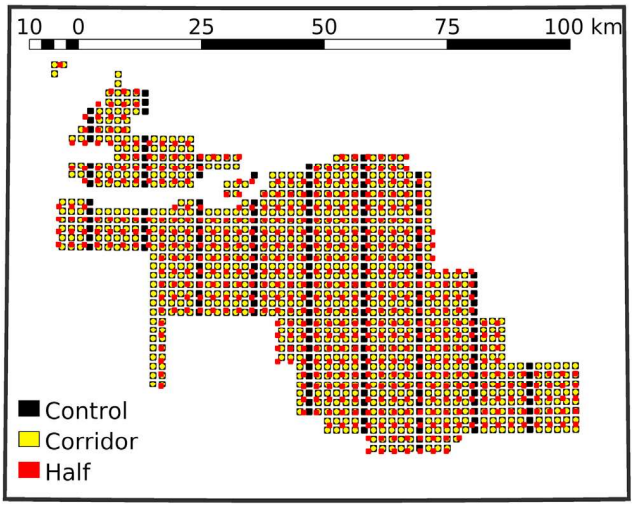

Figure 3. Illustration of the three wind-turbine deployment layouts for the lease areas 1–7 cluster (see location in Figure 1)

The black squares denote the placement of wind turbines within this cluster of lease areas in the control deployment layout with wind turbine separation of 1.85 km (for a mean installed capacity density of 4.34 $MWkm^{-2}$). The yellow circles denote placement of wind turbines in this cluster of lease areas in the maritime-corridor deployment layout (i.e., where the sixth north-south row of wind turbines from the control are removed). The red squares denote placement of wind turbines in this cluster of lease areas in the half-density deployment layout.

wind-speed class 4–10 ms^{-1}). The simulation periods are referred to here use the date; YYYY-MM-DD (i.e., year-month-day) of the first day of each 5-day period.

Simulations are performed for three different wind turbine layouts and ICD (Figure 3): (1) a control layout using the average wind turbine spacing from Europe (i.e., 7.7 wind- urbine rotor diameters), which means that the distance between each wind turbine is 1.85 km. This spacing has been selected for LAs 1 through 7. It yields a total IC of 28.8 GW from 1922 wind turbines of 15 MW each. For this wind turbine layout the mean ICD across the four clusters of LAs is 4.34 $MWkm^{-2}$. (2) A maritime-corridor layout where the sixth north-south "column" of wind turbines in each LA is removed. This reduces the total IC to 24.1 GW. (3) A half-density layout for a total installed of 14.5 GW. The ICD for this layout (~2.1 $MWkm^{-2}$) is at the lower end of current offshore wind farms in Europe.

The distribution of wind turbines between the LA clusters are as follows. In the control simulations there are 1,073 wind turbines deployed in LAs 1 through 7, 89 in LA 8, 624 in LAs 9 through 13, and 136 in LAs 14 and 15. When the maritime corridors are introduced, the total number of wind turbines in each LA cluster drops to 900, 74, 521, and 109, respectively. In the half-density layout the wind turbines are separated by ~2.8 km, and the equivalent wind turbine numbers deployed in each LA cluster are, respectively, 532, 47, 318, and 71.

Output from each of the eleven, 5-day simulations of the control layout is weighted using the relative frequency of the flow conditions it represents to derive robust estimates of expected power production and a wake climatology from the U.S. east coast LAs. The same analysis is performed for simulations of the other wind-farm layouts. Model output for the control and half-density wind-farm layouts are also used to develop first-order scaling rules that describe how the area influenced by wakes

from an offshore wind farm depends on the prevailing atmospheric conditions and the density of wind turbines within the wind farm.

RESULTS

Estimated power production from the U.S. offshore LAs

After applying frequency weighting to output from the 5-day simulations of each of the 11 flow scenarios, the expected electric-power production for the control layout is 116 TWh/year or 3% of current national supply. Electric-power production from wind turbines is summarized using capacity factors (CFs) computed as the ratio of the amount of power produced normalized by the potential power produced if all wind turbines run at their rated capacity (in this case, 15 MW). The mean CF for the control layout, where the wind turbines are spaced at the mean value from operating offshore wind farms in Europe, is 45.8% (Table 1). Power losses due to transmission, curtailment for grid operation, and operations and maintenance actions for onshore wind farms decrease CFs in the U.S. by an average of 4 percentage points.[40] Assuming that this estimate is also appropriate for offshore wind turbine arrays, the resulting estimated net-CF for these U.S. east coast offshore LAs is ~42%. This is comparable with, or better than, values reported for European (38% during 2019[41] and 40.8% cited in a meta-analysis[31]) and global (40% to 42%[11]) offshore wind farms. Thus, this modeling suggests that if the U.S. LAs are developed using wind turbines similar to the IEA 15-MW reference wind turbine laid out at a spacing equal to the mean in European offshore wind farms, they would operate with the same, or higher, CFs than those in smaller offshore wind farms in Europe that have been shown to be highly viable economically.

There is substantial variability in power production across the flow scenarios with, as expected, higher freestream wind speeds being associated with higher CFs (Figure 4A; Table 1). The higher CFs for the northern LAs (LA cluster 1–7 and LAs 8; Figures 4A and 5A) are due to: (1) higher wind speeds and thus better wind resources (Figure 5B) and (2) smaller wake losses in the smallest contiguous LA of wind turbine deployments (lease area 8, LA8) (Figures 4B and 5A). The south-north gradient of increasing wind-resource magnitude implied in the 11 simulations of the individual flow scenarios is consistent with wind-resource estimations from long-term reanalyses,[10] mesoscale simulations, and satellite-derived wind climates.[42] The most northern and largest cluster of LAs (1 through 7; see Figure 1B) exhibit a frequency-weighted mean CF of 46%, while in LA 8 it is 56%, in lease areas 9–13 it is 45% and lease areas 14 and 15 have a mean CF of 40% (Table 1; Figures 4B and 5).

Each of the LA clusters exhibits different CFs for the diverse flow scenarios due in part to variations in wind direction, and hence the over-water fetch and the resulting levels of turbulent kinetic energy (TKE) and wind speeds at the wind turbine HH (Figure 4C). For example, LAs 14 and 15 exhibit the highest mean CFs for the northeasterly flow scenarios (NE10-16 and NE4-10, represented by simulation periods that commence on 1985-11-28 and 2012-11-17) and lowest mean CFs for flow directions that are from land (NW4-10 and SW4-10, represented by simulation periods that commence on 1988-07-04 and 1998-06-04) (Figure 4B).

Two sets of sensitivity simulations for different wind turbine layouts are performed for a subset of atmospheric flow conditions. Implementation of maritime corridors reduces overall power production due to the decrease in the number of wind turbines (from 1,922 to 1,604) but increases mean CFs by 2 percentage points due to the reduction in wake losses (Figure 4A; Table 1). Reducing the wind turbine

Table 1. Summary of the flow scenarios and simulation results

		ERA5: lease area 8 centroid				Control					Corridor		Half	
Flow scenario	Start date of 5 day	% of obs.	100-m WS class (ms^{-1})	100-m wind direction class (°)	# of hours out of 120 in class	Mean CF (%)	Mean wake loss (%)	Area of d04 with $<v_d>$ of 2% (%)	Area of d04 with $<v_d>$ of 5% (%)	Area of d04 with $<v_d>$ of 10% (%)	Mean CF (%)	Mean wake loss (%)	Mean CF (%)	Mean wake loss (%)
NW4-10	1979-10-26	7.85	4–10	270–360	66	26.7	34.4	4.1	2.3	1.3	28.3	30.5	32.1	21.2
SW16-25	1981-04-04	1.6	16–25	180–270	43	76.0	13.5	7.7	3.7	1.7	–	–	–	–
SE4-10	1981-08-29	7.5	4–10	90–180	78	22.9	65.5	8.8	5.6	3.8	–	–	–	–
NE10-16	1985-11-28	4.6	10–16	0–90	64	73.6	17.5	7.6	3.3	1.6	–	–	–	–
SW10-16	1986-03-26	9.1	10–16	180–270	69	53.0	31.1	12.3	6.2	3.6	56.2	27.0	63.4	17.4
SW4-10	1988-07-04	12.5	4–10	180–270	84	9.0	64.7	14.1	4.7	2.7	10.1	60.3	13.6	47.0
NW4-10	1998-06-04	7.85	4–10	270–360	78	42.8	34.6	5.6	3.4	2.2	–	–	–	–
NW16-25	2000-01-17	1.4	16–25	270–360	32	60.7	6.8	3.6	1.6	0.2	–	–	–	–
NW10-16	2007-02-05	11	10–16	270–360	84	88.7	4.2	2.8	1.4	0.3	89.6	3.3	91.0	1.7
SE10-16	2011-05-15	2.3	10–16	90–180	37	63.3	20.7	7.7	5.0	2.9	–	–	–	–
NE4-10	2012-11-17	9.6	4–10	0–90	90	49.1	34.4	10.3	3.9	2.0	52.0	30.5	59.9	20.1
Frequency-weighted means. Two values are given for the control.						45.8[a] 45[b]	35.3[a] 34.7[b]	–	–	–	46.9	31.3	51.4	22.5

Columns on the left define the flow scenarios and the 11 5-day periods used to represent each scenario (by start date). Subsequent columns show the flow-scenario frequency based on ERA5 WS and wind direction at 100 m from the grid cell containing lease area 8 (LA8), along with the number of hours in the 5-day period that fall within the flow class. Results of the WRF simulations are shown for three different wind-turbine layouts: control in which the lease areas are fully occupied by wind turbines deployed with a 1.85 km spacing. Corridor where every sixth north-south row of wind turbines is omitted. Half (for half-installed capacity density) where the wind-turbine spacing is increased to 2.6 km (see details in Figure 3). The mean CF shown is derived from 10-min power production output from wind turbines in all lease areas. Mean wake losses are computed using the power production from the wind-farm parameterization and the maximum power possible if all wind turbines experienced the freestream WS. For the control layout the percentage of the grid cells in the innermost domain that exhibits a mean velocity deficit (v_d) of 2, 5, and 10% is also shown. Slightly over 1.5% of simulation domain d04 grid cells contain wind turbines in the control simulations.

[a]Frequency weighting across all flow scenarios.

[b]Frequency weighting of only flow scenarios also used in Corridor and half simulations.

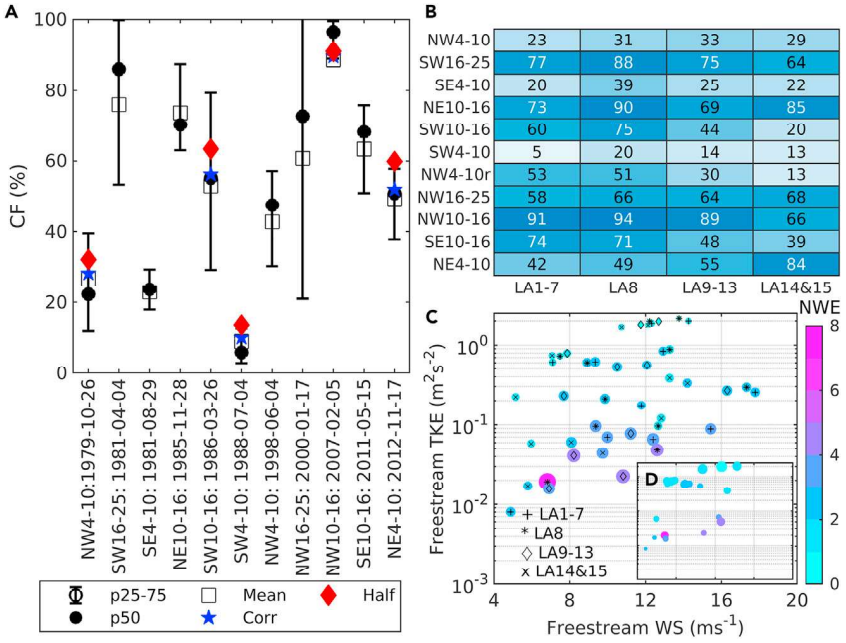

Figure 4. Capacity factors (CFs, in %) and wake extents for each of the 5-day periods that represent the 11 flow scenarios

(A) Mean, median (p50), and interquartile range (p25–75) of 10-min systemwide CFs (i.e., all lease areas) for each flow scenario in the control simulations (black). Also shown are mean capacity factors for simulations of wind turbine layouts including maritime corridors (blue stars) and half wind turbine density (red diamonds). Labels on the bottom axis indicate the flow scenario and start date of each 5-day simulation period.

(B) A heat map of mean capacity factors (CFs, in %) in each lease-area (LA) cluster for each flow scenario from the control simulations. Note: two cases are simulated for the most common flow scenario; northwesterly flow with WSs from 4 to 10 ms^{-1} (NW4-10), one in fall and one in summer (denoted by the r). The first lease area cluster (LA1–7) is located south of Massachusetts. Lease area 8 (LA8) is located off the coast of New York state. Lease areas 9–13 (LA9-13) are located offshore of New Jersey, Delaware, and Maryland. Lease areas 14 and 15 (LA14&15) are located off the coast of Virginia (Figures 1A and 1B).

(C) Normalized wake extent (NWE) calculated as the area covered by a mean velocity deficits of over 5% ($v_d \leq -0.05$) divided by the spatial extent of the lease-area cluster that generates the wake using Equation 6) for the control simulations plotted as a function of the mean freestream wind speed (WS) and turbulent kinetic energy (TKE) at 150 m in height over each lease-area cluster. There are 11 simulations and 4 lease-area clusters, thus 44 data points are plotted. The symbol size and color denote the normalized wake extent (NWE), and the marker in each NWE estimate denotes the lease-area cluster for which it is derived.

(D) (Inset to C) Difference in NWE (ΔNWE, Equation 7) plotted as a function of the mean freestream WS and TKE at 150 m over each lease-area cluster. Symbol size scales with the magnitude of ΔNWE between the control layout and half-density simulations (range 0.15–0.95), while the color denotes normalized wake extent (NWE) in the control simulations.

installed density to half of that used in the control simulations (968 wind turbines) further reduces power production but again increases mean CFs (Figure 4A; Table 1). Frequency-weighted mean CFs based on this subset of five flow scenarios increases from 45% in the control, to 46.9% in the corridor layout, and to 51.4% in the half-density layout (Table 1). This demonstrates the highly nonlinear dependence of power production and wake losses on atmospheric conditions and wind turbine spacing. Simulations such as those presented herein, which consider different wind turbine layouts, have high value in guiding development of large offshore wind farms in spatially limited LAs, particularly when they address other stakeholder interests (e.g., corridors to enable fishing and shipping) and can contribute to life-cycle financial analyses.[44]

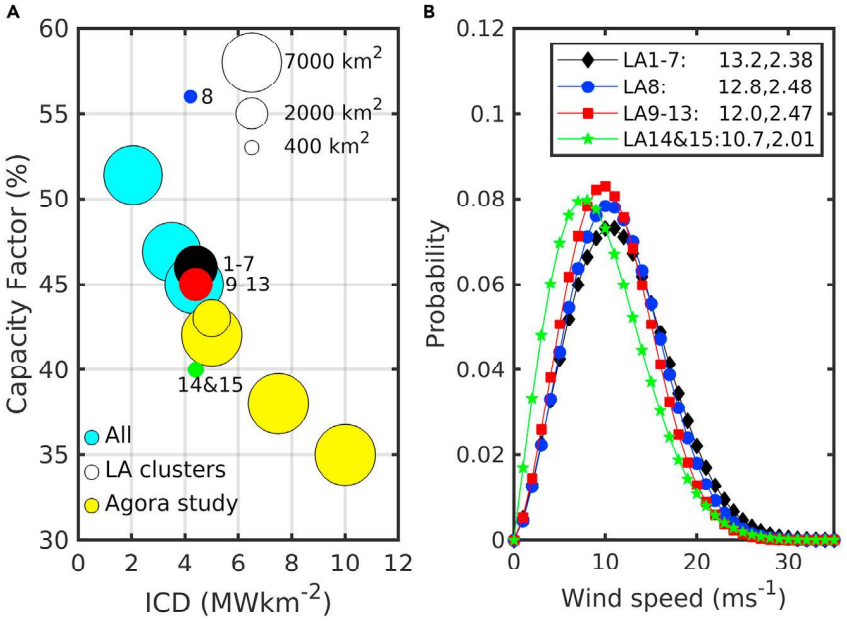

Figure 5. Capacity factors and wind speed probability distributions for the U.S. east coast lease area clusters

(A) Mean capacity factor (CFs in %) versus installed capacity density (ICD in $MWkm^{-2}$) for varying wind turbine deployment layouts and across the four lease-area (LA) clusters. The symbol diameter in (A) scales with the area over which the wind turbines are deployed (see legend, upper right). Results from this study are shown accumulated over all four lease-area clusters (cyan) for the three wind-turbine deployments—control, maritime corridors, and half-installed capacity density—(ICD), and for each the four lease-area (LA) clusters (colors as in B) from the control deployment (ICD ~ 4.34 $MWkm^{-2}$) with the numbers indicating the lease-area clusters (LAs 1–7, 8, 9–13, and 14 and 15) (see Figures 1A and 1B). Also shown are results of a study for projected developments in the German Bight area of the North Sea from the Agora study.[6] Both analyses are based on simulations with the Weather Research and Forecasting (WRF) model, but use different wind-farm parameterizations; Fitch[37,38] is shown here and the Explicit Wake Parameterization (EWP)[43] in the Agora study. Results from the Agora study are shown for 12-MW wind turbines deployed at an installed capacity density (ICD) of 5 $MWkm^{-2}$ over an area of 2,767 km^2, with an installed capacity (IC) of 13.8 GW, and in two large arrays covering areas of 2,767 km^2 and 4,473 km^2 (total IC of 36.2 GW), and for those two deployment areas at ICD of 7.5 $MWkm^{-2}$ (total IC of 54.3 GW) and of 10 $MWkm^{-2}$ (total IC of 72.4 GW).

(B) Probability distributions from a two-parameter Weibull fit to modeled freestream wind speeds (WSs) at a height of 153 m a.s.l. in the center of each lease-area (LA) cluster. The numbers in the legend in (B) indicate the Weibull A and Weibull k parameters derived using maximum likelihood estimation and Equation 3.

Estimated wake intensity and spatial extent

Despite the relatively high CFs that measure the actual energy output relative to the maximum possible, these model simulations also indicate substantial loss of potential power production due to the impingement of wakes on downstream wind turbines within individual LAs and between LAs (Figure 6). Individual LAs, and not only those that are immediately adjacent, are projected to be frequently operating in the "wind shadow" of upstream wind farms (Figure 6). This not only reduces power production but will be associated with increased mechanical loading on the wind turbines.

Frequency-weighted wake-induced power losses averaged over all LAs are 35.3% (Table 1). Thus, over a third of potential electrical-power production that could be achieved if all wind turbines operated in freestream (undisturbed) flow is lost due

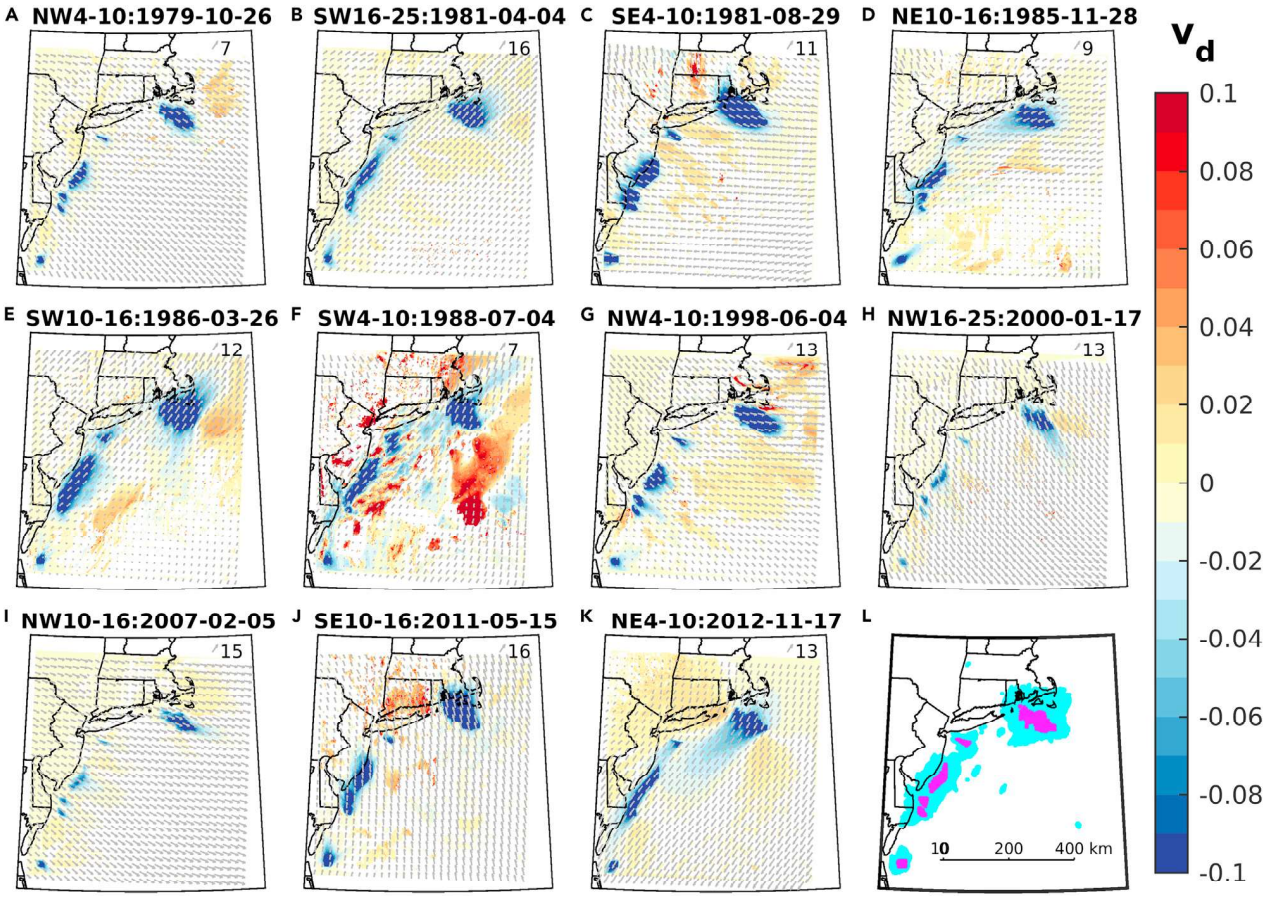

Figure 6. Mean velocity deficit (v_d) in each grid cell for each of the 5-day flow-scenario simulations (Table 1)

(A–K) The title of each panel denotes the flow scenario (the first two letters denote the wind direction and the digits indicate the WS class) and first day of each 5-day simulation period (date is written as year-month-day). The mean velocity deficit is the mean normalized difference in WS in each grid cell at each time step (i) in output from simulation domain d04 (operating wind turbines) to output from simulation domain d03 (no wind turbines) (see Equation 4). The overlying quivers are the mean WS and direction computed using output from the simulation domain d03 that describes the freestream conditions. For legibility, the quivers are plotted at the 12th grid cell in both the latitude and longitude positions and are scaled to prevent overlap. The maximum length of each quiver in each panel is set to the maximum mean WS plot for each case (shown in the upper right of the panel and expressed in ms^{-1}).

(L) Composite of all grid cells that have a mean velocity deficit of 5% or more ($v_d \leq -0.05$) in one or more of the flow cases (cyan) and the location of grid cells containing wind turbines (magenta).

to their operation within wakes from upstream wind turbines and wind farms. This value greatly exceeds wake losses from current European offshore wind farms[25] in part because of the very large extent of the wind-farm clusters and unprecedented number of wind turbines deployed.

Velocity deficits (v_d) are used here as a metric of wake intensity and extent. They represent the reduction in wind speed relative to what would be observed if no upstream wind turbines are present. These velocity deficits are calculated using wind speeds at the wind turbine HH from simulation domain d04 output with the action of wind turbines included (WS_{WT}) and output from simulation domain d03 where no wind turbines are included (WS_{NoWT}) (see methods). The concept of the normalized wake extent (NWE) is introduced to describe the areal extent of disturbed flow caused by a given wind farm. It is the ratio of the spatial extent of the wind shadow generated by a wind farm to the area of the wind farm. The NWE is naturally a

function of the threshold of velocity deficit used to define the wake. The area covered by mean velocity deficits of 2% (i.e., $v_d \leq -0.02$, Equation 4) for the 11 flow scenarios with the control layout ranges from 2.8% to 14.1% of the innermost model domain where wind turbines are operating (d04), while the area covered by wind turbines is 1.5% (Table 1). Thus, the mean NWE using this velocity deficit threshold varies depending on the prevailing atmospheric conditions but is between two times and nearly ten times the spatial extent of the wind farms. Similar mean NWEs computed for the different flow scenarios using a velocity deficit (v_d) of 5% range from one to four, with a weighted mean of 2.6. Using a velocity deficit (v_d) of 10% to define the area covered by a wake, the mean NWE in each 5-day simulation ranges from 0.15 to nearly three (Table 1). These values indicate that, consistent with expectations, wind turbine deployments within these LAs will generate substantial downstream "wind shadows" (Figure 6). As discussed further below, large, NWEs are associated with simulations of flow conditions characterized by moderate wind speeds, low ambient turbulence, and low planetary boundary layer depths.

The NWE is substantially smaller in the half-density simulations for all LA clusters and all values of freestream wind speed, planetary boundary layer height, and TKE (Figure 7). The mean difference in normalized spatial wake extents in the control and half-density simulations (ΔNWE, computed using Equation 7) is 0.48. Thus, the area covered by mean velocity deficit of at least 5% reduces to half the value from the control simulations when a half-density wind turbine layout is simulated. Thus, on average, there is a systemwide benefit from minimizing wind shadows from upstream LAs by locating wind turbines with greater spacing. However, the range of ΔNWE extends from 0.12 to 0.96, indicating that under some atmospheric flow conditions the NWE is only modestly influenced by the density of wind turbine deployments in the LAs. The difference in NWE in the half-density simulations relative to the control is maximized for periods with high ambient turbulence (Figure 4D). Thus, the decrease in wake extent due to the reduction in ICD is disproportionately weighted toward periods with relatively small, NWEs in the control simulations. The BOEM intends to auction additional LAs close to these existing LAs. While adoption of lower ICD will reduce revenues to individual LA operators, it may have benefits in terms of reducing systemwide power losses and wind turbine fatigue loading due to wakes within wind farms and between wind farms.

An alternative metric of the wind-farm wake extent is the maximum distance downwind from LA clusters aligned with the mean wind direction to which a mean velocity deficit of at least 5% ($v_d \leq -0.05$) extends (Figure 6L). For the control simulations, the minimum downwind wake extent from the largest LA cluster (LAs 1–7) is 14 km. It is associated with northwesterly flow scenarios (represented by simulations commencing on 1979-10-26 and 2007-02-05) (Figure 6A–6K). These simulations exhibit flow from over land to this LA cluster with relatively low freestream wind speeds (5–8 ms^{-1} at the center of these LAs at ~150 m in height) and moderate freestream TKE of ~1 m^2s^{-2}. The maximum wake extent from the LAs 1–7 of 90 km is found for the SW10-16 flow scenario (the simulation starting on 1986-03-26) and the NE4-10 flow scenario (represented by the simulation that starts on 2012-11-17) (Figure 6). The SW10-16 case exhibits higher wind speeds (freestream wind speed at ~150 m at the center of the LA cluster of ~10 ms^{-1}) but has a long over-water fetch, which results in low freestream TKE < 0.07 m^2s^{-2} that contributes to slow wake recovery and large wake-propagation distances. By contrast, the NE4-10 case exhibits higher TKE < 0.4 m^2s^{-2}, but lower wind speeds (WSs ~7.8 ms^{-1}) and higher thrust coefficients, which also lead to larger wake extents. For cases with southerly, southwesterly mean flow, i.e.,

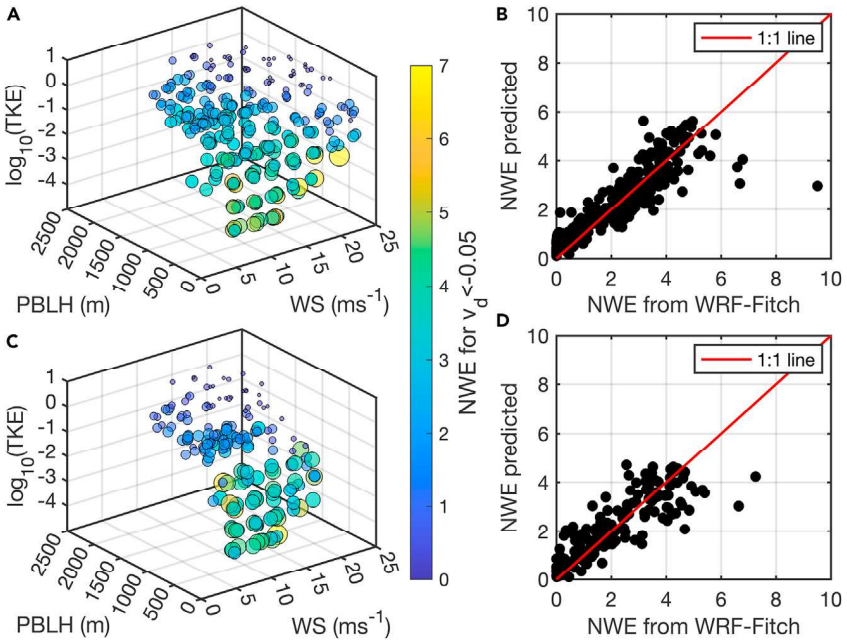

Figure 7. Spatial extent of disturbed flow (wakes) from offshore wind farms shown as a function of prevailing meteorology

(A and C) 3D bubble plots of the normalized wake extent (NWE, for a velocity deficit threshold 5%, i.e., $v_d < -0.05$) from each of the four lease-area clusters as a function of freestream wind speed (WS) and turbulent kinetic energy (TKE, shown in $\log_{10}$ scale) close to the wind-turbine HH of 150 m, and the freestream planetary boundary layer height (PBLH) in the centroid of the lease-area cluster.

(A) Results from the simulations of the control layouts, where wind turbines are installed with the mean separation of 7.7 times the wind-turbine rotor diameter. The installed capacity density for these control simulations is approximately 4.34 $MWkm^{-2}$.

(C) Results from the simulations of the half-density layouts, where the density of wind turbines is reduced to half that used in the control layout and represents the lowest densities used in European offshore wind farms. The associated installed capacity density is ~2.2 $MWkm^{-2}$.

(B and D) Scatterplots of the normalized wake extent (NWE) for each combined WS, PBLH, and TKE class derived directly from the WRF-Fitch output versus those predicted from the regression models.

(B) Results for an installed capacity density of 4.34 $MWkm^{-2}$ (i.e., the control simulations) where the regression model has the form, $NWE = 3.52 - 0.093 \times WS - 0.73 \times log_{10}(TKE) - 6.3 \times 10^{-4} \times PBLH$.

(D) Results for an installed capacity density of ~2.2 $MWkm^{-2}$ (i.e., the half-density simulations) where the regression model has the form, $NWE = 3.00 - 0.056 \times WS - 0.57 \times log_{10}(TKE) - 11 \times 10^{-4} \times PBLH$.

SW4-10 (1988-07-04), SW10-16 (1986-03-26), SW16-25 (1981-04-04) or northeasterly flow, NE4-10 (2012-11-17), velocity deficits above 5% fully encompass all of the mid-Atlantic LA clusters (LAs 9–13) indicating substantial array-array interactions, despite separation distances of up to ~23 km (Figure 6).

The SW4-10 flow scenario is observed for 12.5% of hours (Table 1) and is associated with the largest systemwide wake losses, and hence the smallest CFs (Table 1; Figure 4A). The 5-day simulation period starting 1988-07-04 has a freestream modal wind direction of ~210°, median WS of 6.3 ms^{-1}, and TKE below 0.01 m^2s^{-1} in LA 8. Mean CFs for LAs 1–7 for this flow scenario are particularly small (Figure 4B) due to low freestream WSs and a clear deep array wake effect. Fewer than 6% of wind turbines, all of which are located on the edge of the array, exhibit power production above 10% of rated power. Mean CFs for LAs 9–13 are also low for this flow scenario (14%) (Figure 4B), and the contour enclosing mean velocity deficits above 5% ($v_d \leq -0.05$) over the mid-Atlantic LA cluster for this flow scenario extends

over a 210-km distance aligned along a south-southwest to north-northeast axis (Figure 6).

This variability in wake extents and CFs between the flow scenarios emphasizes the importance of simulating a wide array of atmospheric conditions and affirms the scenario construction used herein encompasses examples of maximum and minimum wake intensity and extent (Table 1). The composite overlay of areas with mean velocity deficits of over 5% (i.e., $v_d \leq -0.05$) under one or more of the flow scenarios (Figure 6L) provides important guidance for the selection of future LAs in order to avoid places with substantial wind shadowing from existing lease areas.

These thorough analyses of the power production and wake behavior across the different LA clusters along the U.S. east coast and their dependence on wind turbine layout and prevailing meteorology provides context that is critical to developing a generalized model for wind-farm wake extents that is presented in the next section.

A generalized model of wind farm wake extent

As illustrated in the previous discussion, the time or distance downstream required for a wind turbine wake to be eroded due to mixing with surrounding, higher-momentum air, is determined by the original intensity of the wake and the mixing state of the atmosphere. The wake intensity is, in large part, dictated by the freestream WS and the wind turbine thrust coefficient (Figure 1E). The mixing state of the atmosphere and ability to transfer higher-momentum air into the wake is determined by the ambient TKE and the planetary boundary layer height. Accordingly, the mean normalized spatial extent of wakes from each LA cluster scales primarily according to both mean freestream TKE and WS at HH (Figure 4C). Large, NWEs are most evident at low WSs and low TKE (Figure 4C). Conversely, for mean TKE above 0.5 m^2s^{-2}, the NWE is almost uniformly less than twice the area of the LA clusters (Figure 4C). A weaker but still important third control on wake extent is the planetary boundary layer height (Figure 7A).

Under the hypothesis that wind-farm intensity, areal extent, and recovery are largely controlled by three variables—freestream WS, TKE, and planetary boundary layer height—a generalized model of NWE is derived. The predictand is the NWE, i.e., the area covered by a mean velocity deficit ($[v_d] \leq -0.05$). The predictors are freestream WS, TKE, and planetary boundary layer height (PBLH) for the center of each LA cluster from the domain in which no wind turbine effects are simulated. Two models are derived (see details in methods). The first uses model output from simulations of the control layout that employ a wind turbine spacing equal to that agreed for some of the LAs and that typifies the European offshore wind energy industry (ICD of 4.34 $MWkm^{-2}$). The second model uses output from half-density layouts where the wind turbines are installed over the same area but with greater separation leading to an ICD of approximately 2.2 $MWkm^{-2}$. The NWE model for the control layouts has the following form:

$$NWE = 3.52 - 0.093 \times WS - 0.73 \times log_{10}(TKE) - 6.3 \times 10^{-4} \times PBLH \quad \text{(Equation 1)}$$

All of the coefficients are statistically different from zero at a confidence level of 99% and variance explanation (R^2), adjusted for the number of predictors,[45] is 0.72 (Figure 7).

The form of this linear model (Equation 1) indicates that the areal extent of the wake from a large offshore wind farm exhibits a statistically significant negative dependence on freestream WS close to the wind turbine HH, with larger wake generation

at lower WSs. There is also a negative dependence on the base-10 logarithm of turbulence intensity (log_{10}[TKE]) at wind turbine HH. Weaker ambient turbulence leads both to slower wake recovery and to larger wake extent. Both findings are consistent with analyses of operational data from offshore wind farms that have indicated below average power production, and larger wake effects, under moderate WSs and low turbulence intensity.[15] The model also indicates evidence of a negative dependence of NWE on freestream PBLH at the center of each LA cluster. For very large wind turbine arrays wake recovery is largely dictated by the rate at which momentum can be transferred from aloft. Mixing of high-momentum air from the free troposphere across the temperature inversion that typifies the top of the boundary layer into the boundary layer is very slow. Thus, under low PBLH the volume of air from which momentum can be extracted to recover the wake is smaller than under higher PBLH.

Using the half-density layout, the coefficients in the linear model are of the same sign for each of the predictors:

$$NWE = 3.00 - 0.056 \times WS - 0.57 \times log_{10}(TKE) - 11 \times 10^{-4} \times PBLH \quad \text{(Equation 2)}$$

Again, all of the coefficients are statistically different from zero at a confidence level of 99% and variance explanation (R^2), adjusted for the number of predictors,[45] is 0.70 (Figure 7).

The high variance explanation for Equations 1 and 2 indicate that these models are relatively good representations of the model output on which they are based. Further, there are robust relationships between the areal extent of a wake generated by very large offshore wind farms and the freestream WS and TKE near the wind turbine HH and the freestream PBLH. Consistent with expectations, for the same freestream WS, turbulence intensity, and PBLH the area covered by a wake from each wind farm is smaller for wind farms that have lower ICD, or greater wind turbine spacing. For example, for a WS of 7 ms^{-1}, TKE of 0.001 ms^{-2} and a PBLH of 500 m, the area covered by a 5% velocity deficit will be an average of 4.74 times the areal footprint of the wind farm if the wind turbines are installed with a spacing equal to that of current offshore wind farms in Europe. Conversely, for the half density of wind turbine deployments, the areal extent of the wind shadow is estimated to be 3.78 the area of the offshore wind farm.

In addition to demonstrating the functional dependence of wake extent on key meteorological drivers, these equations could provisionally be used with output from WRF simulations of other global regions to provide first-order estimates of likely wind shadows from proposed offshore wind farms. Naturally, caution should be used in extrapolating to atmospheric conditions beyond those sampled in this analysis and/or to scales of wind deployments dissimilar to those addressed here. Further, it is important to note that other modeling approaches are available to describe wind turbine and wind-farm wakes,[46,47] and different wind-farm parameterizations for use within the WRF model.[43] No assessment can currently be made regarding how results presented herein may differ from those generated using other modeling frameworks.

DISCUSSION

Expansion of offshore wind is a key component of global efforts to reduce the carbon intensity of the energy sector. Deeper understanding of the atmospheric physics of large wind farms is critical to optimal, cost-effective exploitation of the substantial offshore wind resource. Our research addresses this need and is unique in several

regards. First, we present a computationally efficient and robust method to derive representative power production and wake projections for large offshore wind farms. Second, we demonstrate the approach and the concept of NWEs by applying our method to offshore wind LAs along that U.S. east coast. Last, we quantify the sensitivity of power production and wake-induced power losses to both wind-farm ICD and prevailing meteorology for a wide range of meteorological conditions that prevail offshore.

Our results indicate that power production of 116 TWh/year and mean CFs of ~ 50% can be achieved from the 15 U.S. east coast offshore wind energy LAs by employing 15-MW wind turbines at the anticipated spacing of 1.85 km (Table 1; Figure 4). CFs calculated for all three wind turbine layouts we considered meet or exceed those of currently operating offshore wind farms in Europe. They are consistent with, and indeed slightly higher than, those from an analogous WRF modeling study for projected installed wind energy capacity in 2050 for the German Bight region of the North Sea[6] (Figure 5). However, for wind turbine layouts similar to those from smaller offshore wind farms in Europe, a substantial fraction of these wind turbines will operate in wakes from upstream turbines and wind farms. These wake effects will reduce power production by over one-third (Figure 6; Table 1). There is clear evidence for substantial array-array interactions (i.e., power losses at downwind wind farms caused by wind turbines operating upwind) even for LAs separated by 23 km. These results emphasize the critical importance of evaluating potential wake losses from upstream wind farms as the BOEM moves forward with tendering additional LAs along the U.S. east coast.[36]

Using a low estimate of revenues from electricity production of $62 per MWh there are clear and substantial potential financial benefits from improved array layouts and careful siting of new wind turbine developments to reduce wake-induced power losses and increase CFs. At this scale of development (28.8 GW), a 1% increase in the CF would increase electricity output by about 2.5 TWh per year, leading to additional annual revenues of over US$150 million. Introduction of maritime corridors in the wind turbine layouts decreases estimated annual electrical-power production from 116 to 99 TWh/year. Thus, a reduction of total IC by 16.5% yields a reduction in projected power production of 14.7% because the increase in wind turbine spacing reduces wake-induced power losses and increases the efficiency of power production from the wind turbines. To provide an economic assessment of the maritime corridors scenario, we assume an installation cost of US$ 3 million per MW (the average of those projected for the U.S.[14] and realized in Germany[13]) and a power purchase price of US$ 62 per MWh of electricity produced (the average bid prices for European offshore wind farms[13]). Excluding any resulting additional cabling costs, introduction of the maritime corridors will decrease initial investment costs by ~US$ 14.3 billion but will also lower annual revenues by ~US$ 1.06 billion. Thus, the ultimate system-wide benefits of introducing maritime corridors and/or using higher or lower ICD merits detailed analyses, including all internal and external costs and benefits.

Projected power production, wake extent, and intensity are a nonlinear function of prevailing meteorology, e.g., wind resource and turbulence intensity (Figures 4C and 7), wind turbine layouts, e.g., ICD and areal extent (Figures 5 and 7), and model assumptions (e.g., wind-farm parameterization).[26,48,49] The statistical models developed here show the extent of wakes from large offshore wind farms can be explained by three atmospheric variables that are commonly available from meteorological models and/or can be measured using existing *in situ* and remote sensing technologies. The areal extent of disturbed flow normalized to the area of the wind farm that generates the wake is maximized under conditions of low turbulence intensity,

moderate WSs, and low boundary layer heights (Figure 7). Thus, offshore wind farms are most likely to experience lower power production due to the presence of upstream wind farms under relatively low WSs and when warmer air moves over a colder sea. Under these conditions, the lower atmosphere will become stably stratified resulting in low ambient turbulence and low boundary layer heights.

Given the scale of the financial investment and the critical importance of offshore wind energy to the zero-carbon-emissions economy, further work is warranted. This should include a diversity of wind turbine layouts, inclusion of alternative windfarm parameterizations and additional atmospheric flow scenarios to ensure optimal design of individual offshore wind farms and management of the large-scale global expansion of offshore wind energy.

EXPERIMENTAL PROCEDURES

Resource availability

Lead contact

Requests for further information should be directed to the lead contact, Sara C. Pryor [redacted]@cornell.edu).

Materials availability

No materials were used in this study.

Data and code availability

Source code for WRF v3.8.1 including the wind-farm parameterization patch is available from http://www2.mmm.ucar.edu/wrf/users/download/get_sources.html. ERA5 data are available from https://climate.copernicus.eu/climate-reanalysis. Shapefiles of the lease areas are available from the BOEM at; https://www.boem.gov/renewable-energy/mapping-and-data/renewable-energy-gis-data. The population density in the contiguous U.S. according to the 2010 census is available from; https://www.census.gov/data/tables/time-series/demo/popest/2010s-state-total.html. Output from the WRF simulations presented in figures and analyses herein is available for download from ZENODO (10.5281/zenodo.5137547) access to the full suite of WRF output are available via the DoE tape archive. Output from simulations of the control layouts is available from: https://portal.nersc.gov/archive/home/projects/m2645/www/public_data_NY_lease_fitch_full_density. Output from simulations of the layouts with maritime corridors is available from: https://portal.nersc.gov/archive/home/projects/m2645/www/public_data_NY_lease_fitch_recovery_corridors. Output from simulations of the half-density layouts is available from: https://portal.nersc.gov/archive/home/projects/m2645/www/public_data_NY_lease_fitch_half_density. MATLAB is a proprietary software program developed and available for purchase from MathWorks. MATLAB code used to perform the analyses is available for download from ZENODO (10.5281/zenodo.5137547).

Methods

Selecting the flow scenarios

The simulation and analysis framework presented here is designed to optimally quantify wake impacts on power production while reducing the computational cost and redundancy inherent in long-term continuous simulations. It further avoids limitations associated with use of idealized flow scenarios or individual case studies. The scenario approach ensures timely production of actionable information to those responsible for progressing development of offshore resources at the lowest LCoE. Details of the computational approach and costs are given in supplemental information.

The ERA5 reanalysis[50] is used to derive representative flow scenarios and the initial and lateral boundary conditions (LBC) for simulations with the WRF model. The ERA5 reanalysis model ingests an unprecedented suite of assimilated *in situ* and remote sensing observations.[50] ERA5 exhibits relatively high fidelity for 100-m wind speeds[40,51–53] and has been used as LBC in a range of WRF-based regional simulations including those performed for the New European Wind Atlas.[54] The periods for which WRF simulations are performed are selected based on analyses of WS and direction at 100 m a.g.l. for 1979–2018 from the ERA5 grid cell (30 × 30 km) containing the center of the New York LA (LA 8, Figures 1A and 1B). They are selected to represent commonly occurring flow conditions of relevance to power production and wake generation from wind turbines. Accordingly, the flow scenarios focus on the following WS classes; 4–10 ms^{-1} (high thrust coefficients causing relatively large wake magnitudes, Figure 1E), 10–16 ms^{-1} (moderate thrust coefficients and wakes) and 16–25 ms^{-1} (low thrust coefficients with small wake magnitude). The wind directions (WD) are also clustered into physically meaningful groups that represent differentiable modes of over-water fetch to the offshore LAs (Figure 2). Four directional classes are defined: 270°–360°, 180°–270°, 0°–90° and 90°–180° (listed in decreasing frequency). These directional classes represent flow that has a relatively short fetch over water to LA 8 (of the order tens rather than hundreds of km) for the two west sectors (SW: 180–270°, NW: 270–360°) versus those for the two easterly sectors (NE: 0–90°, SE: 90–180°) with hundreds to thousands of km of over-water fetch (Figures 1A and 1B). Ten combined WS and direction classes are required to capture 75% of the total 40 years of hourly observations. The flow scenarios are described using the nomenclature; WDWS, where WD is NE, SE, SW or NW, and WS is 4–10, 10–16 or 16–25.

Once the flow scenarios are identified, the 40 year record of hourly ERA5 derived WSs and directions at 100 m over the center of LA 8 is scanned to identify 5 day periods with the maximum number of hours that conform to each flow scenario (Table 1). Variation in atmospheric stability, turbulence intensity and PBLH offshore is dominated by the seasonal timescale due to the low frequency variability in sea surface temperatures.[55] Thus, in selecting the 5-day periods to represent the flow scenarios consideration is also given to ensuring the seasonal representation (Figure 2E). For the most frequent flow scenario (NW4-10), two cases; one in later autumn and one in summer are selected. Hence, 11 5-day periods are selected for the WRF model simulations (Table 1).

Simulation settings

Simulations are performed with WRF v3.8.1 and use the Fitch wind-farm parameterization.[38] This parameterization works such that every wind turbine in a grid cell contributes to estimated power production (in watts) as a function of the incident WS and the wind-turbine power curve (Figure 1E). Each wind turbine also induces wakes by applying a local drag force that reduces WSs and adds TKE to all model vertical levels that intersect the turbine rotor. Drag applied and TKE introduced are functions of the thrust coefficient (Figure 1E) and thus are determined by the incident WS and wind-turbine specifications.[38] Simulations performed here employ a modified version of the Fitch parameterization corrected for an earlier coding error that prevented advection of wind turbine induced TKE and that employs an updated algorithm for wind turbine added TKE.[37] Key physics setting are as in previous research[2] and shown in supplemental information. Each simulation employs a 6-h spin up and then runs for 5 days. All variables presented herein are output at 10-min intervals.

Wind resources and wind turbine wake effects are a function of model resolution.[26,48] Power density estimates from mesoscale models with a 10-km grid spacing

can be 50% lower than those from higher-resolution modeling.[48] Here, four simulation domains are employed (Figure 1A). The outer domain comprises 150 × 150 grid cells with a grid resolution of 16.67 km (d01). This is nested down to the middle domain (d02) comprising 250 × 250 grid cells resolved at 5.56 km. Two inner domains of 340 × 361 grid cells resolved using a 1.85 km resolution are run sequentially. The first (d03) is operated without the action of wind turbines to provide a freestream WS. A second identical innermost domain (d04) is run with the wind-farm parameterization turned on. The resolution used for d03 and d04 is selected to match the expected wind-turbine separation of 1.85 km.

There are 57 layers in the vertical, 20 levels at which WSs are output are below 370 m and 14 are within the rotor plane. The nineth level has a mean height of 143 m and is taken as equivalent to that at the nominal wind turbine HH = 150 m (Figure 1D).

As of early 2021 wind-turbine selections and locations for the different U.S. offshore LAs are not available. Thus, simulations are performed for three plausible wind-farm layouts. The control employs a wind-turbine spacing of 1.85 km. For the IEA 15 MW reference turbine used herein has a HH ~ 150 m and a rotor diameter (D) ~ 240 m.[12] Thus, the spacing between wind turbine of 1.85 km is equal to a spacing of 7.7D. It is equal to the average wind-turbine spacing from operating wind farms in Europe. In this set of simulations all LAs are fully covered by a total of 1922 wind turbines (Figure 3). The mean wind turbine ICD for these control simulations is 4.34 $MWkm^{-2}$. Two sets of sensitivity simulations are also performed for a subset of atmospheric flow conditions. In the corridor simulations, a maritime corridor is inserted by removing the sixth north-south "column" of wind turbines in each wind-turbine cluster, reducing the number of wind turbines to 1,604 (Figure 3). Such corridors have been proposed to accommodate shipping safety considerations and enable fishing,[56] and may also mitigate wildlife impacts.[57] In the half-density sensitivity simulations, the density of wind turbines in each LA is halved reducing the total number of wind turbines to 968. The resulting ICD (~2.1 $MWkm^{-2}$) is at the lower end of current-generation European offshore wind farms.

Statistical methods

Power production reported here derives directly from the WRF wind-farm parametrization and is determined by the WS across the rotor plane and the wind-turbine power curve (Figure 1E).

Wind regimes in the LA clusters are compared by fitting time series of modeled freestream WS at the nominal wind-turbine HH of 150 m from the centroids of each LA cluster to a two-parameter Weibull distribution:

$$p(WS) = 1 - exp\left[-\left(\frac{WS}{A}\right)^{k}\right] \qquad \text{(Equation 3)}$$

where the two parameters in this probability distribution are the scale parameter, A (units of ms^{-1}) that describes the peak in the WS distribution and shape parameter, k, that describes the dispersion around that peak. These parameters are fitted using maximum likelihood methods.[45]

The wake intensity and spatial extent is characterized using the mean fractional velocity deficit (v_d) that describes the difference in WS due to the action of wind turbines. The mean v_d in each grid cell is computed using all output from each 5-day simulation (i.e., after the 6-h spin-up period is concluded) as:

$$v_d = \frac{1}{n}\sum_{i=1}^{i=n}\left[\frac{WS_{WT(x,y,i)} - WS_{NoWT(x,y,i)}}{WS_{NoWT(x,y,i)}}\right] \quad \text{(Equation 4)}$$

The fractional velocity deficit is calculated using wind speeds at the wind-turbine HH using output from simulation domain d04 with the action of wind turbines included (WS_{WT}) and output from simulation domain d03 where no wind turbines are included (WS_{NoWT}). v_d is the mean of normalized difference in WS in each grid cell (x, y) at each of the 720 10-min timesteps in each 5-day period (i = 1 to n = 720). A two-sample t-test with a threshold p value of 0.01 is applied to assign statistical significance to the mean pairwise differences in WS. Results are corrected for multiplicity by ranking the p values from each grid cell (where j = 1 is allocated to the smallest p value and kk is the total number of grid cells) and then selecting as statistically significant only those for which the following condition is realized[45]:

$$p_j \leq \frac{j}{kk}p \quad \text{(Equation 5)}$$

The concept of NWE is introduced to characterize the region of disturbed flow generated by a wind farm that is colloquially referred to as the "wind shadow." NWEs are calculated for each LA cluster in each 5-day simulation as the area covered by a mean $v_d \leq -0.05$ ($Area_{v_d \leq -0.05}$) divided by the spatial extent of the LA cluster (i.e., group of adjacent LAs, $Area_{LAcluster}$) that generates the wake:

$$NWE = \frac{Area_{v_d \leq -0.05}}{Area_{LAcluster}} \quad \text{(Equation 6)}$$

The difference in NWE (ΔNWE) from each LA cluster in simulations with the control layout and the half-density layout is given by:

$$\Delta NWE = \frac{NWE_{control} - NWE_{half}}{NWE_{control}} \quad \text{(Equation 7)}$$

Statistical models are constructed that describe the NWE, (i.e., the area covered by a 5% velocity deficit relative to the freestream WS normalized by the areal extent of the wind-turbine deployment) as a function of prevailing meteorology. Separate models are developed using output from the control layout simulations and using output from the half-density wind-farm layouts. In these analyses the NWE from each cluster of LAs is computed for each 10-min period along with the freestream WS, $\log_{10}$(TKE) and PBLH at the center of that LA cluster. To build stable regression models output from each LA cluster and each 10-min time stamp are first composited into combined classes of wind speed, turbulence and planetary boundary layer heights using seven WS classes (4–7, 7–10, 10–13, 13–16, 16–19, 19–22, 22–25 ms^{-1}), five $\log_{10}$(TKE) classes (5×10^{-5} to 5×10^{-4}, 5×10^{-4} to 5×10^{-3}, 5×10^{-3} to 5×10^{-2}, 5×10^{-2} to 5×10^{-1}, 5×10^{-1} to 5 m^2s^{-2}) and six PBLH classes (0–400, 400–800, 800–1,200, 1,200–1,600, 1,600–2,000, 2,000–2,400 m). The calculations are performed separately for each LA cluster (Figure 7) and then combined for the model generation. For each combined class of wind speed, turbulent kinetic energy and planetary boundary layer heights that has > 4 members, mean values of NWE, WS, $\log_{10}$(TKE) and PBLH are computed. The resulting regression equations describe NWE as a function of these predictors (see Figure 7). The regression coefficients are deemed statistically significant if they differ from zero at the 99% confidence level and the goodness of fit is evaluated using the R^2 value adjusted for the number of predictors.[45]

An estimate of wake-induced power production loss is made by computing the maximum possible power production in each 10-min period if each wind turbine experienced undisturbed flow. This estimate is derived by applying the IEA reference turbine power curve (Figure 1E) to freestream WSs from the third

simulation domain (d03) at a model height of ~150 m in each grid cell where a wind turbine is present in simulation domain d04. The difference between the power derived using the wind-farm parameterization and this maximum possible power from the freestream WS is the wake loss:

$$wakeloss = \frac{\sum_1^{i=n}\left(\sum_{y=y1}^{y=y2}\sum_{x=x1}^{x=x2} PC\left(WS\left(x_{No_{WT}}, y_{NO_{WT}}, i\right)\right)\right) - \sum_1^{i=n}\left(\sum_{y=y1}^{y=y2}\sum_{x=x1}^{x=x2} P_{Fitch}\left(x_{WT}, y_{WT}, i\right)\right)}{n}$$

(Equation 8)

where I denotes the time stamps and ranges from 1 to n, where n = 720 for 10-min output over 5 days. PC is the power production as a function of WS computed from the power curve for the IEA 15 MW reference wind turbine (Figure 1E). P_{Fitch} is the power production from those same grid cells in simulation domain d04 computed by the modified Fitch scheme. The grid cells considered y1:y2 and x1:x2 are those that contain wind turbines in d04 for the control simulation.

SUPPLEMENTAL INFORMATION

Supplemental information can be found online at https://doi.org/10.1016/j.joule.2021.09.002.

ACKNOWLEDGMENTS

The US Department of Energy Office of Science (DE-SC0016605), the US Department of Energy Office of Energy Efficiency and Renewable Energy, and New York State Energy Research and Development Authority via the National Offshore Wind Research and Development consortium (147505) funded this research. This research was enabled by computational resources supported by the U.S. National Science Foundation via the Extreme Science and Engineering Discovery Environment (XSEDE) (award TG-ATM170024) and ACI-1541215, and those of the National Energy Research Scientific Computing Center, a DOE Office of Science User Facility supported by the Office of Science of the U.S. Department of Energy under contract no. DE-AC02-05CH11231. The comments from four reviewers are acknowledged.

AUTHOR CONTRIBUTIONS

S.C.P. and R.J.B. conceived the original concept and obtained the funding for the research. S.C.P. conducted all analyses presented here and drafted the manuscript and all figures. R.J.B. and S.C.P. designed the wind-turbine scenarios employed. R.J.B. designed the flow scenarios. T.J.S. performed the WRF simulations. S.C.P. and R.J.B. addressed review comments.

DECLARATION OF INTERESTS

The authors declare no competing interests.

Received: February 19, 2021
Revised: June 7, 2021
Accepted: September 8, 2021
Published: September 30, 2021

REFERENCES

1. Pryor, S.C., Barthelmie, R.J., Bukovsky, M.S., Leung, L.R., and Sakaguchi, K. (2020). Climate change impacts on wind power generation. Nat. Rev. Earth Environ. *1*, 627–643. https://doi.org/10.1038/s43017-020-0101-7.

2. Pryor, S.C., Barthelmie, R.J., and Shepherd, T.J. (2020). 20% of US electricity from wind will have limited impacts on system efficiency and regional climate. Sci. Rep. *10*, 541. https://doi.org/10.1038/s41598-019-57371-1.

3. Jacobson, M.Z., Delucchi, M.A., Bauer, Z.A.F., Goodman, S.C., Chapman, W.E., Cameron, M.A., Bozonnat, C., Chobadi, L., Clonts, H.A., Enevoldsen, P., et al. (2017). 100% clean and renewable wind, water, and

sunlight all-sector energy roadmaps for 139 countries of the world. Joule *1*, 108–121. https://doi.org/10.1016/j.joule.2017.07.005.

4. He, G., Lin, J., Sifuentes, F., Liu, X., Abhyankar, N., and Phadke, A. (2020). Rapid cost decrease of renewables and storage accelerates the decarbonization of China's power system. Nat. Commun. *11*, 2486. https://doi.org/10.1038/s41467-020-16184-x.

5. HM Government. (2020). Energy white paper. Powering our net zero future. https://www.gov.uk/government/publications/energy-white-paper-powering-our-net-zero-future.

6. Engiewende, Agora, and Verkehrswende, Agora; Technical University of Denmark; max-planck-Institute for Biogeochemistry (2020). Making the most of offshore wind: re-evaluating the potential of offshore wind in the German North Sea. https://www.agora-energiewende.de/en/publications/making-the-most-of-offshore-wind/.

7. Musial, W., Heimiller, D., Beiter, P., Scott, G., and Draxl, C. (2016). Offshore wind energy resource assessment for the United States, p. 88, Technical report NREL/TP-5000-66599. https://www.nrel.gov/docs/fy16osti/66599.pdf 2016.

8. EIA (2020). Electric power annual 2019 (Energy Information Administration). https://www.eia.gov/electricity/annual/pdf/epa.pdf.

9. BOEM (2020). Coastal Virginia offshore wind project (CVOW) (United States Department of the Interior, Bureau of Ocean Energy Management). https://www.boem.gov/renewable-energy/state-activities/coastal-virginia-offshore-wind-project-cvow.

10. Barthelmie, R.J., Dantuono, K.E., Renner, E.J., Letson, F.L., and Pryor, S.C. (2021). Extreme wind and waves in U.S. east coast offshore wind energy lease areas. Energies *14*, 1053. https://doi.org/10.3390/en14041053.

11. Jorgensen, B.H., Holtinnen, H., D'ahlgaard, K., Rosenfeldt Jakobson, K., and Marti, I. (2020). IEA Wind TCP Annual Report 2019 (International Energy Agency).

12. Gaertner, E., Rinker, J., Sethuraman, L., Zahle, F., Anderson, B., Barter, G.E., Abbas, N.J., Meng, F., Bortolotti, P., and Skrzypinski, W. (2020). IEA wind TCP Task 37: definition of the IEA 15-megawatt offshore reference wind turbine (National Renewable Energy Laboratory(NREL)). https://www.osti.gov/biblio/1603478.

13. Jansen, M., Staffell, I., Kitzing, L., Quoilin, S., Wiggelinkhuizen, E., Bulder, B., Riepin, I., and Müsgens, F. (2020). Offshore wind competitiveness in mature markets without subsidy. Nat. Energy *5*, 614–622. https://doi.org/10.1038/s41560-020-0661-2.

14. Stehly, T., Beiter, P., and Duffy, P. (2020). 2019 cost of wind energy review (National Renewable Energy Laboratory). https://www.nrel.gov/docs/fy21osti/78471.pdf.

15. Barthelmie, R.J., Hansen, K.S., and Pryor, S.C. (2013). Meteorological controls on wind turbine wakes. Proc. IEEE *101*, 1010–1019. https://doi.org/10.1109/JPROC.2012.2204029.

16. Barthelmie, R.J., and Jensen, L.E. (2010). Evaluation of wind farm efficiency and wind turbine wakes at the Nysted offshore wind farm. Wind Energy *13*, 573–586. https://doi.org/10.1002/we.408.

17. Thomsen, K., and Sørensen, P. (1999). Fatigue loads for wind turbines operating in wakes. J. Wind Eng. Ind. Aerodyn. *80*, 121–136. https://doi.org/10.1016/S0167-6105(98)00194-9.

18. Veers, P., Dykes, K., Lantz, E., Barth, S., Bottasso, C.L., Carlson, O., Clifton, A., Green, J., Green, P., Holttinen, H., et al. (2019). Grand challenges in the science of wind energy. Science *366*, eaau2027. https://doi.org/10.1126/science.aau2027.

19. Lundquist, J.K., DuVivier, K.K., Kaffine, D., and Tomaszewski, J.M. (2019). Costs and consequences of wind turbine wake effects arising from uncoordinated wind energy development. Nat. Energy *4*, 26–34. https://doi.org/10.1038/s41560-018-0281-2.

20. Miller, L.M., Brunsell, N.A., Mechem, D.B., Gans, F., Monaghan, A.J., Vautard, R., Keith, D.W., and Kleidon, A. (2015). Two methods for estimating limits to large-scale wind power generation. Proc. Natl. Acad. Sci. USA *112*, 11169–11174. https://doi.org/10.1073/pnas.1408251112.

21. Miller, L.M., and Keith, D.W. (2018). Observation-based solar and wind power capacity factors and power densities. Environ. Res. Lett. *13*, 104008. https://doi.org/10.1088/1748-9326/aae102.

22. Miller, L.M., and Keith, D.W. (2019). Corrigendum: observation-based solar and wind power capacity factors and power densities (2018 Environ. Res. Lett. 13 104008). Environ. Research Letters *14*, 079501. https://doi.org/10.1088/1748-9326/aaf9cf.

23. Hasager, C.B., Vincent, P., Badger, J., Badger, M., Di Bella, A., Peña, A., Husson, R., and Volker, P.J. (2015). Using satellite SAR to characterize the wind flow around offshore wind farms. Energies *8*, 5413–5439. https://doi.org/10.3390/en8065413.

24. Platis, A., Siedersleben, S.K., Bange, J., Lampert, A., Bärfuss, K., Hankers, R., Cañadillas, B., Foreman, R., Schulz-Stellenfleth, J., Djath, B., et al. (2018). First in situ evidence of wakes in the far field behind offshore wind farms. Sci. Rep. *8*, 2163. https://doi.org/10.1038/s41598-018-20389-y.

25. Barthelmie, R.J., Pryor, S.C., Frandsen, S.T., Hansen, K.S., Schepers, J.G., Rados, K., Schlez, W., Neubert, A., Jensen, L.E., and Neckelmann, S. (2010). Quantifying the impact of wind turbine wakes on power output at offshore wind farms. J. Atmos. Oceanic Technol. *27*, 1302–1317. https://doi.org/10.1175/2010JTECHA1398.1.

26. Pryor, S.C., Shepherd, T.J., Volker, P.J.H., Hahmann, A.N., and Barthelmie, R.J. (2020). "Wind theft" from onshore wind turbine arrays: sensitivity to wind farm parameterization and resolution. J. Appl. Meteorol. Climatol. *59*, 153–174. https://doi.org/10.1175/JAMC-D-19-0235.1.

27. Wind Europe. (2020). Offshore Wind in Europe key trends and statistics (wind Europe). https://windeurope.org/wp-content/uploads/files/about-wind/statistics/WindEurope-Annual-Offshore-Statistics-2019.pdf.

28. Mytilinou, V., and Kolios, A.J. (2019). Techno-economic optimisation of offshore wind farms based on life cycle cost analysis on the UK. Renew. Energy *132*, 439–454. https://doi.org/10.1016/j.renene.2018.07.146.

29. Bosch, J., Staffell, I., and Hawkes, A.D. (2019). Global levelised cost of electricity from offshore wind. Energy *189*, 116357. https://doi.org/10.1016/j.energy.2019.116357.

30. Deutsche WindGuard. (2018). Capacity densities of European offshore wind farms. https://www.msp-platform.eu/practices/capacity-densities-european-offshore-wind-farms.

31. Enevoldsen, P., and Jacobson, M.Z. (2021). Data investigation of installed and output power densities of onshore and offshore wind turbines worldwide. Energy Sustain. Dev. *60*, 40–51. https://doi.org/10.1016/j.esd.2020.11.004.

32. Wiser, R., Rand, J., Seel, J., Beiter, P., Baker, E., Lantz, E., and Gilman, P. (2021). Expert elicitation survey predicts 37% to 49% declines in wind energy costs by 2050. Nat. Energy *6*, 555–565.

33. Nygaard, N.G. (2014). Wakes in very large wind farms and the effect of neighbouring wind farms. J. Phys.: Conf. Ser. *524*, 012162. https://doi.org/10.1088/1742-6596/524/1/012162.

34. Schneemann, J., Rott, A., Dörenkämper, M., Steinfeld, G., and Kühn, M. (2020). Cluster wakes impact on a far-distant offshore wind farm's power. Wind Energ. Sci. *5*, 29–49. https://doi.org/10.5194/wes-5-29-2020.

35. Lee, J.C.Y., and Fields, M.J. (2021). An overview of wind-energy-production prediction bias, losses, and uncertainties. Wind Energ. Sci. *6*, 311–365. https://doi.org/10.5194/wes-6-311-2021.

36. Boutwell, S. (2019). The path forward for offshore wind leasing on the outer continental shelf (Bureau of Ocean Energy Management), June 11, 2019. https://www.boem.gov/newsroom/notes-stakeholders/message-boems-acting-director-path-forward-offshore-wind-leasing-outer.

37. Archer, C.L., Wu, S., Ma, Y., and Jiménez, P.A. (2020). Two corrections for turbulent kinetic energy generated by wind farms in the WRF model. Mon. Weather Rev. *148*, 4823–4835. https://doi.org/10.1175/MWR-D-20-0097.1.

38. Fitch, A.C., Olson, J.B., Lundquist, J.K., Dudhia, J., Gupta, A.K., Michalakes, J., and Barstad, I. (2012). Local and mesoscale impacts of wind farms as parameterized in a mesoscale NWP model. Mon. Weather Rev. *140*, 3017–3038. https://doi.org/10.1175/MWR-D-11-00352.1.

39. Tammelin, B., Vihma, T., Atlaskin, E., Badger, J., Fortelius, C., Gregow, H., Horttanainen, M., Hyvönen, R., Kilpinen, J., Latikka, J., et al. (2013). Production of the Finnish wind atlas. Wind Energy *16*, 19–35. https://doi.org/10.1002/we.517.

40. Pryor, S.C., Letson, F.W., and Barthelmie, R.J. (2020). Variability in wind energy generation across the contiguous United States. J. Appl.

Meteorol. Climatol. *59*, 2021–2039. https://doi.org/10.1175/JAMC-D-20-0162.1.

41. Wind Europe. (2020). Wind Energy in Europe in 2019: Trends and Statistics. https://windeurope.org/wp-content/uploads/files/about-wind/statistics/WindEurope-Annual-Statistics-2019.pdf.

42. Ahsbahs, T., Maclaurin, G., Draxl, C., Jackson, C.R., Monaldo, F., and Badger, M. (2020). US East Coast synthetic aperture radar wind atlas for offshore wind energy. Wind Energ. Sci. *5*, 1191–1210. https://doi.org/10.5194/wes-5-1191-2020.

43. Volker, P.J.H., Badger, J., Hahmann, A.N., and Ott, S. (2015). The explicit wake parametrisation V1.0: a wind farm parametrisation in the mesoscale model WRF. Geosci. Model Dev. *8*, 3715–3731. https://doi.org/10.5194/gmd-8-3715-2015.

44. Judge, F., McAuliffe, F.D., Sperstad, I.B., Chester, R., Flannery, B., Lynch, K., and Murphy, J. (2019). A lifecycle financial analysis model for offshore wind farms. Renew. Sustain. Energy Rev. *103*, 370–383. https://doi.org/10.1016/j.rser.2018.12.045.

45. Wilks, D.S. (2011). Statistical Methods in the Atmospheric Sciences (Academic Press).

46. Sharma, V., Cortina, G., Margairaz, F., Parlange, M.B., and Calaf, M. (2018). Evolution of flow characteristics through finite-sized wind farms and influence of turbine arrangement. Renew. Energy *115*, 1196–1208. https://doi.org/10.1016/j.renene.2017.08.075.

47. Wu, K.L., and Porté-Agel, F. (2017). Flow adjustment inside and around large finite-size wind farms. Energies *10*, 2164. https://doi.org/10.3390/en10122164.

48. Badger, J., and Volker, P.J.H. (2017). Efficient large-scale wind turbine deployment can meet global electricity generation needs. Proc. Natl. Acad. Sci. USA *114*, E8945. https://doi.org/10.1073/pnas.1708350114.

49. Volker, P.J.H., Hahmann, A.N., Badger, J., and Jørgensen, H.E. (2017). Prospects for generating electricity by large onshore and offshore wind farms. Environ. Res. Lett. *12*, 034022. https://doi.org/10.1088/1748-9326/aa5d86.

50. Hersbach, H., Bell, B., Berrisford, P., Hirahara, S., Horányi, A., Muñoz-Sabater, J., Nicolas, J., Peubey, C., Radu, R., Schepers, D., et al. (2020). The ERA5 global reanalysis. QJR Meteorol. Soc. *146*, 1999–2049. https://doi.org/10.1002/qj.3803.

51. Kalverla, P.C., Holtslag, A.A.M., Ronda, R.J., and Steeneveld, G.J. (2020). Quality of wind characteristics in recent wind atlases over the North Sea. QJR Meteorol. Soc. *146*, 1498–1515. https://doi.org/10.1002/qj.3748.

52. Ramon, J., Lledó, L., Torralba, V., Soret, A., and Doblas-Reyes, F.J. (2019). What global reanalysis best represents near-surface winds? QJR Meteorol. Soc. *145*, 3236–3251. https://doi.org/10.1002/qj.3616.

53. Jourdier, B. (2020). Evaluation of ERA5, MERRA-2, COSMO-REA6, NEWA and AROME to simulate wind power production over France. Adv. Sci. Res. *17*, 63–77. https://doi.org/10.5194/asr-17-63-2020.

54. Hahmann, A.N., Sīle, T., Witha, B., Davis, N.N., Dörenkämper, M., Ezber, Y., García-Bustamante, E., González-Rouco, J.F., Navarro, J., Olsen, B.T., and Söderberg, S. (2020). The making of the new European wind atlas – part 1: model sensitivity. Geosci. Model Dev. *13*, 5053–5078. https://doi.org/10.5194/gmd-13-5053-2020.

55. Barthelmie, R.J., Grisogono, B., and Pryor, S.C. (1996). Observations and simulations of diurnal cycles of near-surface wind speeds over land and sea. J. Geophys. Res. *101*, 21327–21337. 337. https://doi.org/10.1029/96JD01520.

56. Mehdi, R.A., Schröder-Hinrichs, J.U., van Overloop, J., Nilsson, H., and Pålsson, J. (2018). Improving the coexistence of offshore wind farms and shipping: an international comparison of navigational risk assessment processes. WMU J. Marit. Affairs *17*, 397–434. https://doi.org/10.1007/s13437-018-0149-0.

57. Petruny, L.M., Wright, A.J., and Smith, C.E. (2014). Getting it right for the North Atlantic right whale (Eubalaenaglacialis): a last opportunity for effective marine spatial planning? Mar. Pollut. Bull. *85*, 24–32. https://doi.org/10.1016/j.marpolbul.2014.06.004.

Wind Energ. Sci., 8, 787–805, 2023
https://doi.org/10.5194/wes-8-787-2023

eawe european academy of wind energy
Open Access WIND ENERGY SCIENCE

Investigating energy production and wake losses of multi-gigawatt offshore wind farms with atmospheric large-eddy simulation

Peter Baas[1], **Remco Verzijlbergh**[1,2], **Pim van Dorp**[1], **and Harm Jonker**[1,3]

[1]Whiffle, Molengraaffsingel 8, 2629 JD Delft, the Netherlands
[2]Department of Engineering Systems and Services, Delft University of Technology, Jaffalaan 5, 2628 BX Delft, the Netherlands
[3]Department of Geoscience and Remote Sensing, Delft University of Technology, Stevinweg 1, 2628 CN Delft, the Netherlands

Correspondence: Peter Baas ([redacted]@whiffle.nl)

Received: 12 December 2022 – Discussion started: 20 December 2022
Revised: 7 March 2023 – Accepted: 24 April 2023 – Published: 22 May 2023

Abstract. As a consequence of the rapid growth of the globally installed offshore wind energy capacity, the size of individual wind farms is increasing. This poses a challenge to models that predict energy production. For instance, the current generation of wake models has mostly been calibrated on existing wind farms of much smaller size. This work analyzes annual energy production and wake losses for future, multi-gigawatt wind farms with atmospheric large-eddy simulation. To that end, 1 year of actual weather has been simulated for a suite of hypothetical 4 GW offshore wind farm scenarios. The scenarios differ in terms of applied turbine type, installed capacity density, and layout. The results suggest that production numbers increase significantly when the rated power of the individual turbines is larger while keeping the total installed capacity the same. Even for turbine types with similar rated power but slightly different power curves, significant differences in production were found. Although wind speed was identified as the most dominant factor determining the aerodynamic losses, a clear impact of atmospheric stability and boundary layer height has been identified. By analyzing losses of the first-row turbines, the yearly average global-blockage effect is estimated to between 2 and 3 %, but it can reach levels over 10 % for stably stratified conditions and wind speeds around 8 m s^{-1}. Using a high-fidelity modeling technique, the present work provides insights into the performance of future, multi-gigawatt wind farms for a full year of realistic weather conditions.

1 Introduction

As part of the transition to renewable energy sources, the European offshore wind energy capacity is expanding rapidly. For example, the offshore wind energy capacity in Dutch, Belgian, Danish, and German parts of the North Sea is anticipated to reach the 65 GW mark in the year 2030 and 150 GW in the year 2050 (The Esbjerg Declaration, 2022), whereas the European-wide target for offshore wind in 2050 is 300 GW (European Commission, 2020).

Ten years ago, the largest offshore wind farms had a capacity of around 500 MW. Nowadays this number has increased to 1500 MW, and before the year 2030, wind farms of 4000 MW will be no exception. In fact, already today clusters of wind farms with a joint capacity of several gigawatts exist. In parallel, the wind turbines themselves have been increasing in size. The current generation of offshore wind turbines have a nominal power of 10 to 12 MW, but this could increase to as much as 20 MW for the year 2030. Offshore wind energy is thus entering a new phase on three levels: the total installed capacity, the size of the wind farms, and the size of the individual wind turbines.

Veers et al. (2019), among others, have pointed out the need for a better understanding of atmospheric flows through

wind farms. In particular the growth of wind farm size poses a challenge for models that predict energy production. The current generation of wake models has been extensively validated on wind farms in the 100-to-500 MW range. Using these model to make predictions for the future generation of multi-gigawatt wind farms forces them to operate well outside their validation range. This could at least add significant uncertainty to their predictions. It could therefore be argued that more physics-based models have higher fidelity in this "terra incognita".

One such modeling technique is large-eddy simulation (LES). By numerically integrating the filtered conservation equations of mass, momentum, temperature, and moisture, LES is able to capture the essential aspects of wind farm flow dynamics in a physically sound way. The "global-blockage" phenomenon is a fitting example: the presence of a wind farm induces spatial gradients in the modeled pressure field, leading to forces upwind of the wind farm, thus "informing" the flow about the "obstacle" ahead and causing the flow to deflect (around and/or over the wind farm).

LES has been at the forefront of wind farm flow physics research for some time; see for example the reviews in Mehta et al. (2014), Stevens and Meneveau (2017), and Porté-Agel et al. (2020). Owing to the increase in wind turbine and wind farm scales, a number of recent studies have explored atmospheric flows through large wind farms. Maas and Raasch (2022) have studied the wake effects of a cluster of offshore wind farms in the German Bight, exploring aspects like (far-)wake effects, boundary layer structure, turbulence, and entrainment of kinetic energy for a selection of cases with different atmospheric stabilities. Verzijlbergh (2021) discussed some aspects of modeling flows through large wind farms with illustrative LES results of a 4 GW wind farm in the North Sea.

The present work aims to explore the energy production and internal wake effects for a suite of hypothetical 4 GW offshore wind farm scenarios. The scenarios differ in terms of applied turbine type, capacity density, and layout. Furthermore, we study how wake losses depend on atmospheric stability and we discuss the global-blockage phenomenon. Amongst others, we address questions like the following: how large are wake and blockage losses in 4 GW wind farms and how do these depend on wind speed, wind direction, and atmospheric stability? What is the impact of turbine size and power density? How are losses distributed over the wind farms for different layouts and geometries?

To this end, for a total of six hypothetical wind farm scenarios we simulate 1 year of actual weather with the GRASP (GPU-Resident Atmospheric Simulation Platform) LES model. This is done by driving the LES with data from ECMWF's ERA5 reanalysis dataset (Hersbach et al., 2020). In this way, we obtain representative distributions of, for example, wind speed, stability, and baroclinicity in a natural way (Schalkwijk et al., 2015b). The resulting dataset can be regarded as a consistent, three-dimensional, 1-year dataset of pseudo-observations of meteorological variables (including wake effects) and power production (at turbine level). As such, the present work allows for a more statistical approach to studying wind farm dynamics compared to other LES studies that have mostly considered a set of idealized case studies.

This paper is organized as follows. In Sect. 2 the model is introduced. The different scenarios are described in Sect. 3. Section 4 presents the results. After a discussion in Sect. 5, the conclusions are summarized in Sect. 6.

2 Model description and simulation strategy

The model simulations are carried out with the GPU-Resident Atmospheric Simulation Platform (GRASP). GRASP is an LES code that runs almost entirely on GPUs; see Schalkwijk et al. (2012). The origin of GRASP can be traced back to the Dutch Atmospheric Large-Eddy Simulation (DALES) model, which is extensively described in Heus et al. (2010).

2.1 Governing equations

We present the most important governing equations below. More details can be found in Heus et al. (2010), Böing (2014), and Schalkwijk et al. (2015a). We follow Einstein's summation notation, with $x_1, x_2, x_3 = x, y, z$ for the coordinates and $u_1, u_2, u_3 = u, v, w$ for the wind components. The continuity equation reads

$$\frac{\partial \rho_\mathrm{b} u_j}{\partial x_j} = 0. \tag{1}$$

In the anelastic approximation employed in GRASP, the density $\rho_\mathrm{b} = \rho_\mathrm{b}(z)$ represents a base density profile depending on height only.

$$\rho_\mathrm{b}\frac{\partial u_i}{\partial t} = -\frac{\partial \rho_\mathrm{b} u_i u_j}{\partial x_j} - \frac{\partial \tau_{ij}}{\partial x_j} - \frac{\partial p'}{\partial x_i} + \delta_{i3}\rho_\mathrm{b} B + \epsilon_{ij3} f_\mathrm{c}\left(u_j - u_{\mathrm{geo},j}\right) + \left(\frac{\partial \rho_\mathrm{b} u_i}{\partial t}\right)_\mathrm{sources} \tag{2}$$

In the Navier–Stokes equation above, we denote buoyancy with B. In the buoyancy calculation a height-dependent reference temperature is used. The large-scale pressure gradient term has been written as a geostrophic wind u_geo. Further, f_c denotes the Coriolis parameter and p' the pressure fluctuations. The subgrid-scale turbulent stress, τ_{ij}, needs to be modeled with an appropriate turbulence closure. In this study we apply the Rozema model (Rozema et al., 2015), which is a minimum-dissipation eddy-viscosity model specifically developed for anisotropic grids. As such, τ_{ij} is modeled as

$$\tau_{ij} = -2K_m S_{ij}, \tag{3}$$

where

$$S_{ij} = \frac{1}{2}\left(\frac{\partial u_i}{\partial x_j} + \frac{\partial u_j}{\partial x_i}\right) \tag{4}$$

is (the symmetric part of) the velocity-gradient tensor. The eddy viscosity/diffusivity, K_m, is given by

$$K_m = (c_s \Delta)^2 f\left(S_{ij}\right), \tag{5}$$

with a term containing the grid resolution, Δ; a prefactor, c_s; and some function of the velocity-gradient tensor. The prefactor c_s is named after the so-called Smagorinsky constant in the traditional Smagorinsky subgrid model.

Transport of heat is described by

$$\rho_b \frac{\partial \vartheta_l}{\partial t} = -\frac{\partial \rho_b u_j \vartheta_l}{\partial x_j} - \frac{\partial F_j^{\vartheta}}{\partial x_j} + S_{\vartheta_l}. \tag{6}$$

Sources/sinks of temperature are, e.g., related to diabatic processes such as radiative transfer. Radiative transfer calculations are carried out offline based on the ERA5 input profiles of the relevant variables.

We use a temperature,

$$\vartheta_l = \frac{h_l}{c_p}, \tag{7}$$

which is based on moist static energy h_l:

$$h_l = c_p T + gz - L_v q_l - L_i q_i. \tag{8}$$

This is a conserved variable for moist adiabatic ascent. Here $c_p = 1005\,\mathrm{kJ\,kg^{-1}\,K^{-1}}$ denotes the specific heat capacity of air (at constant pressure), $L_v = 2.25 \times 10^6\,\mathrm{J\,kg^{-1}}$ the latent heat of vaporization of water, and $L_i = 2.84 \times 10^6\,\mathrm{J\,kg^{-1}\,K^{-1}}$ the latent heat of sublimation of ice.

Transport of moisture is described by

$$\rho_b \frac{\partial q_t}{\partial t} = -\frac{\partial \rho_b u_j q_t}{\partial x_j} - \frac{\partial F_j^{q}}{\partial x_j} + S_{q_t}, \tag{9}$$

where $q_t = q_v + q_l + q_i$ denotes the conserved variable total specific humidity, being the sum of vapor, liquid, and ice water. Subgrid fluxes of humidity are denoted F_j^q. Local sources/sinks of humidity, denoted by S_{q_t}, are related to microphysics.

An "all-or-nothing" cloud adjustment scheme is used that assumes that no cloud water/ice is present in unsaturated grid boxes, while all moisture exceeding the local saturated vapor pressure is considered liquid water or ice. In addition, the Grabowski (1998) ice microphysics scheme is used. A single precipitating prognostic variable, q_r, is used. The partitioning towards water, snow, and graupel is diagnosed with a temperature criterion. Autoconversion, the initial stage of raindrop formation, is modeled according the Kessler–Lin formulation (Khairoutdinov and Randall, 2003).

2.2 Boundary conditions

2.2.1 Large-scale meteorological conditions

In this study, the LES is coupled to ECMWF's ERA5 reanalysis dataset. As we apply periodic lateral boundary conditions, no large-scale gradients can be resolved by the LES (a model version with open boundary conditions is currently being developed). Initial conditions and large-scale (LS) tendencies are extracted from ERA5 by means of spatial and temporal interpolation and prescribed to GRASP as a function of height only (i.e., homogeneous over the domain). To account for the large-scale tendencies, several model terms are adjusted and/or added:

$$\rho_b \frac{\partial u_i}{\partial t} = \ldots + \epsilon_{ij3} f\left(u_j - u_{\mathrm{geo},j}^{\mathrm{LS}}\right) - \rho_b u_i^{\mathrm{LS}} \frac{\partial u_j^{\mathrm{LS}}}{\partial x_j} - w^{\mathrm{LS}} \frac{\partial u_i}{\partial z} + \frac{1}{\tau}\left(u_i^{\mathrm{LS}} - \overline{u_i}\right). \tag{10}$$

And for any scalar ϕ_i,

$$\rho_b \frac{\partial \phi_i}{\partial t} = \ldots - \rho_b u_i^{\mathrm{LS}} \frac{\partial \phi_j^{\mathrm{LS}}}{\partial x_j} - w^{\mathrm{LS}} \frac{\partial \phi_i}{\partial z} + \frac{1}{\tau}\left(\phi_i^{\mathrm{LS}} - \overline{\phi_i}\right). \tag{11}$$

The final terms of Eqs. (10) and (11) represent nudging to the large-scale model: the slab-averaged model fields ($\overline{u_i}$, $\overline{\phi_i}$) are nudged to ERA5 with a nudging timescale, τ, of 6 h. This timescale is long enough to give the LES physics enough freedom to establish its own unique state but short enough to make the simulation follow slow large-scale disturbances such as weather fronts (Neggers et al., 2012). In the upper quarter of the domain, the nudging timescale to ERA5 is gradually decreased (i.e., stronger nudging) towards a value of 60 s at the domain top.

2.2.2 Lower-boundary conditions

Over water surfaces (as in the present study), GRASP uses a prescribed surface temperature T_s. At the surface, saturation is assumed:

$$q_{ts} = q_{sat}(T_s, p_s). \tag{12}$$

The surface roughness lengths for momentum and heat, $z_{0m,h}$, are parameterized following the ECMWF IFS documentation (ECMWF, 2017):

$$z_{0m} = \alpha_m \frac{\nu}{u_*} + \alpha \frac{u_*^2}{g}, \tag{13}$$

$$z_{0h} = \alpha_h \frac{\nu}{u_*}, \tag{14}$$

where α is the Charnock parameter, taken as 0.0185. Furthermore, $g = 9.81\,\mathrm{m\,s^{-2}}$ is the gravitational constant; $\nu = 1.5 \times 10^{-5}\,\mathrm{m^2\,s^{-1}}$ is the kinematic viscosity of air, $\alpha_m = 0.11$, and $\alpha_h = 0.4$. For momentum, this parameterization follows Charnock (1955) with viscous effects for light wind conditions added.

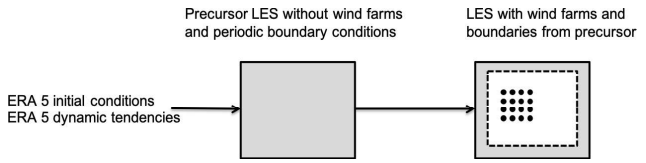

Figure 1. Schematic view of ERA5 boundary conditions, a precursor simulation, and a nested domain with turbines.

2.2.3 Upper-boundary conditions

At the top of the domain, we take

$$\frac{\partial u}{\partial z} = \frac{\partial v}{\partial z} = 0,\ w = 0,\ \frac{\partial \phi_i}{\partial z} = \text{constant in time.} \tag{15}$$

Fluctuations of velocity and scalars are damped out in the upper part of the domain by a sponge layer through additional forcing/source terms added to the right-hand side of the governing equations:

$$\rho_\mathrm{b} \frac{\partial u_i}{\partial t} = \ldots - \alpha^\mathrm{sp} \rho_\mathrm{b} (u_i - \overline{u_i}), \tag{16}$$

$$\rho_\mathrm{b} \frac{\partial \phi_i}{\partial t} = \ldots - \alpha^\mathrm{sp} \rho_\mathrm{b} \left(\phi_i - \overline{\phi_i}\right), \tag{17}$$

with α^sp being a height-dependent relaxation rate (units s^{-1}) that varies from $2.75 \times 10^{-3}\ \mathrm{s}^{-1}$ at the top of the domain to 0 at the height where the sponge layer starts, which is at 75 % of the domain height (i.e., the sponge layer comprises the upper quarter of the domain).

2.2.4 Lateral boundary conditions

In the present setup we apply periodic boundary conditions. To prevent the recirculation of wind farm wakes, we make use of a concurrent-precursor simulation (Stevens et al., 2014). This is a simulation without wind turbines that runs in parallel with the "actual" simulation. Over a boundary region, the values of the actual simulation are strongly nudged towards the precursor simulation (with an adaptive nudging timescale on the order of the model time step). A schematic overview of this setup is shown in Fig. 1.

2.3 Wind turbine parameterization

Wind turbines are modeled by a so-called actuator-disk model. This models each turbine as a semi-permeable disk that exerts forces on the flow that are consistent with the thrust curve of the wind turbine. In this way, wind farm wake effects are taken into account. In addition, using the turbine power curve, the turbine parameterization allows us to directly model power output per turbine at a high temporal resolution. The actuator-disk model is implemented following Meyers and Meneveau (2010) and Calaf et al. (2010). Within this parameterization, the total drag force exerted on the flow by a wind turbine is modeled as

$$F_\mathrm{t} = -\frac{1}{2} \rho A C_\mathrm{t}' \overline{M_\mathrm{D}}^2, \tag{18}$$

where ρ is the disk-averaged air density, $A = \pi R^2$ the frontal area of the rotor, and C_t' the thrust coefficient based on the disk-averaged wind speed M_D. Wind turbine power is given by

$$P_\mathrm{t} = -\frac{1}{2} \rho A C_\mathrm{p}' \overline{M_\mathrm{D}}^3, \tag{19}$$

with C_p' being the disk-based power coefficient. The disk-based power and thrust coefficients are determined from the manufacturer's power and thrust curves by means of an offline simulation. This additional step is required, since the manufacturer curves are based on a free-stream wind speed, M_∞; a reference density, ρ_0; and a reference turbulent intensity, TI_ref. An additional advantage of this approach is that the turbines by definition produce the correct power and thrust for the given grid configuration. The present implementation of the actuator-disk model has been tested extensively in operational practice and shows good performance for a wide range of numerical grid settings.

In order to quantify aerodynamic losses, we compare the energy production of the wind turbines with the production of so-called thrustless turbines. These thrustless turbines are embedded in the concurrent-precursor simulation. The disk-based power coefficients for the thrustless turbines are obtained by means of a separate offline simulation with the thrust coefficients set to 0. As a result, a power production of the thrustless turbines can be determined, but they do not exert drag on the flow. Thus, each thrustless turbine produces power as if it were a single isolated turbine. Furthermore, the simulations with thrustless turbines and those with the active turbines experience exactly the same turbulent wind fields at the boundaries. As such, the difference between the production of the thrustless turbines and the active turbines is a measure of the aerodynamic loss.

2.4 Simulation strategy

For each of the wind farm scenarios (Sect. 3.1), the year 2015 was simulated. For this year, observations from the meteorological mast (metmast) "Meteomast IJmuiden" were available for basic validation. The year-long simulations consist of concatenated daily simulations with a spin-up of 2 h. For each day, GRASP is initialized at 22:00 UTC the previous day. Model output valid between 00:00 and 24:00 (UTC) is used for the analysis.

The model domain consists of $640 \times 640 \times 48$ grid points. The horizontal grid spacing is 120 m; the lowest grid box has a height of 30 m. The horizontal domain size extends to 76 800 m. Vertical grid stretching was applied to obtain a domain height of 3000 m (i.e., a uniform growth factor of 2.845 %). Sensitivity experiments discussed in Sect. 5 indi-

cate that this domain size is sufficiently large. The model domain is centered around 52.8659° N, 3.5364° E. This corresponds to a location in the North Sea, roughly 100 km from the Dutch coast within the planned 4000 MW wind farm IJmuiden Ver.

Compared to other LES studies (Wu and Porté-Agel, 2017; Maas and Raasch, 2022; Strickland et al., 2022), the horizontal resolution of 120 m is relatively coarse. This choice results from a trade-off between computational cost and accuracy and has been tested extensively in an operational setting. As such, it follows from our ambition to simulate a full year of realistic weather conditions, rather than the common approach of running a suite of targeted (idealized) case studies. To provide insights into the effect of the applied resolution, the sensitivity of the results to the grid spacing is discussed in Sect. 5.

As a basic validation of the model's capability to represent the local wind conditions, Fig. 2a compares modeled versus observed wind speed at a height of 92 m. In this case, the modeled (horizontal) wind speed is taken from a virtual metmast placed at the location of the actual metmast. The correspondence between model and tower observations is satisfactory, with error metrics within the expected range for wind resource assessments. Figure 2b shows the distribution of the modeled 92 m wind speed, with a Weibull function fitted to the data. For comparison, grey dots indicate the distribution of the observations. Figure 2c presents the (modeled) wind rose, indicating that southwesterly winds have the highest frequency of occurrence and are generally stronger than winds from other sectors.

3 Wind farm scenarios and turbine characteristics

In this section, the six hypothetical 4000 MW wind farm scenarios and details of the applied turbine types will be introduced.

3.1 Scenarios

Layouts of the six considered scenarios are given in Fig. 3. The rationale for the first five scenarios is the same: each layout consists of four sites of roughly 10 km by 10 km, separated by 3 km wide corridors. Each of the four sites within each scenario has an installed capacity of approximately 1000 MW (Scenario 1 to 4). The number of turbines depends on the rated power of the applied turbine. As Scenario 5 has only half the capacity density of the other scenarios (5 MW km^{-2} instead of 10 MW km^{-2}), each of its four sites has only half the installed capacity (i.e., 500 MW). Scenario 6 is based on the actual site boundaries of the planned IJmuiden Ver wind farm for which a tender is expected to open in 2023 (RVO, 2022). The installed capacity of 4000 MW corresponds to the actual plans.

3.2 Turbine types

To study the impact of using different turbine types while keeping the total installed power approximately the same, four different turbine types have been applied. Three reference wind turbines were used with data taken from https://nrel.github.io/turbine-models/Offshore.html (last access: 18 May 2023;the DTU_10MW_178_RWT turbine (10.6 MW, labeled as DTU10), the IEA_10MW_198_RWT turbine (10.6 MW, labeled as IEA10), and the IEA_15MW_240_RWT turbine (15 MW, labeled as IEA15)). In addition, a 21.4 MW turbine was constructed by using the power and thrust curves from the IEA15 turbine but increasing the rotor diameter to obtain the desired rated power. Power and thrust curves for the four wind turbines are given in Fig. 4. The rated wind speed of the IEA10 is lower than that of the DTU10. Instead, the latter produces lower thrust. Differences between the c_p and c_t curves of the IEA10 and IEA15 turbines are small.

An overview of the scenarios and turbine characteristics is given in Table 1. The installed capacity of the first four scenarios is close to 4200 MW. For Scenario 5, with half the capacity density, this is 2100 MW. The installed capacity for the IJmuiden Ver scenario (Scenario 6) is a little lower than for the other scenarios. Turbine spacing is between 5.6 and 6.2 D for the 10 MW km^{-2} scenarios and 8.3 D for the 5 MW km^{-2} scenario. These values are in the range of values that occur in existing offshore wind farms. The baseline capacity density of 10 MW km^{-2} corresponds to the target set for future wind farms in the Dutch part of the North Sea. In the following, we consider Scenario 3 a reference, for which more detailed analyses will be presented.

4 Results

In this section we discuss the differences in energy production between the six scenarios. We distinguish between production of the thrustless turbines (also called "free-stream production" or "gross power") and the actual production ("net power"). We designate the difference between the two as the "aerodynamic losses". Depending on the application, we present either absolute aerodynamic losses (in MW or MW h) or relative aerodynamic losses (dimensionless) where the absolute losses are normalized with the free-stream production.

After analyzing the dependence of the aerodynamic losses on the wind speed, we discuss the impact of atmospheric stability and boundary layer height. Next, losses of the first-row turbines (i.e., turbines which have no other turbines upstream) will be considered, which gives an indication of the impact of blockage effects. We will also break down our results for bins of wind direction. Apart from showing the impact of wind farm layout, this illustrates that for understanding directional differences, a proper separation of the wind speed effect and the stability effect is crucial. Finally, we il-

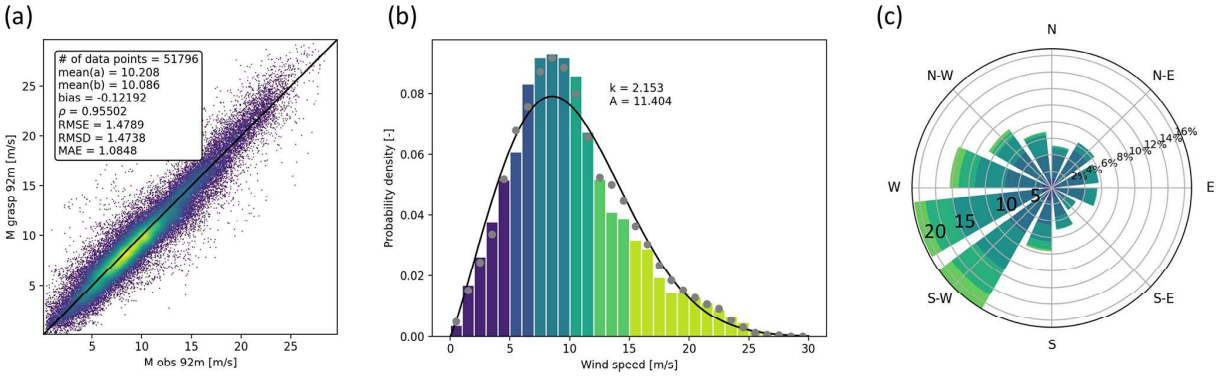

Figure 2. Validation results of GRASP versus offshore tall mast IJmuiden. **(a)** Modeled versus observed wind speed at 92 m. **(b)** Weibull plot of GRASP 92 m wind speed. Grey dots represent the observations. **(c)** Modeled wind rose at 92 m. Colors indicate 5 m s^{-1} intervals.

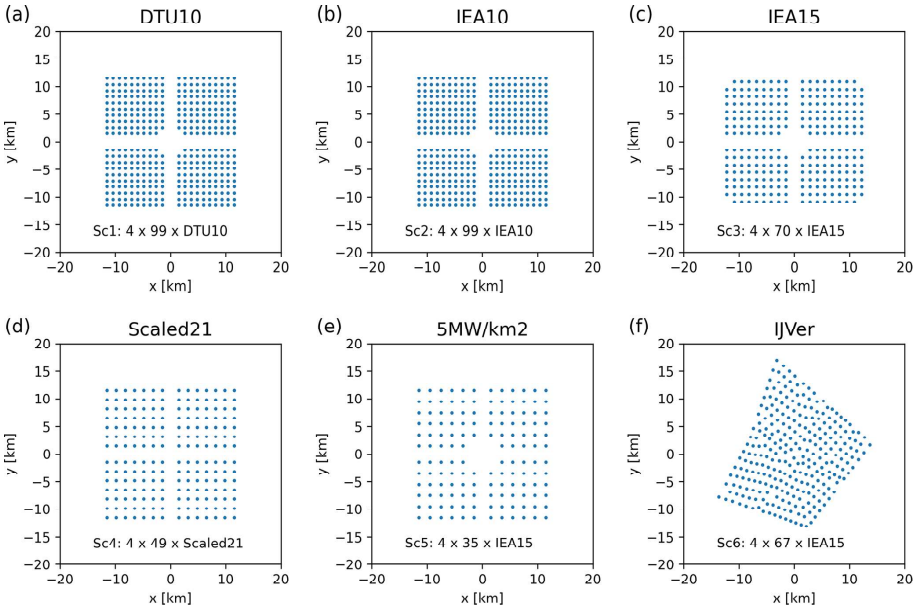

Figure 3. Layouts of the six wind farm scenarios. Panel titles refer to the scenario labels in Table 1. For each scenario the number and type of the applied turbine are indicated.

lustrate the results with a selection of composite maps showing spatial variations in wind speed and aerodynamic losses over the wind farms.

Figure 5 presents the overall energy production and the aerodynamic losses for each of the six scenarios. The aerodynamic losses vary between 12 % and 18 % for the 4 GW wind farms, whereas the 2 GW variant has losses of around 6 %. Several noticeable differences between the scenarios become apparent.

First, although the DTU10 and IEA10 turbine have the same rated power, the actual production of the IEA10 turbine is 7.7 % larger. This significant difference is the result of higher "free-stream" production numbers. These more than compensate for the slightly higher aerodynamic losses. Both the higher production and the higher aerodynamic losses for the IEA10 scenario can be related to a difference in the rotor diameter and a different behavior of the respective power curves (see Fig. 4).

Second, while keeping the same installed power, it appears to pay off to apply fewer but more powerful turbines. This is shown by comparing the IEA10, IEA15, and Scaled21 scenarios. While these three scenarios have similar free-stream production, their actual production varies significantly: for IEA10, production is 5.3 % less than for IEA15, and for Scaled21, the production is 2.8 % more. In terms of aerodynamic losses, this implies a reduction from 18.4 % for IEA10 to 11.8 % for Scaled21. At the same time, Table 1 indicates that the turbine spacing in terms of rotor diameters is approximately the same for these three scenarios. This suggests that the (relative) reduction in the number of turbines that is hampered by wakes of other turbines is a major factor contributing to higher production (for instance, the ratio of the

Table 1. Overview of the six scenarios, including turbines characteristics. Turbine radius is denoted by r, turbine rated power by P_{rated}, the wind farm installed capacity by $P_{\text{installed}}$, and the number of installed turbines by N. Turbine spacing is given in number of rotor diameters, D.

Scenario	Label	Turb. type	Hub height [m]	r [m]	P_{rated} [MW]	N [–]	$P_{\text{installed}}$ [MW]	Spacing	Density [MW km^{-2}]
1	DTU10	DTU_10MW_178_RWT	119	89	10.6	396	4198	6.2 D	10.5
2	IEA10	IEA_10MW_198_RWT	119	98	10.6	396	4198	5.6 D	10.5
3	IEA15	IEA_15MW_240_RWT	150	120	15.0	280	4200	5.6 D	10.5
4	Scaled21	Scaled_21.4MW_WT	173	143	21.4	196	4194	5.8 D	10.5
5	5MW/km2	IEA_15MW_240_RWT	150	120	15.0	140	2100	8.3 D	5.4
6	IJVer	IEA_15MW_240_RWT	150	120	15.0	268	4020	5.3 D	10.4

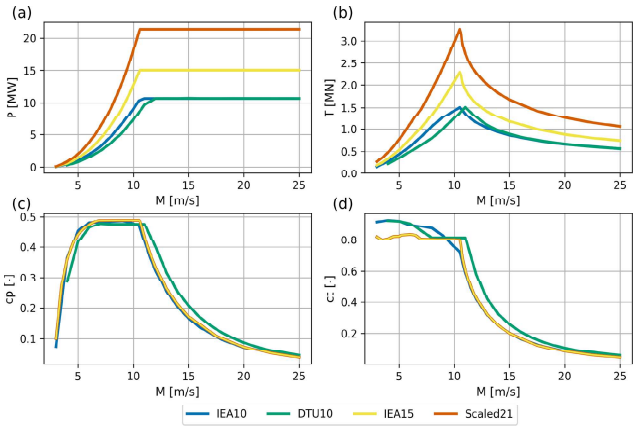

Figure 4. Power and thrust curves for the applied turbine types.

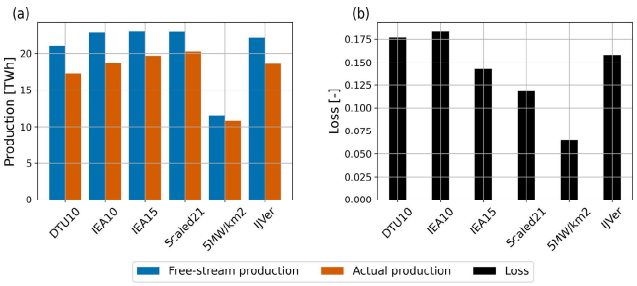

Figure 5. Total free-stream and actual production **(a)** and aerodynamic losses **(b)** for the six scenarios.

number of first-row turbines over "wake-impacted" turbines will increase (beneficially) when the total number of turbines becomes smaller).

Third, Fig. 5 illustrates the impact of varying the installed capacity per square kilometer. As expected, in the 5 MW km^{-2} scenario, the free-stream production is reduced by 50 % compared to the reference IEA15 scenario. However, the actual production decreases only by 45.2 %. The aerodynamic losses decrease drastically from 14.3 % to 6.5 %.

Fourth, the results of the IJVer scenario are comparable to the IEA15 scenario. Its free-stream production is a bit less, because the installed capacity is slightly lower. Also, its aerodynamic losses are slightly higher, which is mainly related to the absence of the 3 km wide corridors (see Fig. 3).

In summary, the present results indicate that expected aerodynamic losses for a 4 GW offshore wind farm are in the range of 12 % to 18 %, where the exact value is determined by the rated power of the applied turbines (or, the number of installed turbines). Moreover, turbines of the same rated capacity but different power curves may give significantly different production numbers. We emphasize that absolute numbers are related to the prevalent wind conditions in the simulated year 2015. To obtain annual energy production (AEP) estimates that are representative of a longer period, additional statistical postprocessing of the data is required, but this is out of the scope of the present work.

4.1 Wind speed dependence of production and losses

Figure 6 considers energy production and aerodynamic loss as a function of the free-stream disk-averaged wind speed (i.e., the disk-averaged wind speed from the thrustless turbines in the concurrent-precursor simulation). From left to right, the top panels represent averaged instantaneous wind farm production over the year, total energy production, and normalized cumulative production, respectively. The bottom panels show the equivalent aerodynamic losses. The results presented here are representative of the wind climate and the specific turbine design choices. A few interesting observations can be made.

First, Fig. 6a indicates that for wind speeds stronger than 14 m s^{-1}, all scenarios operate at rated power. For these strong wind conditions, which generate 50 % of the total energy production (Fig. 6c), the energy content of the flow is so large that aerodynamic losses are negligible.

Second, Fig. 6d–f illustrate that 80 % of all aerodynamic losses occur within a narrow wind speed range of 8 to 12 m s^{-1}. For lower wind speeds, production and losses are low anyway; for higher wind speeds, all turbines operate

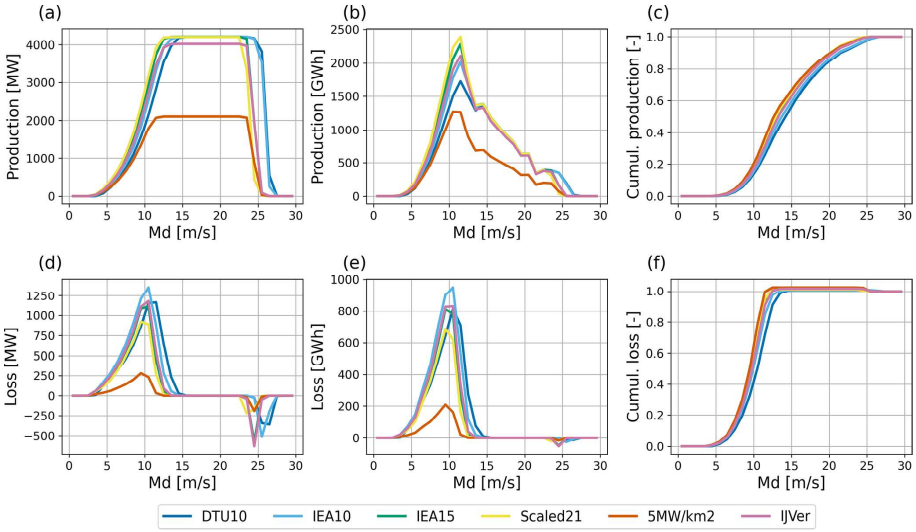

Figure 6. **(a–c)** Year-averaged wind farm power production **(a)**, total energy production for 1 m s^{-1} bins **(b)**, and normalized cumulative production **(c)** as a function of the free-stream disk-averaged wind speed. **(d–f)** Year-averaged wind farm power losses **(d)**, total aerodynamic losses for 1 m s^{-1} bins **(e)**, and normalized cumulative losses **(f)** as a function of the free-stream disk-averaged wind speed.

at (or close to) rated power. Around cut-out wind speeds, substantial instantaneous negative losses occur (Fig. 6d). This remarkable feature is caused by the fact that for these wind speeds, as a result of subtle wake effects, the number of power-producing turbines in the simulations with actual (thrust-generating) turbines is larger than in the simulations with the thrustless turbines. As the frequency of occurrence of these specific wind conditions is low, the impact of this effect on the integrated losses is small (Fig. 6e).

Third, the total energy production peaks around a wind speeds of approximately 12 m s^{-1}. This can be understood by interpreting the total energy production as a function of wind speed as a multiplication of the wind speed probability density (Fig. 2b) and the power curves.

Differences between the six scenarios are small. They are consistent with the total production numbers of Fig. 5 and can be explained by the differences in the turbine power curves (Fig. 4).

4.2 Impact of stability and boundary layer height

In this sub-section, we attempt to isolate the impact of stability and boundary layer height from the impact of the wind speed itself. For clarity reasons, mainly results for the IEA15 reference scenario are presented.

The impact of atmospheric stability on wake losses of wind farms has been widely reported in the scientific literature; see, e.g., Stevens and Meneveau (2017). As a stability parameter, we choose the bulk Richardson number, R_b, over the rotor blade of the IEA15 turbine, i.e., between heights of 270 and 30 m:

$$R_\mathrm{b} = \frac{g}{\vartheta_l} \frac{\Delta z \Delta \vartheta_l}{(\Delta u)^2 + (\Delta v)^2}. \tag{20}$$

Values of R_b are taken from the precursor simulation. As such, they represent free-stream (or undisturbed) conditions. We consider three classes of stability, separated by the percentiles 33.3 and 66.6 of the year-round distribution of R_b, which have values of −0.04 and 0.44, respectively. As such, the stability class with the 33.3 % of lowest R_b values represents convective conditions, while the class with the 33.3 % of highest R_b values represents significantly stable conditions. The class of intermediate stability contains neutral conditions but is dominated by weakly stratified conditions.

Figure 7 presents the aerodynamic losses as a function of the free-stream disk-averaged wind speed for the three stability classes for the IEA15 scenario. For a wide range of wind conditions, the impact of stability is small. However, just in the wind speed range where most of the actual losses occur, a clear impact of stability is observed. Here, for the most stably stratified conditions, relative losses are roughly 10 percentage points larger than for convective conditions. For higher wind speeds, losses quickly reduce to zero, irrespective of stability. For lower wind speeds, absolute losses (and production) are small.

The strong dependency of aerodynamic losses on the wind speed may easily obscure an analysis of the impact of stability. The relevant wind speed range for considering the impact of stability seems to be between 6 and 10 m s^{-1}. This narrow range of wind speeds is characterized by near-constant relative losses, which allows for a fair comparison between stability conditions. As can be seen in Fig. 4, this specific wind speed range coincides with the power and thrust curves being at their maximum. In the following, to indicate any impact of stability, we include only data for which the wind speed is between 6 and 10 m s^{-1}.

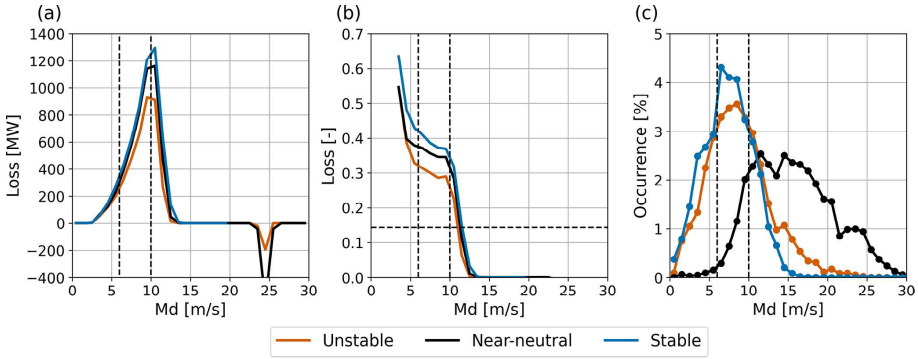

Figure 7. Combined effect of wind speed and stability on wind farm aerodynamic losses. **(a)** Power losses in megawatts (MW). **(b)** Relative aerodynamic losses. **(c)** Frequency of occurrence of the three stability classes. Dashed lines at 6 and 10 m s^{-1} indicate the wind speed interval for which the aerodynamic losses are relatively constant. The horizontal dashed line in **(b)** indicates the overall aerodynamic loss.

Table 2. Relative aerodynamic losses per scenario for free-stream disk-averaged wind speeds between 6 and 10 m s^{-1}, for the three stability classes.

Scenario	Unstable	Neutral	Stable
DTU10	0.29	0.37	0.45
IEA10	0.34	0.41	0.48
IEA15	0.29	0.35	0.38
Scaled21	0.26	0.29	0.32
MW km^{-2}	0.14	0.18	0.20
IJVer	0.32	0.36	0.41

Table 3. Contingency table showing the simultaneous frequency of occurrence (in %) of the three classes of stability (unstable, neutral, stable) and boundary layer height (low, medium, high).

	Low	Medium	High	Total
Unstable	0.3	13.9	19.1	33.3
Neutral	6.1	15.8	11.4	33.3
Stable	24.6	5.2	3.6	33.3
Total	31.0	34.9	34.1	100.0

Table 2 summarizes the relative aerodynamic losses for all six scenarios for disk-averaged wind speeds between 6 and 10 m s^{-1}. Considerable differences between scenarios exist: the higher the overall aerodynamic losses (cf. Fig. 5), the larger the impact of stability. For example, the impact of stability is clearly smaller for the Scaled21 and 5 MW km^{-2} scenarios.

To summarize, the impact of stability is only significant for a small range of wind speed conditions. However, it is exactly this range that is also most relevant for aerodynamic losses.

Apart from stability, other LES wind farm studies indicate that the boundary layer height, h, may have substantial impact on wakes and wind farm production (e.g., Maas and Raasch, 2022). Here, we examine the influence of the boundary layer height on the aerodynamic losses for the IEA15 scenario. To that end, we diagnosed the boundary layer height from model output of the precursor simulation (undisturbed conditions). We take h as the height at which the magnitude of the momentum flux becomes less than 5 % of its surface value.

We distinguish three classes of h, separated by the percentiles 33.3 and 66.6 of the year-round distribution of h, which have values of 341 and 955 m, respectively. Figure 8 presents the aerodynamic losses as a function of the free-stream disk-averaged wind speed for the three classes of boundary layer height. The results show remarkable resemblance with the stability analysis (Fig. 7). Also here, the impact is mostly confined to the wind speed range between 6 and 10 m s^{-1}. Within this range, aerodynamic losses for shallow boundary layers are clearly (around 10 percentage points) higher than for deep boundary layers.

Obviously, stability and boundary layer height are related. This is illustrated in Table 3, which shows the simultaneous occurrence of the three classes of stability and boundary layer height. Especially the shallow boundary layers clearly coincide with stably stratified conditions.

4.3 First-row losses

As with any obstacle placed in a flow, wind farms will have an impact on the flow itself. The air will tend to flow around and over the obstacle, and in front of the wind farm a reduction in wind speed is expected. This will lead to a reduction in power production of the turbines that are not in the wake of other turbines (i.e., located in the "first row"). This phenomenon is know as the global-blockage effect (Bleeg et al., 2018). As the wind speed reduction will propagate to downstream ("waked") turbines, separating the blockage effect from wake effects is virtually impossible. This is especially true for observations and physically based modeling studies like LES. Therefore, in this study we focus on losses

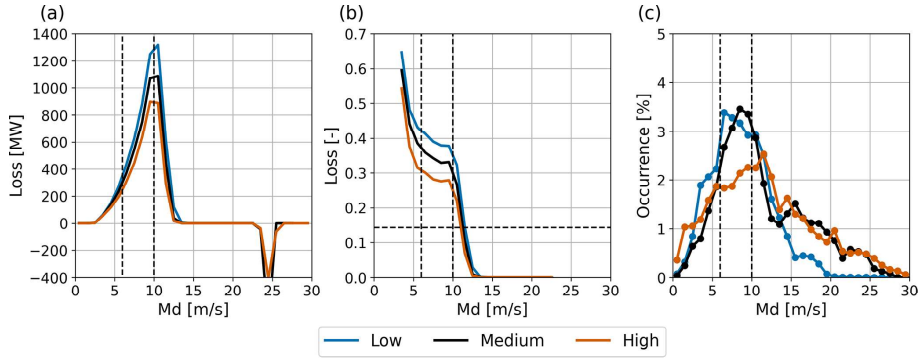

Figure 8. Combined effect of wind speed and boundary layer height on wind farm aerodynamic losses. **(a)** Power losses in megawatts (MW). **(b)** Relative aerodynamic losses. **(c)** Frequency of occurrence of the three boundary layer height classes. Dashed lines at 6 and 10 m s^{-1} indicate the wind speed interval for which the aerodynamic losses are relatively constant. The horizontal dashed line in **(b)** indicates the overall aerodynamic loss.

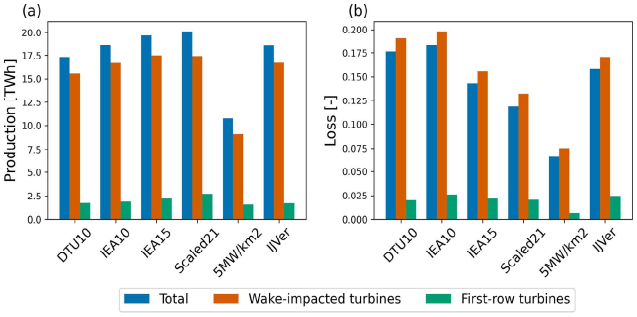

Figure 9. **(a)** Total production, production of "wake-affected" turbines, and production of first-row turbines for all six scenarios. **(b)** Aerodynamic losses.

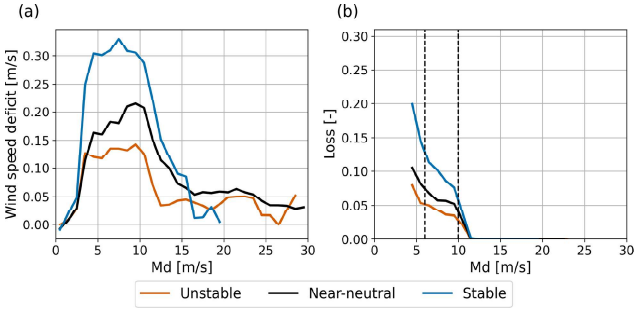

Figure 10. The reduction in the first-row 140 m wind speed compared to the free-stream wind speed **(a)** and the relative aerodynamic losses of first-row turbines **(b)** as a function of wind speed and stability.

of the first-row turbines, which can be interpreted as a conservative estimate for the blockage effect.

We determine the first-row losses as follows: given the wind direction, for each time step we verify if any other turbines are located within a 60° wide sector opposite to the flow direction. If this is not the case, a turbine is classified as a first-row turbine for that particular time step.

Figure 9 presents the year-round production numbers and relative aerodynamic losses for the first-row turbines and all other (waked) turbines. The actual production of the first-row turbines is between 2 % and 3 % lower than their corresponding thrustless (or free-stream) production. Although the applied definitions and metrics can be discussed, these values are not inconsistent with values of the blockage effect reported in the literature (e.g., Wu and Porté-Agel, 2017; Allaerts et al., 2018; Bleeg et al., 2018; Schneemann et al., 2021). Consistently, the losses of the non-first-row, or other, turbines are a bit higher than the overall losses.

As with the overall aerodynamic losses above, we can also assess the impact of both wind speed and stability on the first-row losses. Figure 10 shows that, consistently with the above results (e.g., Fig. 6), also the first-row losses are negligible for wind speeds over 12 m s^{-1}. Interestingly, the first-row wind speed deficit with respect to free-stream conditions continues towards much higher wind speeds. The majority of the first-row losses occur for wind speeds between 6 and 10 m s^{-1}. Values range from 4 % in convective conditions to 8 % in the most stable conditions. The corresponding first-row wind speed deficits vary from approximately 0.12 to 0.30 m s^{-1}. Relative first-row losses are even higher for wind speeds below 6 m s^{-1}, but these are less relevant in an absolute sense (not shown).

We conclude that first-row losses are on average between 2 % and 3 %. However, for the wind speed range where most of the losses occur these numbers can be more than twice as high. Also, first-row losses are significantly larger for stably stratified conditions (cf. Strickland et al., 2022).

4.4 Directional effects

An analysis of aerodynamic losses per wind direction reveals how the respective impacts of wind speed and stability are

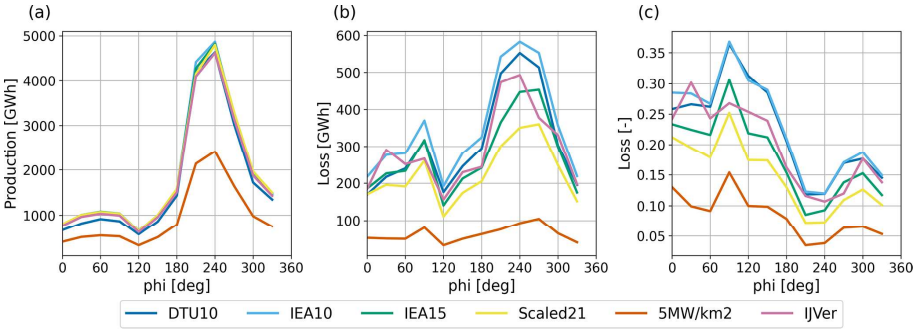

Figure 11. Directional dependence of total energy production **(a)**, absolute aerodynamic losses **(b)**, and relative losses **(c)** for the six scenarios.

entangled. Moreover, it shows the impact of difference in the layout and geometry of the wind farm scenarios.

Figure 11 shows energy production and aerodynamic losses as a function of the wind direction. The first element that stands out is the overwhelming dominance of the contribution of southwesterly winds to the total energy production. This is the cumulative effect of both the higher frequency of occurrence and the generally stronger wind speeds (see Fig. 2c), in combination with a strongly non-linear character of the turbine power curves.

Figure 11b and c show that while the absolute losses are largest for the southwesterly direction, the relative losses are much higher for easterly directions. From this figure, it cannot be determined if the difference in relative losses is mainly a wind speed effect or if stability is important here. Interestingly, the five hypothetical layouts closely follow the same pattern, but the IJVer scenario behaves differently. Comparison with Fig. 3 suggests that this difference is related to the different layout of the IJVer scenario: while other scenarios form north–south- and west–east-facing squares, the IJVer layout is significantly rotated (but still resembling a clear "square-like" shape). Inspection of Fig. 11b and c indicates that aerodynamic losses are higher/lower when the flow is directed towards the faces/corners of the wind farm layouts.

For two of the scenarios, IEA15 and IJVer, Fig. 12 breaks down the directional losses into stability and wind speed. Figure 12a and b present the relative aerodynamic losses for the three stability classes defined above, irrespective of the wind speed. Losses for stably stratified conditions are the largest, but the losses for convective conditions are also large. Because of generally higher wind speeds (i.e., lower thrust coefficients), the losses for the near-neutral class are much smaller, even when omni-direction numbers are considered (not shown).

As a next step, the bottom panels of Fig. 12 present stability-dependent losses like before but now only including wind speeds between 6 and 10 $\mathrm{m\,s^{-1}}$. By doing so, a clear organization of the data occurs, with the lowest losses occurring for convective conditions and the highest losses for the most stably stratified conditions. Moreover, a clear directional pattern is revealed, in particular for the IEA15 scenario, with much higher losses when the flow is directed to the sides of the wind farm and lower losses when the flow faces the corners of the wind farm. This pattern is clearly visible for all three stability classes. For the IJVer scenario the directional pattern is more obscured.

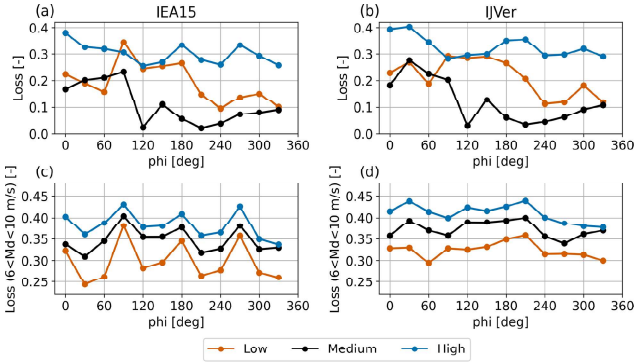

Figure 12. Directional dependence of total aerodynamic losses for different stability classes for the IEA15 **(a, c)** and IJVer **(b, d)** scenarios. The top panels **(a, b)** are based on all data; the bottom panels **(c, d)** only include wind speeds between 6 and 10 $\mathrm{m\,s^{-1}}$.

In summary, Fig. 12 demonstrates that an assessment of the impact of stability on wind farm losses is not straightforward. It can only be isolated if the data are also conditioned over a particular, carefully selected wind speed range. This is because both the turbine thrust curves and the stability depend on the wind speed but in different ways. To avoid the impact of wind speed as much as possible, this range should not be too broad, as small differences in wind speed can have a large impact on both absolute and relative aerodynamic losses (Fig. 7).

4.5 Spatial patterns

So far, we have only considered power production and aerodynamic losses for the wind farms as a whole. In the following section, we consider spatial variations in wind speed,

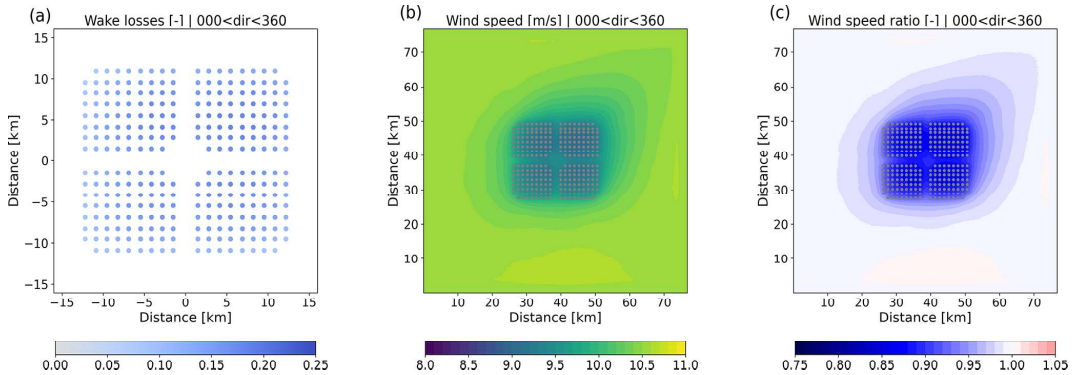

Figure 13. Aerodynamic losses **(a)**, mean 140 m wind speed **(b)**, and ratio of actual to free-stream wind speed **(c)** for the IEA15 scenario (including all data).

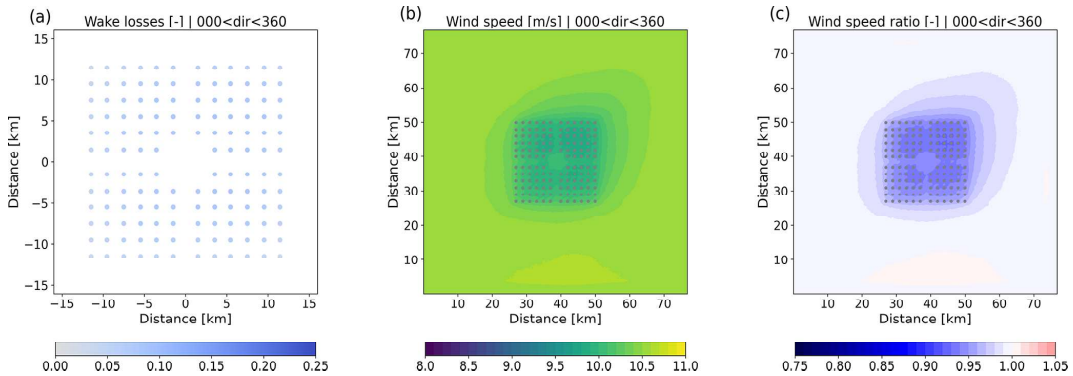

Figure 14. Same as Fig. 13 but for the 5 MW km^{-2} scenario (including all data).

power production, and aerodynamic losses over the wind farms. By breaking down the dataset into bins of wind direction, wind speed, and stability classes, the impact of different atmospheric conditions can be examined. A selection of composite maps of aerodynamic losses, wind speed, and the ratio of actual to free-stream wind speed (taken from the precursor simulation) are presented.

Figure 13 shows aerodynamic losses, mean wind speed, and velocity deficit compared to the free-stream flow for the IEA15 scenario, averaged over the entire year and all wind directions. Losses vary from around 6 % for turbines located at the outer parts of the wind farm to 20 % for turbines in the interior of the wind farm. The dominance of stronger southwesterly winds is reflected in lower losses in the southwestern part of the wind farm and a clear asymmetry in the composite wind fields. The impact of the wind farm on the year-round, omni-directional wind field is on the order of 20 km, after which a velocity deficit of less than 1 % is observed.

For comparison, Fig. 14 shows the results for the 5 MW km^{-2} scenario. As expected, losses are much lower compared to IEA15, which has a capacity density of around 10 MW km^{-2}. This is the combined effect of larger distance between the turbines and the fact that only half the number of turbines is involved. The impact on the mean wind field and the corresponding velocity deficit is smaller as well: in the center of the wind farm the velocity deficit is 6 %, compared to 12 % in the 10 MW km^{-2} case.

Figure 15 presents composite maps for the IEA15 scenario again but now only including data with a wind direction between 15 and 45°. In this case, a clear wake is visible, which is still present as the flow reaches the southern edge of the domain. Clearly, for studying wake lengths behind wind farms of this size, much larger domains are required than the present 80 km. Upstream, the wind speed is already reduced before the flow reaches the wind farm, which signals the presence of blockage. Along the sides, a clear flow acceleration is visible. The distribution of aerodynamic losses over the wind farm shows interesting patterns. Although not in the wake of any other turbines, the first-row turbines in the northeastern corner of the wind farm produce 10 % less power than their "thrustless" equivalents. On the other hand, the turbines in the southeastern part profit from the flow acceleration around the wind farm and produce up to 5 % more power than if they had operated in isolation.

Comparison of Fig. 15 with Fig. 16 clearly illustrates the difference in the flow being oriented to the corner of the wind farm or directly towards the one of the sides. In the case of the latter, the numbers of turbines that are facing undisturbed

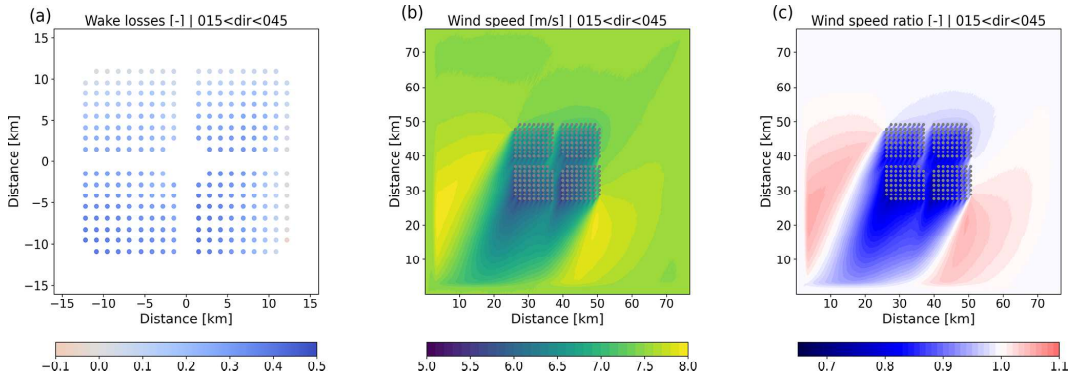

Figure 15. Same as Fig. 13 but only including wind directions between 15 and 45°.

conditions (apart from blockage effects) is much less, resulting in larger aerodynamic losses (cf. Fig. 12).

The different layout of the IJVer scenario results in relatively low aerodynamic losses for easterly flow (Fig. 17). Also here, flow acceleration around the wind farm leads to increased production for, in this particular case, the northernmost turbines.

Finally, Figs. 18 and 19 illustrate the impact of convective and stable conditions, respectively. To enable a "fair" comparison, only conditions with wind speeds between 6 and 10 m s^{-1} are included. As shown before, in this wind speed range the aerodynamic losses are much higher than average. In stably stratified conditions, deeper wakes occur that extend further downstream. Also, the wind speed reduction upstream of the wind farm is larger in stable conditions. This is reflected in larger first-row losses compared to convective conditions. Moreover, going deeper into the wind farm, losses increase faster for stable than for convective conditions: near the southern edge of the wind farm, turbine losses increase to around 60 % for stable conditions, while they are confined to approximately 40 % in convective conditions.

5 Discussion and sensitivity study

To assess production numbers and aerodynamic losses for a suite of hypothetical 4 GW offshore wind farms, a full year of simulations with the LES model GRASP have been performed. Even though GRASP has a relatively high computational performance due to its implementation on GPUs, the computational costs of the simulations are significant. That is to say, in order to enable the atmospheric simulations of large wind farms covering an entire year, the configuration of both the model grid and the domain needs to be carefully selected to limit computational cost while maintaining physically sound results.

Because the applied horizontal grid spacing of 120 m might be considered coarse for an atmospheric LES model and/or for the actuator-disk model that is used, we consider an assessment of the sensitivity of the modeling results appropriate. Therefore, additional simulations have been performed in which we varied the resolution, the prefactor of the subgrid model (governing the magnitude of the subgrid-scale diffusion), and the domain size (both height and horizontal extent). The sensitivity experiments were performed on a smaller domain of 30 720 m. A wind farm of around 770 MW was included. To assess if relative differences between scenarios remained the same, each sensitivity experiment was carried out twice: once with 72 of the IEA10 turbines (regular 9 by 8 array, spacing of 5.6 D) and once with 36 of the Scaled21 turbines (regular 6 by 6 array, spacing of 5.8 D). The sensitivity experiments were not run for the entire year but for a representative subset of 100 d. The 100 d was selected by a k-means clustering method based on the daily mean of the longitudinal and latitudinal components of the ERA5 100 m wind.

Specifically, the following sensitivity experiments have been performed:

- *REF*. This is a reference simulation on a 30 720 m domain of 3000 m height. The horizontal grid spacing was 120 m and the height of the lowest grid box 30 m (as in the main simulations). The number of grid points was 256 in the horizontal and 48 in the vertical.
- *HR*. This is the same as REF but with the horizontal grid spacing set to 60 m. To keep the domain size the same, the number of grid points in the horizontal was increased to 512.
- C_s. This is the same as REF but with the c_s prefactor of the subgrid-scale eddy diffusivity increased by 50 % (see Eq. 5).
- $2L_x$. This is the same as REF but with a twice as large horizontal domain of 61 440 m using 512 grid points in both horizontal directions.
- $2L_z$. This is the same as REF but with the domain height increased to 6000 m using 68 vertical levels.

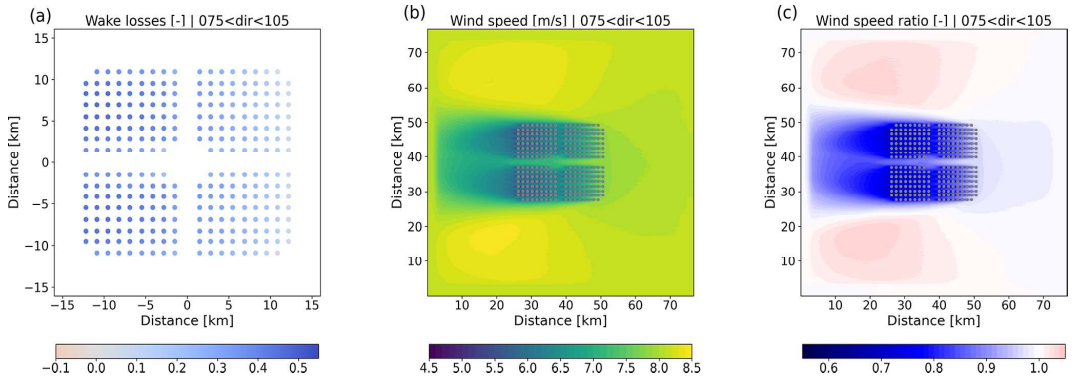

Figure 16. Same as Fig. 13 but only including wind directions between 75 and 105°.

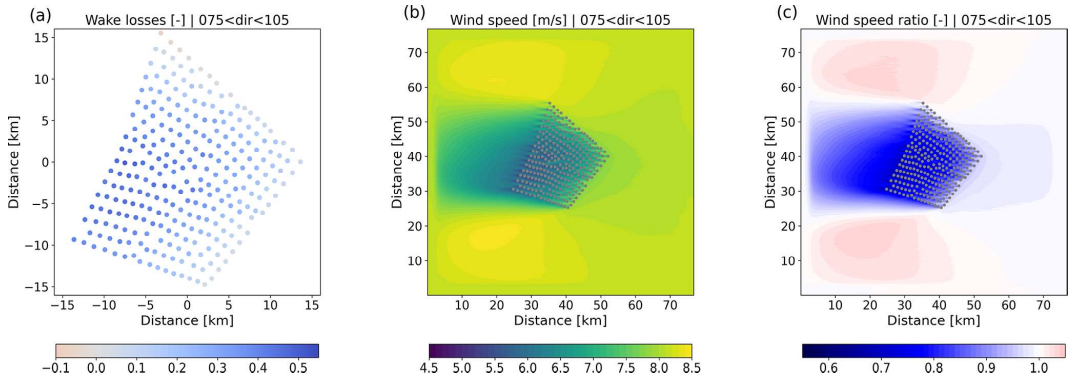

Figure 17. Same as Fig. 13 but for the IJVer scenario, only including wind directions between 75 and 105°.

– $5L_z$. This is the same as REF but with the domain height increased to 14 500 m using 96 vertical levels.

Modifying the modeling setup may impact both the ambient conditions (which will change the thrustless production numbers) and the interaction between the turbines of the wind farm (changing the aerodynamic losses). Figure 20 presents the relative differences between each sensitivity experiment and the REF experiment. Differences in free-stream (thrustless) production are mostly less than 1 %. The same is true for the actual production numbers. Naturally, the aerodynamic losses of the sensitivity experiment are smaller than in the main simulations as the installed capacity is smaller.

Increasing the resolution from 120 to 60 m leads to slightly lower aerodynamic losses. This is expected as at finer resolutions, turbine wakes are more accurately resolved and less smeared out over the grid. Still, the impact is relatively small, especially given the factor-of-8 difference in computational cost (number of points in the domain and a 50 % reduction in the model time step). Increasing the prefactor of the subgrid-scale eddy diffusivity c_s by 50 % increases the subgrid-scale diffusion, logically leading to a decrease in resolved fluctuations. As shown by the c_s experiment, the impact on the aerodynamic losses is small. A common way to assess the validity of a large-eddy simulation is to consider the fraction of resolved turbulence. In our main simulation, the resolved fraction of the momentum flux is larger than 80 % for 70 % of the time (at a height of 150 m, which is the hub height of the IEA15 turbine). For stably stratified conditions the contribution of the subgrid-scale fluxes is larger, but situations where all turbulent fluctuations disappear are rare. In practice, a relatively large (fractional) subgrid-scale contribution may have limited effect, as the absolute values of the turbulent fluxes are small.

The sensitivity experiments were performed for two contrasting wind farm scenarios in order to verify the robustness of the relative differences between the scenarios. Figure 20b indicates that while the aerodynamic losses may change a bit between the sensitivity experiments, the two scenarios show similar patterns. This gives confidence in the comparison between different scenarios in Sect. 4.

It can be argued that the impact of the sensitivity experiments as discussed above is masked by the fact that for wind speed above 14 m s^{-1} (related to 50 % of the production), losses are negligible anyway (cf. Fig. 6). Therefore, Fig. 21 presents relative aerodynamic losses for disk-averaged wind speeds between 6 and 10 m s^{-1}. As expected, aerodynamic losses for this specific wind speed range are higher than the overall losses, as are the differences between the scenarios. Still, differences with the REF simulations remain within

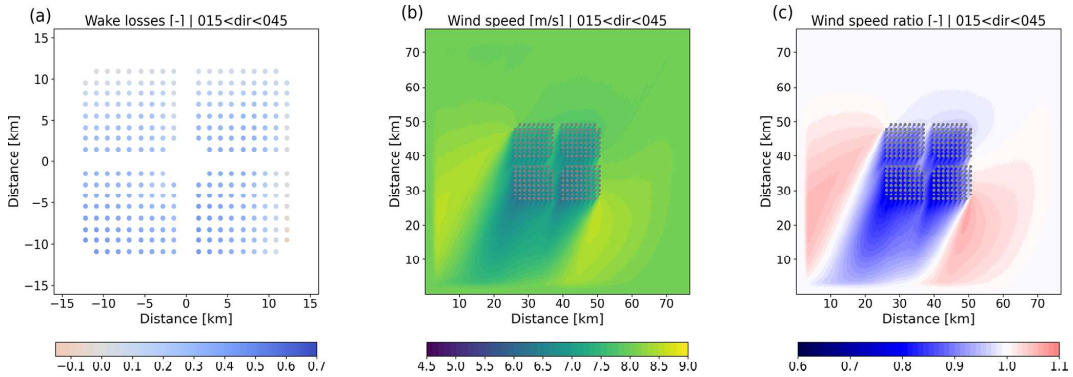

Figure 18. Same as Fig. 13 but only including convective conditions, wind speeds between 6 and 10 m s^{-1}, and wind directions between 15 and 45°.

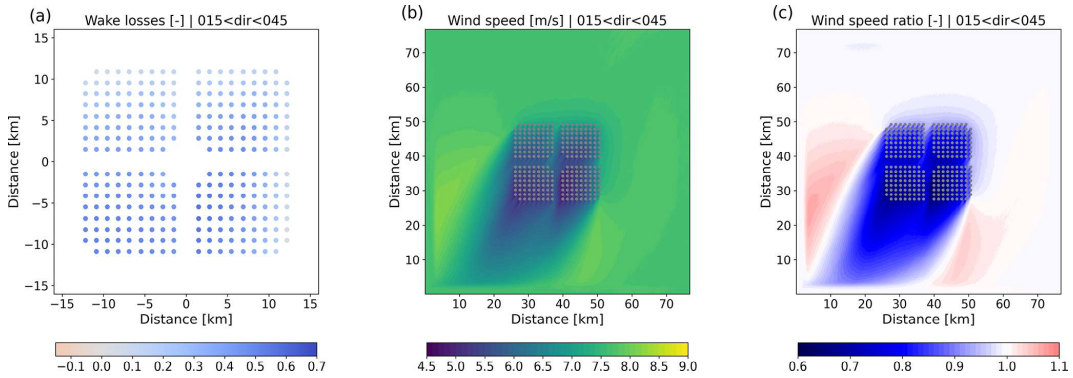

Figure 19. Same as Fig. 13 but only including stable conditions, wind speeds between 6 and 10 m s^{-1}, and wind directions between 15 and 45°.

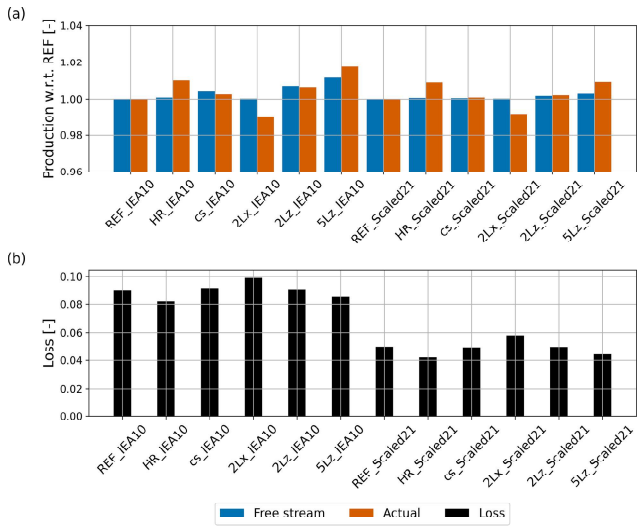

Figure 20. Free-stream and actual production of the sensitivity experiments with respect to REF (**a**) and the corresponding aerodynamic losses (**b**).

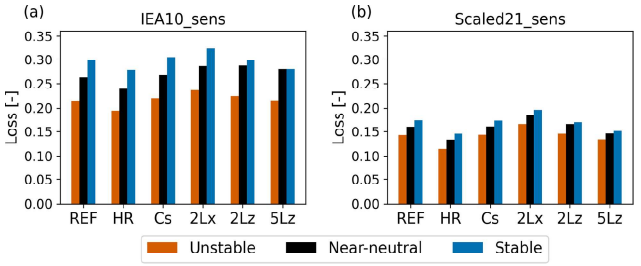

Figure 21. Stability-dependent aerodynamic losses for disk-averaged wind speeds between 6 and 10 m s^{-1} for the IEA10 (**a**) and Scaled21 (**b**) sensitivity experiments.

reasonable limits. Presented numbers are for the three stability classes defined above. The differences between the stability classes are similar for the different sensitivity experiments. This gives confidence in the analysis on the impact of stability in the main Results section.

Increasing the horizontal and increasing the vertical extent of the domain both have a modest impact on the production numbers and aerodynamic losses. With a twice-as-large horizontal domain, the aerodynamic losses become slightly

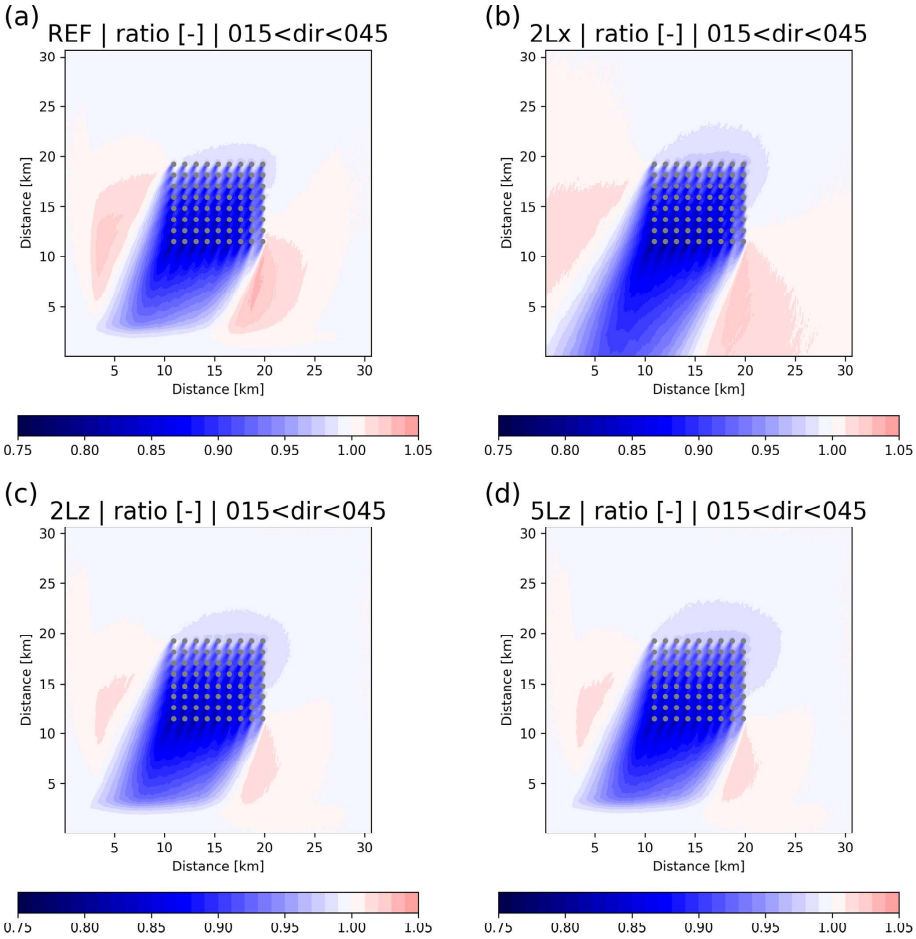

Figure 22. Ratio of actual to free-stream 142 m wind speed for the REF **(a)**, the $2L_x$ **(b)**, the $2L_z$ **(c)**, and the $5L_z$ **(d)** IEA10 sensitivity experiments for wind directions between 15 and 45°.

higher. This may be related to the additional space around the wind farms, reducing the tendency of the flow to accelerate along the wind farm's edges.

Recently, several LES wind farm studies have argued that for a proper modeling of flow through large wind farms, large domain heights (usually more than 10 km) are required. In particular, these large domain heights would be needed for a proper modeling of wind-farm-induced gravity waves and their impact on blockage effects and production numbers (e.g., Allaerts and Meyers, 2017; Lanzilao and Meyers, 2022). Therefore, we performed two sensitivity simulations with increased domain height: one with a height of 6 km ($2L_z$) and one with a height of 14.5 km ($5L_z$). The results presented in Figs. 20 and 21 do not indicate a significant sensitivity of our results to the domain height (in contrast, explorative model simulations in the early stages of the present study indicated that reducing the domain height to, for instance, 2000 m does have a clear impact on the results).

In addition, Fig. 22 shows the impact of the domain configuration on the ratio of actual to free-stream 140 m wind speeds for wind directions between 15 and 45°. For comparison, the results of the $2L_x$ simulation are cropped to the extent of the REF domain. While the evolution of the wake is comparable to the REF simulation, in the $2L_x$ simulation the flow acceleration along the edges of the wind farm is weaker. The same effect can be seen when the domain height is increased from 3000 to 6000 m ($2L_z$). Increasing the domain height even further, to 14 500 m ($5L_z$), has a negligible effect on the flow field. This is true for both the downstream evolution of the wake and the reduction in the wind speed upstream of the wind farm.

The relatively small impact of the domain height reported here may be somewhat surprising given the findings of the studies cited above. However, it could well be that in our study the impact of, for instance, gravity waves is masked by the large variety of synoptic forcings and boundary layer conditions associated with 1 year of actual weather.

The sensitivity experiments discussed in this section give a clear indication of the robustness of the presented results: modifying grid spacing, settings of the subgrid model, and the extent of the domain within reasonable margins will likely change the results to several percent at maximum.

Overall, we argue that the sensitivity experiments presented here do not invalidate the reasoning and conclusions discussed in the Results section.

Also, from a broader perspective, the sensitivities described here are not larger than, for instance, sensitivities that are reported in studies with mesoscale models that use wind farm parameterizations like the Fitch et al. (2012) parameterization and/or the explicit wake parameterization of Volker et al. (2015) as discussed in, for example, Pryor et al. (2019) and Fischereit et al. (2022). In addition, engineering models rely on calibration on wind farms with much smaller installed capacities as discussed in the present work, and extrapolation to large wind farms is not straightforward. For example, Maas and Raasch (2022) demonstrate that flow dynamics for multi-gigawatt wind farms may differ significantly from those for smaller-scale wind farms.

6 Conclusions

In this work we studied production numbers and aerodynamic losses for six hypothetical 4 GW offshore wind farm scenarios using the GRASP large-eddy simulation model. The six scenarios differed in terms of applied turbine type (e.g., $2n \times 10$ MW turbines versus $n \times 20$ MW turbines), installed capacity density (5 MW km^{-2} versus 10 MW km^{-2}), and layout. For each scenario, a 1-year GRASP simulation was performed using 2015 meteorological large-scale conditions taken from ECMWF's ERA5 reanalysis dataset.

The results suggest that, for the simulated year, aerodynamic losses for a 4 GW offshore wind farm vary from 12 % for 21 MW turbines to 18 % for 10 MW turbines. Moreover, even for turbine types with similar rated capacity but slightly different power and thrust curves, energy production may vary by as much as 7.7 %.

For all considered scenarios, 80 % of the aerodynamic losses occur in a narrow wind speed range of 8 to 12 m s^{-1}. On the other hand, 50 % of the energy production occurs without any aerodynamic losses when all turbines operate at rated capacity. Naturally, these specific numbers should be viewed in the context of the wind speed probability density function considered and the wind turbine design choices (power curves).

Although wind speed is identified as the most important factor determining aerodynamic losses, we were able to isolate the impact of stability. A fair assessment of this impact seemed possible by only considering wind speeds between 6 and 10 m s^{-1}. In this wind speed range, aerodynamic losses may be 10 percentage points larger for stably stratified conditions compared to convective conditions. Numbers vary per scenario with larger differences for scenarios with higher overall losses.

Losses of first-row turbines, which are related to the global-blockage effect, were found to be 2 % to 3 % in general. These values are consistent with values of the blockage effect reported in the literature. As with the general losses, also the first-row losses occur in a narrow range of disk-averaged wind speeds. Also, a clear impact of stability is identified. For example, for disk-averaged wind speeds between 6 and 10 m s^{-1}, first-row losses may increase to almost 10 % in stably stratified conditions.

The complexity of disentangling the effect of wind speed and stability is illustrated by considering direction-dependent aerodynamic losses. Only when selecting proper wind speed conditions does a clear impact of stability and of the geometry of the respective scenarios become apparent. For instance, when the flow is facing the corners of a square-shaped wind farm, losses are clearly lower than when the flow is directed towards the faces of the wind farm.

Sensitivity experiments were carried out to better understand the impact of various modeling choices such as resolution and domain height. Results suggest that overall energy production varies with 1 % to 2 % depending on model settings and/or the domain configuration. Relative differences between the IEA10 and Scaled21 turbine scenario are robust.

In summary, using a high-fidelity modeling technique, the results presented in this explorative study provide a clear indication of the performance of future, multi-gigawatt wind farms for 1 year of realistic weather conditions. Further research could address several open questions like the influence of the lateral boundary conditions, inter-wind-farm wake effects, and more validation against meteorological observations and wind farm data. More elaborate validation studies could also shed more light on the resolution dependence of the aerodynamic losses.

Data availability. The GRASP large-eddy simulation dataset is available from the authors on request.

Author contributions. PB performed the model simulation, analyzed the results, and wrote the manuscript. RV, PvD, and HJ provided ideas, corrections, and modifications. PvD implemented and calibrated the actuator-disk model. HJ is the main developer of the GRASP model.

Competing interests. The contact author has declared that none of the authors has any competing interests.

Disclaimer. Publisher's note: Copernicus Publications remains neutral with regard to jurisdictional claims in published maps and institutional affiliations.

Acknowledgements. The MSc projects of Sebastiaan Ettema and Thijs Bon (Delft University of Technology) on the global-blockage phenomenon provided inspiration and insights for the present work. The constructive comments of the referees are highly appreciated.

Financial support. This research has been supported by the Rijksdienst voor Ondernemend Nederland via the Top Sector Energy project Winds of the North Sea in 2050 (WINS50) (grant no. TEWZ119007).

Review statement. This paper was edited by Cristina Archer and reviewed by Oliver Maas and three anonymous referees.

References

Allaerts, D. and Meyers, J.: Boundary-layer development and gravity waves in conventionally neutral wind farms, J. Fluid Mech., 814, 95–130, https://doi.org/10.1017/jfm.2017.11, 2017.

Allaerts, D., Vanden Broucke, S., Van Lipzig, N., and Meyers, J.: Annual impact of wind-farm gravity waves on the Belgian–Dutch offshore wind-farm cluster, J. Phys.: Conf. Ser., 1037, 072006, https://doi.org/10.1088/1742-6596/1037/7/072006, 2018.

Bleeg, J., Purcell, M., Ruisi, R., and Traiger, E.: Wind farm blockage and the consequences of neglecting its impact on energy production, Energies, 11, 1609, https://doi.org/10.3390/en11061609, 2018.

Böing, S.: The interaction between deep convective clouds and their environment, PhD thesis, TU Delft, https://doi.org/10.4233/uuid:aa9e6037-b9cb-4ea0-9eb0-a47bf1dfc940, 2014.

Calaf, M., Meneveau, C., and Meyers, J.: Large eddy simulation study of fully developed wind-turbine array boundary layers, Phys. Fluids, 22, 1–16, https://doi.org/10.1063/1.862466, 2010.

Charnock, H.: Wind stress on a water surface, Q. J. Roy. Meteorol. Soc., 81, 639–640, 1955.

ECMWF: IFS Manual Part IV: Physical Processes. IFS Documentation Cy43R3, Tech. rep., ECMWF, https://www.ecmwf.int/en/elibrary/17736-part-iv-physical-processes (last access: 18 May 2023), 2017.

European Commission: Offshore Renewable Energy Strategy, https://energy.ec.europa.eu/topics/renewable-energy/eu-strategy-offshore-renewable-energy_en (last access: 18 May 2023), 2020.

Fischereit, J., Brown, R., Gia Larsen, X., Badger, J., and Hawkes, G.: Wind farm wakes simulated using WRF, Bound.-Lay. Meteorol., 182, 175–224, 2022.

Fitch, A., Olson, J., Lundquist, J., Dudhia, J., Gupta, A., Michalakes, J., and Barstad, I.: Local and mesoscale impacts of wind farms as parameterized in a mesoscale NWP Model, Mon. Weather Rev., 140, 3017–3038, https://doi.org/10.1175/MWR-D-11-00352.1, 2012.

Grabowski, W.: Toward Cloud Resolving Modeling of Large-Scale Tropical Circulations: A Simple Cloud Microphysics Parameterization, J. Atmos. Sci., 55, 3283–3298, 1998.

Hersbach, H., Bell, B., P., B., Hirahara, S., Horányi, A., Muñoz-Sabater, J., Nicolas, J., Peubey, C., Radu, R., Schepers, D., Simmons, A., Soci, C., Abdalla, S., Abellan, X., Balsamo, G., Bechtold, P., Biavati, G., Bidlot, J., Bonavita, De Chiara, G., Dahlgren, P., Dee, D., Diamantakis, M., Dragani, R., Flemming, J., Forbes, R., Fuentes, M., Geer, A., Haimberger, L., Healy, S., Hogan, R., Hólm, E., Janisková, M., Keeley, S., Laloyaux, P., Lopez, P., Lupu, C., Radnoti, G., De Rosnay, P., Rozum, I., Vamborg, F., Villaume, S., and Thépaut, J.: The ERA5 global reanalysis, Q. J. Roy. Meteorol. Soc., 146, 1999–2049, https://doi.org/10.1002/qj.3803, 2020.

Heus, T., Van Heerwaarden, C. C., Jonker, H. J. J., Siebesma, A. P., Axelsen, S., Van Den Dries, K., Geoffroy, O., Moene, A. F., Pino, D., De Roode, S. R., and Vila-Guerau de Arellano, J.: Formulation of the Dutch Atmospheric Large-Eddy Simulation (DALES) and overview of its applications, Geosci. Model Dev., 3, 415–444, https://doi.org/10.5194/gmd-3-415-2010, 2010.

Khairoutdinov, M. and Randall, D.: Cloud Resolving Modeling of the ARM Summer 1997 IOP: Model Formulation, Results, Uncertainties, and Sensitivities, J. Atmos. Sci., 60, 607–625, 2003.

Lanzilao, L. and Meyers, J.: Effects of self-induced gravity waves on finite wind-farm operations using a large-eddy simulation framework, J. Phys.: Conf. Ser., 2265, 022043, https://doi.org/10.1088/1742-6596/2265/2/022043, 2022.

Maas, O. and Raasch, S.: Wake properties and power output of very large wind farms for different meteorological conditions and turbine spacings: A large-eddy simulation case study for the German Bight, Wind Energ. Sci., 7, 715–739, https://doi.org/10.5194/wes-7-715-2022, 2022.

Mehta, D., van Zuijlen, A. H., Koren, B., Holierhoek, J. G., and Bijl, H.: Large Eddy Simulation of wind farm aerodynamics: A review, J. Wind Eng. Indust. Aerodynam., 133, 1–17, https://doi.org/10.1016/j.jweia.2014.07.002, 2014.

Meyers, J. and Meneveau, C.: Large Eddy Simulations of Large Wind-Turbine Arrays in the Atmospheric Boundary Layer, in: 48th AIAA Aerospace Sciences Meeting Including the New Horizons Forum and Aerospace Exposition, 4–7 January 2010, Orlando, Florida, USA, 1–10, https://doi.org/10.2514/6.2010-827, 2010.

Neggers, R. A. J., Siebesma, A. P., and Heus, T.: Continuous single-column model evaluation at a permanent meteorological supersite, B. Am. Meteorol. Soc., 93, 1389–1400, https://doi.org/10.1175/BAMS-D-11-00162.1, 2012.

Porté-Agel, F., Bastankhah, M., and Shamsoddin, S.: Wind-Turbine and Wind-Farm Flows: A Review, Bound.-Lay. Meteorol., 174, 1–59, https://doi.org/10.1007/s10546-019-00473-0, 2020.

Pryor, S., Shepard, T., Bartherlmie, R., Hahmann, A., and Volker, P.: Wind farm wakes simulated using WRF, J. Phys.: Conf. Ser., 1256, 012025, https://doi.org/10.1088/1742-6596/1256/1/012025, 2019.

Rozema, W., Bae, H. J., Moin, P., and Verstappen, R.: Minimum-dissipation models for large-eddy simulation, Phys. Fluids, 27, 085107, https://doi.org/10.1063/1.4928700, 2015.

RVO: General Information IJmuiden Ver, https://offshorewind.rvo.nl/cms/view/5c06ac88-c12f-4903-89f3-27d66937b7e9/general-information-ijmuiden-ver (last access: 18 May 2023), 2022.

Schalkwijk, J., Griffith, E. J., Post, F. H., and Jonker, H. J. J.: High-performance simulations of turbulent clouds on a desktop PC, B. Am. Meteorol. Soc., 93, 307–314, 2012.

Schalkwijk, J., Jonker, H., Siebesma, A., and Van Meijgaard, E.: Weather forecasting using GPU-based large-Eddy simulations, B. Am. Meteorol. Soc., 96, 715–723, https://doi.org/10.1175/BAMS-D-14-00114.1, 2015a.

Schalkwijk, J., Jonker, H. J. J., Siebesma, A. P., and Bosveld, F. C.: A Year-Long Large-Eddy Simulation of the Weather

over Cabauw: an Overview, Mon. Weather Rev., 143, 828–844, https://doi.org/10.1175/MWR-D-14-00293.1, 2015b.

Schneemann, J., Theuer, F., Rott, A., Dörenkämper, M., and Kühn, M.: Offshore wind farm global blockage measured with scanning lidar, Wind Energ. Sci., 6, 521–538, https://doi.org/10.5194/wes-6-521-2021, 2021.

Stevens, R. J. and Meneveau, C.: Flow Structure and Turbulence in Wind Farms, Annu. Rev. Fluid Mech., 49, 311–339, https://doi.org/10.1146/annurev-fluid-010816-060206, 2017.

Stevens, R. J., Graham, J., and Meneveau, C.: A concurrent precursor inflow method for Large Eddy Simulations and applications to finite length wind farms, Renew. Energy, 68, 46–50, https://doi.org/10.1016/j.renene.2014.01.024, 2014.

Strickland, J., Srinidhi, N., and Stevens, R.: Wind farm blockage in a stable atmospheric boundary layer, Renew. Energy, 197, 50–58, https://doi.org/10.1016/j.renene.2022.07.108, 2022.

The Esbjerg Declaration: The Esbjerg Declaration on The North Sea as a Green Power Plant of Europe, https://open.overheid.nl/documenten/ronl-1e299d084fbc5bfc2968d934ca2f4a97b3931d9f/pdf (last access: 18 May 2023), 2022.

Veers, P., Dykes, K., Lantz, E., Barth, S., Bottasso, C. L., Carlson, O., Clifton, A., Green, J., Green, P., Holttinen, H., Laird, D., Lehtomäki, V., Lundquist, J. K., Manwell, J., Marquis, M., Meneveau, C., Moriarty, P., Munduate, X., Muskulus, M., Naughton, J., Pao, L., Paquette, J., Peinke, J., Robertson, A., Rodrigo, J. S., Sempreviva, A. M., Smith, J. C., Tuohy, A., and Wiser, R.: Grand challenges in the science of wind energy, Science, 366, eaau2027, https://doi.org/10.1126/science.aau2027, 2019.

Verzijlbergh, R. A.: Atmospheric flows in large wind farms, Europhys. News, 52, 20–23, https://doi.org/10.1051/epn/2021502, 2021.

Volker, P., Badger, J., Hahmann, A., and Ott, S.: The explicit wake parametrisation V1.0: a wind farm parametrisation in the mesoscale model WRF, Geosci. Model Dev., 8, 3715–3731, https://doi.org/10.5194/gmd-8-3715-2015, 2015.

Wu, K. and Porté-Agel, F.: Flow Adjustment Inside and Around Large Finite-Size Wind Farms, Energies, 10, 2164, https://doi.org/10.3390/en10122164, 2017.

Journal of Physics: Conference Series

PAPER • **OPEN ACCESS**

Can mesoscale models capture the effect from cluster wakes offshore?

To cite this article: Miguel Sanchez Gomez *et al* 2024 *J. Phys.: Conf. Ser.* **2767** 062013

Journal of Physics: Conference Series **2767** (2024) 062013 doi:10.1088/1742-6596/2767/6/062013

Can mesoscale models capture the effect from cluster wakes offshore?

Miguel Sanchez Gomez[1], Georgios Deskos[1], Julie K. Lundquist[1,2] and Timothy W. Juliano[3]

[1] National Renewable Energy Laboratory, Golden, Colorado, USA
[2] University of Colorado, Boulder, Colorado, USA
[3] U.S. NSF National Center for Atmospheric Research, Boulder, Colorado, USA

E-mail: [redacted]@nrel.gov

Abstract. Long wakes from offshore wind turbine clusters can extend tens of kilometers downstream, affecting the wind resource of a large area. Given the ability of mesoscale numerical weather prediction models to capture important atmospheric phenomena and mechanisms relevant to wake evolution, they are often used to simulate wakes behind large wind turbine clusters and their impact over a wider region. Yet, uncertainty persists regarding the accuracy of representing cluster wakes via mesoscale models and their wind turbine parameterizations. Here, we evaluate the accuracy of the Fitch wind farm parameterization in the Weather Research and Forecasting model in capturing cluster-wake effects using two different options to represent turbulent mixing in the planetary boundary layer. To this end, we compare operational data from an offshore wind farm in the North Sea that is fully or partially waked by an upstream array against high-resolution mesoscale simulations. In general, we find that mesoscale models accurately represent the effect of cluster wakes on front-row turbines of a downstream wind farm. However, the same models may not accurately capture cluster-wake effects on an entire downstream wind farm, due to misrepresenting internal-wake effects.

1. Introduction

Wakes from offshore wind turbine clusters, also referred to as cluster wakes, can propagate long distances, reducing the power production of downstream wind farms [1, 2]. Power losses associated with the effect of cluster wakes have historically been underestimated, leading to uncertainty in energy yield estimates [3].

Analytical and numerical models can be used to estimate losses from cluster wakes and reduce uncertainty in wind farms' energy production assessments. Due to their low computational cost, engineering wake models are commonly used to quantify both wake and power losses. However, these simplified models do not account for some key physical mechanisms that can modify wake evolution in an offshore environment [4, 5]. High-fidelity simulations, like large-eddy simulations (LES), can provide a more complete representation of wake physics [6]; however, at a considerably higher computational cost. Mesoscale numerical weather prediction models, on the other hand, represent well the physical conditions (such as atmospheric stability) that may impact wake evolution—and at a lower computational cost than LES. Nevertheless, uncertainty persists regarding the precision of mesoscale models in accurately representing the impact of wind turbines in the atmospheric boundary layer [7, 8, 9, 10].

Mesoscale simulations rely on the assumption that the size of the most energetic turbulent structures (l) is much smaller than the horizontal grid spacing (Δx) of the model (i.e., $\Delta x >> l$); as such, the effects of turbulence are parameterized. Vertical turbulence mixing at the subgrid scale is typically modeled by assuming horizontal homogeneity using planetary boundary-layer (PBL) parameterizations. In coarse mesoscale simulations ($\Delta x \sim 10$ km), the horizontal gradients of momentum and heat are small compared to their vertical gradients. However, in high-resolution mesoscale simulations ($\Delta x \sim l$), commonly referred to as *gray zone* or *terra incognita* simulations, the most energetic turbulent eddies are not fully parameterized and horizontal gradients of mean quantities become important [11, 12, 13]. Wind turbine and wind farm wakes are characterized by large horizontal and vertical momentum gradients. Consequently, horizontal gradients of turbulence statistics become non-negligible and the three-dimensional effects of turbulence should be considered. In addition, turbine-scale effects (i.e., momentum extraction and enhanced turbulence mixing), which are on the order of 100 m, must also be parameterized. Wind turbines in mesoscale models are typically parameterized as momentum sinks, such as in the Fitch Wind Farm Parameterization (WFP) [14] and the Explicit Wake Parameterization (EWP) [15], or as enhanced surface roughness [16], which misrepresents the wake structure downstream of the turbines [17].

In this study, we evaluate the ability of the Fitch WFP to represent wakes from offshore wind turbines. In particular, we investigate its ability—when used in conjunction with two different PBL schemes, namely the MYNN [18] and the three-dimensional (3D) PBL [13, 19] schemes—to estimate power losses due to external and internal wakes as compared with operational data from an offshore wind farm. The remainder of this paper is organized as follows. In Section 2, we describe the wind farm operational data used to validate the mesoscale simulations. Section 3 provides an overview of the numerical methods employed herein. The climatology of winds around the wind farms of interest is outlined in Section 4. The effects of cluster wakes on downstream wind farms is detailed in Section 5, and a summary and next steps are provided in Section 6.

2. Wind turbine power data

We use wind turbine operational data from offshore wind farms in the North Sea to validate cluster-wake effects in mesoscale models. Specifically, we assess the interaction between the Westermost Rough and Humber Gateway wind farms. Westermost Rough is located approximately 19 km northwest of the Humber Gateway wind farm (Figure 1). The Westermost Rough wind farm comprises 35 Siemens 6-MW wind turbines with hub height at 102 m and 154-m rotor diameter. The Humber Gateway wind farm comprises 73 Vestas 3-MW wind turbines with hub height at 80 m and 112-m rotor diameter. Turbine power data from the Supervisory Control and Data Acquisition system (SCADA) from Westermost Rough between January and December, 2017, are used to validate power production estimates calculated by the mesoscale model. Power production, nacelle wind speed, turbine yaw angle, and fault conditions are provided by the wind farm operator for each turbine as 10-min averages. All turbines in Humber Gateway are assumed to be operating normally for the analysis.

SCADA data filtering is performed using the FLOw Redirection and Induction in Steady State (FLORIS)-based Analysis for SCADA data (FLASC) tool [20]. We filter out power outliers for each turbine based on curtailment, mean-power-curve outliers, sensor-stuck faults, and non-normal operations. On average for all turbines in the wind farm, 77.9% of the data remain valid after discarding outliers. Furthermore, the yaw angle for each turbine is calibrated to true north in FLASC using FLORIS with the Gaussian wake model.

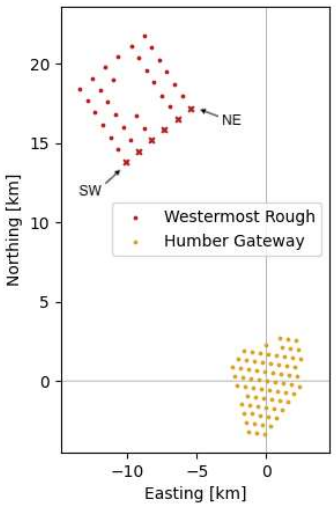

Figure 1. Relative location of the Westermost Rough and Humber Gateway wind farms. Front-row turbines in Westermost Rough for southeasterly winds are shown with crosses. The Southwest (SW) and Northeast (NE) front-row turbines (for southeasterly winds) of Westermost Rough are shown for reference. Relative distances are calculated from the center of the Humber Gateway wind farm.

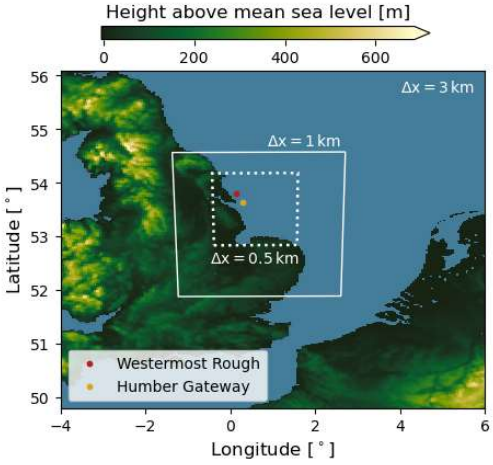

Figure 2. Domain layout for the WRF simulations. The solid and dotted white rectangles represent the location and size of the nested domain for the $\Delta x = 1$ km and $\Delta x = 0.5$ km simulations, respectively, within the parent domain ($\Delta x = 3$ km).

3. Numerical Models

We simulate atmospheric flow around these two wind farms in the North Sea using the Weather Research and Forecasting (WRF) model (Version 4.4) using a two-domain, one-way nesting setup (Figure 2). ERA5 reanalysis [21] provides initial and boundary conditions to the outer ($\Delta x = 3$ km) mesoscale domain. For the nested mesoscale domain, we perform simulations using two horizontal grid spacings, one with $\Delta x = 1$ km (solid white line in Figure 2) and another with $\Delta x = 0.5$ km (dotted white line in Figure 2). The physical characteristics and modeling options of the domains are provided in Table 1.

Two boundary-layer parameterizations are used to model turbulent mixing in the lowest portion of the atmosphere. The one-dimensional 2.5-MYNN boundary-layer parameterization (MYNN from hereafter) [18] is used with $\Delta x = 1$ km, whereas a 3D boundary-layer parameterization (3D PBL from hereafter) [13, 19] is employed with $\Delta x = 0.5$ km. For completeness, we also perform simulations using the 3D PBL for a nested domain with $\Delta x = 1$ km. The MYNN parameterization estimates vertical turbulent mixing using the vertical turbulent stress divergence, whereas horizontal mixing is computed with a Smagorinsky-like approach. In contrast, the 3D PBL explicitly computes both the vertical and horizontal turbulent flux divergence for momentum, heat, and moisture. Here, we use the "boundary-layer approximation" to the 3D PBL, where vertical turbulent fluxes are calculated like in MYNN,

Domain	Δx [km]	Δz_s [m]	(n_x, n_y, n_z)	α [-]	PBL Model
d01	3.0	8	$(241, 241, 79)$	-	MYNN
d02	1.0	8	$(265, 301, 79)$	$[0.0, 0.5, 1.0]$	MYNN
				1.0	3D PBL
	0.5	8	$(265, 301, 79)$	1.0	3D PBL

Table 1. Simulation setup, including horizontal grid resolution (Δx), vertical resolution at the surface (Δz_s), number of grid cells along each direction (n_i), correction factor for the fraction of turbine-added TKE (α), and boundary-layer parameterization for each domain.

and the horizontal turbulent fluxes are calculated analytically following [22], as in [23, 24]. We found the full matrix solution to the turbulent fluxes to be numerically unstable in our test cases. Model closure constants and the master length scale follow the original Mellor–Yamada model [22]. Additional information on the "full" 3D PBL and its "boundary-layer approximation" can be found in Juliano et al. [13].

We simulate the wind turbines exclusively in the nested domain (d02) using the Fitch WFP [14, 25, 23]. The Fitch parameterization represents the effect of wind turbines through a momentum sink and a source of turbulence kinetic energy (TKE). The drag from the turbines on the flow is a function of the thrust coefficient, the number of turbines per grid cell, and the turbine size (i.e., rotor diameter D). The Fitch wind farm parameterization postulates that a fraction of the energy from the flow is converted into increased turbulent motions; thus, the parameterization adds a source to the TKE tendency equation as well. Turbine-added TKE is regulated in the model as $C_{TKE} = \alpha(C_T - C_P)$, where α is a correction factor, and C_T and C_P are the turbine's thrust and power coefficients, respectively, which in turn are a function of inflow wind speed. We explore the sensitivity to the turbine-added TKE in the MYNN simulations by varying α between 0 and 1. Because the average turbine spacing in Westermost Rough and Humber Gateway is 945 m and 580 m, respectively, multiple wind turbines are expected to occupy one grid cell for the $\Delta x = 1$ km domain (Figure 3a). Furthermore, due to the domain discretization and because the effect of the turbines is placed at the grid cell center, the effective wind farm layout of Westermost Rough and Humber Gateway in our simulations (Figure 3) may differ from their physical location (Figure 1). A more accurate representation of each farm's layout is obtained with finer resolution (Figure 3b).

4. Climatology of winds in the region

We characterize the climatology of winds in the region using nacelle-anemometer wind speed and turbine yaw angle (corrected to true north) recorded in SCADA for the turbines in Westermost Rough. Cluster wakes from Humber Gateway are expected to impact Westermost Rough for wind directions between 130° and 170° [26], when both wind farms are partially or fully aligned. Consequently, we focus on these wind sectors. Furthermore, we focus our analysis on winds above cut-in speed and below rated speed (4 m s^{-1} and 13 m s^{-1}, respectively, for the Siemens 6-MW turbine). Rather than replicating the observations on a case-by-case basis, which is highly sensitive to accurately reproducing the temporal evolution of atmospheric conditions, we use ERA5 reanalysis to find times when the statistics of wind speed and direction are comparable to SCADA and simulate those cases in WRF.

To evaluate the capability of mesoscale models in representing cluster wakes, we perform numerical simulations of 42 cases in 2017 that reproduce the statistics of wind speed and direction near the Westermost Rough wind farm. For each case, the parent domain spins up for 14 hr before initializing the nested domain. We discard the first 5 hr of simulation data for the

nested domain. Three-dimensional wind speed and temperature fields, as well as turbine power production, are output every 5 min for 10 hr after spinup of both domains is complete. Note that winds in the mesoscale simulations are expected to be different from the ERA5 reanalysis. ERA5 data is obtained from the ECMWF's Integrated Forecasting System, which employs a different dynamical core, grid resolution, and parameterizations of physical processes from WRF. Thus, even though WRF is forced using ERA5 data, it will reach its own resolved state away from the domain boundaries.

We use the Perkins Skill Score (PSS) [27] to determine a continuous range of wind speeds and directions where wind statistics in the observations and simulations are similar. The PSS is defined as the cumulative minimum value of two distributions of a binned value, measuring the common area between two probability distributions. Here, we compare the conditional probability distributions for wind speed (U_i) and wind direction (ϕ_j) bins from observations (Z_o) and model results (Z_m), as shown in Eq. 1. For the mesoscale simulations, we use wind speed and direction for the grid points closest to the front-row turbines in Westermost Rough.

$$PSS = \sum_{U_i} \sum_{\phi_j} \min\{Z_m(U_i, \phi_j), Z_o(U_i, \phi_j)\} \tag{1}$$

The climatology of winds (i.e., wind speed and direction) near the Westermost Rough wind farm is well represented in the WRF simulations for a range of wind speeds and directions. We calculate the PSS score for different combinations of wind speed and wind direction bins, then find the continuous range of wind speed and directions that maximize the correspondence between the simulations and observations (i.e., PSS score). Note that variations in the cluster-wake effect may influence the model's ability to reproduce the climatology of this site. The PSS score for the conditional probabilities from WRF and SCADA is 0.75 for wind speeds between [6 m s^{-1}, 9.5 m s^{-1}] and wind directions between [130°, 170°], suggesting simulations capture about 75% of the observed probability density functions. Kolmogorov-Smirnov and Chi-Squared tests indicate the statistics of winds in the MYNN and 3D PBL simulations match the statistics of the SCADA data at a 95% confidence level. Moreover, even though the $\Delta x = 0.5$ km domain is smaller than the $\Delta x = 1$ km domain, resulting in different boundary conditions, the statistics of wind speed and direction are still well captured. Approximately 1900 data points of filtered data from SCADA (10-min averages) lay within these wind speed and direction ranges. Similarly, more than 1300 data points from the WRF simulations (data every 5 min) satisfy

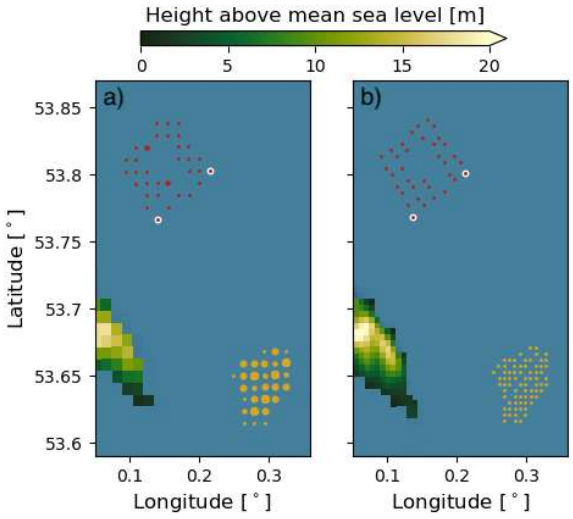

Figure 3. Simulated turbine locations in the WRF grid for the $\Delta x = 1$ km (a) and $\Delta x = 0.5$ km (b) simulations. Multiple turbines located on the same grid cell are represented by larger circles. The edge-most turbines in the front row of Westermost Rough (for southeasterly winds) are highlighted using white circles.

these wind conditions. Note that we use ERA5 reanalysis to find cases when winds at 100 m are between 4 m s^{-1} and 13 m s^{-1}. However, the mesoscale simulations only capture the statistics accurately for wind speeds between 6 m s^{-1} and 9.5 m s^{-1}. The remaining analysis is restricted to winds with a speed between 6 m s^{-1} and 9.5 m s^{-1} and direction between 130° and 170° only.

5. Cluster-wake effects

5.1. Front-row turbines

We quantify cluster-wake effects from Humber Gateway on downstream wind turbines using the average of the ratio of power production from the edge-most, front-row turbines in the Westermost Rough wind farm (turbines SW and NE in Figure 1). This power-ratio metric is accurate for quantifying partially waked conditions for Westermost Rough [26]. The southwest turbine in the front row of Westermost Rough (P_{SW}) is expected to generate more power than the northeast turbine in the front row (P_{NE}) for wind directions around 145°, and vice versa for wind directions around 165° [26].

Mesoscale simulations accurately represent cluster-wake effects on front-row turbines in the Westermost Rough wind farm (Figure 4). In general, all mesoscale simulations display the same trend in the power ratio when compared to SCADA data. The southwest turbine (SW) in Westermost Rough is waked by Humber Gateway for wind direction sectors between 130° and 155°, whereas the northeast turbine (NE) is waked by Humber Gateway for wind direction sectors between 155° and 170°.

The MYNN ($\alpha = 1$) and 3D PBL ($\Delta x = 1$ km) model configurations show the best agreement with the observational data (Figure 4). The power ratio obtained from SCADA is statistically different (95% confidence) from the power ratio predicted using MYNN ($\alpha = 1$) only when the winds have a strong easterly component ($\phi \in [130°, 134°]$). Similarly, SCADA data are only statistically different from the 3D PBL simulations ($\Delta x = 1$ km) for wind sectors $\phi \in [130°, 134°]$ and $\phi = 161° \pm 1°$. Surprisingly, an increased grid resolution while using the 3D PBL (i.e., $\Delta x = 0.5$ km) negatively impacts the ability of the mesoscale model to represent cluster-wake effects on front-row turbines, displaying the least skill in reproducing observations. It is likely that the horizontal gradients of the mean velocities become increasingly important for the wake evolution with the finer grid spacing. Thus, the "full" 3D PBL model instead of its "boundary-layer approximation" may be better suited for modeling the wake evolution downstream of a wind farm using the smaller grid spacing. Despite some studies suggesting turbine-added TKE may affect wind farm wake evolution [25, 23, 8], our data show that power losses due to cluster-wake effects are minimally impacted by α, similar to previous results [28]. Nonetheless, neglecting the turbine-added TKE (i.e., $\alpha = 0$) yields the largest differences between the mesoscale model predictions with MYNN and the SCADA data.

Mesoscale simulations can represent differences in cluster-wake effects caused by different atmospheric stability regimes (Figure 5). For the SCADA data, we quantify stability using the bulk Richardson number between the surface and 150 m derived from ERA5 reanalysis. For WRF, stable conditions are defined using the surface heat flux. For the wind conditions described in Section 4, about 60% (67%) of the cases in WRF (SCADA) are stable and 40% (32%) are unstable. All simulations display increased power losses during stable conditions compared to unstable conditions, just like the SCADA data. The 3D PBL ($\Delta x = 1$ km) better captures cluster-wake effects on front-row turbines for stable and unstable conditions than the other model configurations. Conversely, the 3D PBL ($\Delta x = 0.5$ km) evidences the least agreement with SCADA data for both stable and unstable conditions. Mean cluster-wake effects are similar between the stable and unstable simulations for winds with a strong southerly component ($\phi \sim 165°$). Winds from the south have a long fetch over land, where atmospheric stability can be different (and in many cases opposite) from offshore, and so an internal boundary layer develops with stably stratified winds aloft a weakly unstable surface layer that can persist

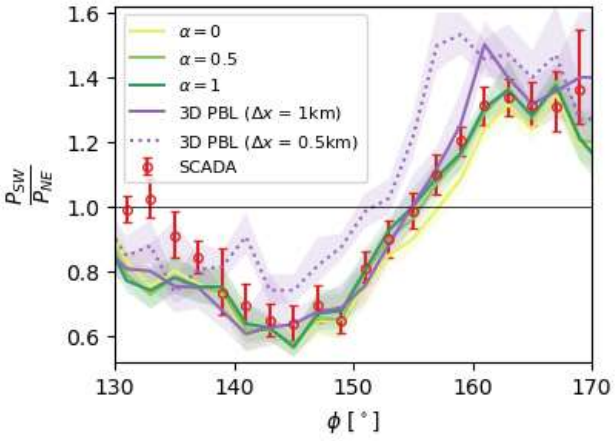

Figure 4. Ratio of power production between the southwest (SW) and northeast (NE) front-row turbines (as shown in Figure 1) of Westermost Rough for simulations and observations. Data are shown for wind speeds between $[6\ \mathrm{m\ s^{-1}}, 9.5\ \mathrm{m\ s^{-1}}]$ and wind directions between $[130°, 170°]$ in $2°$ bins. The shaded area/error bars represent the 95% confidence interval obtained from a bootstrapping method.

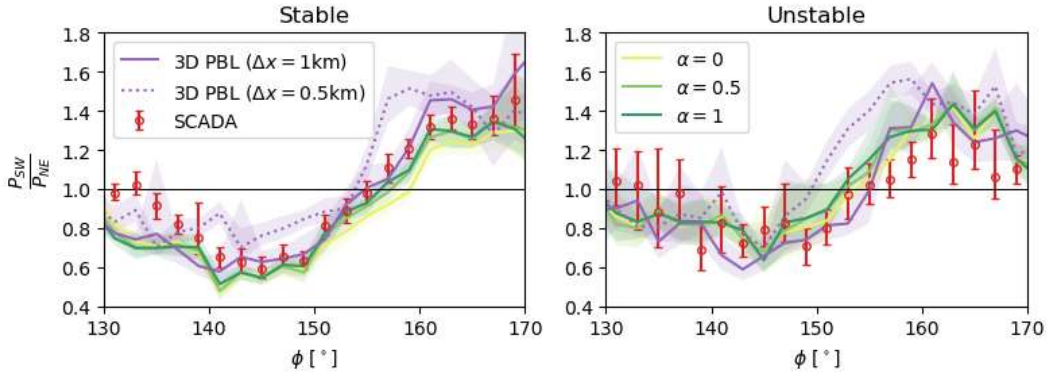

Figure 5. Same as Figure 4 but for stable (left) and unstable (right) atmospheric stability conditions.

for long distances and affect cluster-wake evolution.

5.2. Wind farm

Even though mesoscale simulations accurately represent cluster-wake effects on front-row turbines (Section 5.1), they do not necessarily capture the effect on the entire downstream wind farm. We quantify the model's accuracy in representing the effect from internal and external wakes using the error metric $\mathbb{E}$ defined in Eq. 2, where $\hat{P}_o$ and $\hat{P}_m$ are the average normalized power production of each turbine from SCADA and WRF, respectively, for the wind speed U_i and direction ϕ_j sectors. The normalized power production of each turbine in Westermost Rough for a combination of wind speed and direction (U_i, ϕ_j) is estimated as $\hat{P} = P/P_{FR}$, where P_{FR} is the average power production of the front-row turbines. $\mathbb{E}$ provides a measure of the mismatch between WRF and SCADA for a set of inflow wind conditions. Based on Eq. 2, WRF overestimates wake effects when $\mathbb{E} > 0$, and underestimates wake effects when $\mathbb{E} < 0$. Figure 6 illustrates the mismatch between WRF and SCADA for two sets of wind directions: when the wind turbine columns are aligned with the incoming flow (Figure 6a-c), and when they are staggered (Figure 6d-f). Note that we do not include results from MYNN for $\alpha = 0, 0.5$ in Figure 6 because they are nearly identical to the results from MYNN with $\alpha = 1$.

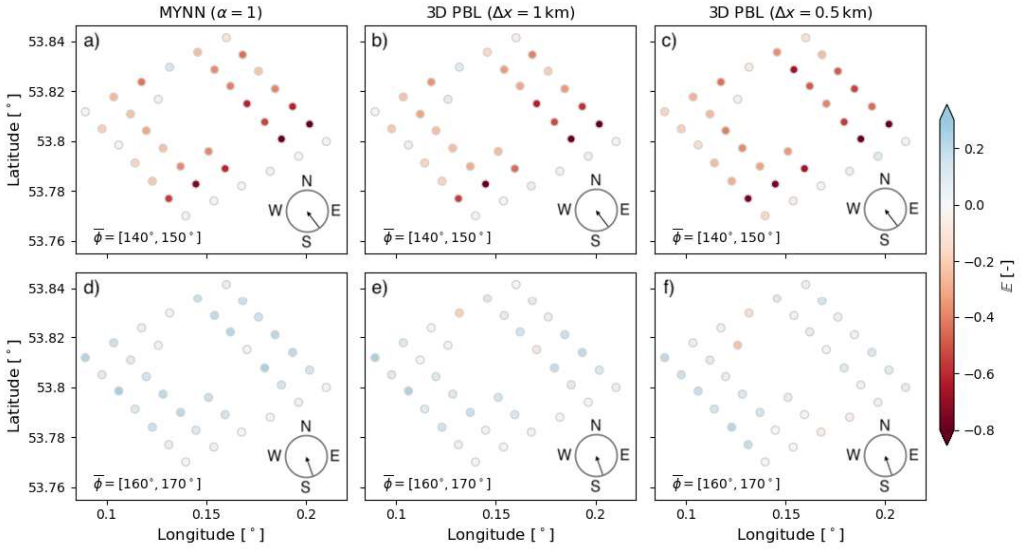

Figure 6. Normalized difference between measured and simulated power production for each wind turbine in Westermost Rough. Data are shown for wind speeds between [6 m s^{-1}, 9.5 m s^{-1}]. The top panels (a-c) correspond to wind directions within $[140°, 150°]$, and the bottom panels (d-f) to wind directions within $[160°, 170°]$. Panels (a,d) show the difference between SCADA and WRF with MYNN ($\alpha = 1$), panels (b,e) the difference between SCADA and WRF with the 3D PBL ($\Delta x = 1$ km), and panels (c,f) the difference between SCADA and WRF with the 3D PBL ($\Delta x = 0.5$ km). The arrows in the bottom right of each panel illustrate the range of wind directions considered.

$$\mathbb{E}(U_i, \phi_j) = \frac{\hat{P}_o(U_i, \phi_j) - \hat{P}_m(U_i, \phi_j)}{\hat{P}_o(U_i, \phi_j)} \tag{2}$$

Mesoscale simulations underestimate (overestimate) internal-wake effects when the wind direction results in an aligned (staggered) array layout within Westermost Rough (Figure 6). All model configurations display the same trend when compared to the observations. Power production from WRF is generally larger than SCADA for aligned conditions (Figure 6a-c), and consistently larger for the second turbine row in Westermost Rough, suggesting WRF predicts smaller velocity deficits than the observations. Conversely, the simulations predict larger internal-wake velocity deficits when the wind direction results in a staggered layout, as depicted by reduced power production compared to SCADA (Figure 6d-f). Differences between SCADA and WRF are minimal for front-row turbines, as shown in Section 5.1, suggesting cluster wakes from Humber Gateway are accurately represented in the simulations.

Internal-wake effects are not accurately captured in the mesoscale simulations because the velocity deficits are distributed over a grid cell that is much larger than the individual wakes. As a result, the velocity deficit is reduced for aligned conditions ($\phi \approx 146°$), minimizing internal-wake effects on downstream turbines. For the same reasons, power reductions from internal wakes are overestimated in a staggered layout ($\phi \approx 165°$) because individual turbine wakes affect a wider downstream area. Furthermore, turbines may occupy adjacent grid cells in the staggered layout; thus, individual-turbine wakes can propagate to a nearby turbine even if it is not immediately downstream. Given that internal-wake effects are not accurately captured in mesoscale simulations, it can be argued that total wake-related power losses that includes both internal- and cluster-wake effects can be misrepresented.

6. Summary and Conclusions

Wakes from offshore wind turbine clusters can propagate long distances, reducing the power production of downstream wind farms. Power losses from cluster wakes have historically been underestimated, leading to uncertainty in energy yield estimates. Mesoscale numerical weather prediction models can be used to estimate losses from cluster wakes and reduce uncertainty in wind farms' energy production assessments. However, there is still uncertainty regarding the accuracy and calibration parameters of the wind turbine parameterizations within them. Here, we investigate the ability of the mesoscale Fitch wind turbine parameterization to represent offshore cluster wakes using two boundary-layer parameterizations. We perform high-resolution mesoscale simulations of two offshore wind farms in the North Sea using the Weather Research and Forecasting model. Wind turbine operational data from the downstream wind farm are used to investigate the ability of the mesoscale model to capture internal- and external-wake effects.

Mesoscale models accurately represent cluster-wake effects on the front-row turbines of the downstream wind farm, but fail to capture the internal-wake effects. The one-dimensional and three-dimensional boundary-layer parameterizations yield accurate estimates for cluster-wake-induced power losses on the front-row turbines of a waked offshore wind farm (Figure 4). Inherently, stable atmospheric conditions exhibit increased power losses compared to unstable atmospheric stability regimes (Figure 5), a feature that is well-captured by the mesoscale simulations. However, mesoscale models fail to capture the cumulative power reductions for an entire wind farm when it is being waked by an upstream turbine cluster because internal wakes are not well represented. Due to the numerical grid resolution used in the mesoscale simulations, power losses due to internal wakes are overestimated (underestimated) when the wind is staggered (aligned) with the turbine columns of the wind farm (Figure 6). It is likely that an even finer grid spacing is required to accurately represent internal-wake effects in mesoscale simulations. However, the horizontal gradients in the wake of the wind farm may become non-negligible with the smaller grid spacing, highlighting the importance of further development of the "full" 3D PBL for high-resolution mesoscale modeling of wind farms. Future studies could use a hybrid approach and combine engineering models or large-eddy simulations with mesoscale models to evaluate internal-wake effects on power production of the offshore wind farm. Mesoscale models may also be used to estimate cluster-wake effects when observations are not available or for planning purposes. To this end, mesoscale model results may be employed to tune engineering wake models for farm-to-farm wakes for a variety of wind speeds, wind directions, and atmospheric stability conditions that represent the climatology of a given site, which is cost-prohibitive if only using large-eddy simulations.

7. Acknowledgments

The authors would like to thank Ørsted for providing access to operational and measurement data from the Westernmost Rough offshore wind farm. This work was authored in part by the National Renewable Energy Laboratory, operated by Alliance for Sustainable Energy, LLC, for the U.S. Department of Energy (DOE) under Contract No. DE-AC36-08GO28308. Partial funding was provided by DOE's Office of Energy Efficiency and Renewable Energy Wind Energy Technologies Office and funded in part by the Bureau of Ocean Energy Management through an interagency agreement with DOE. Partial funding was also provided by partially funded by the National Offshore Wind Research and Development Consortium (NOWRDC) to carry out a Joint Industry Project investigating Multi-fidelity Modeling of Offshore Wind Inter-array Wake Impacts to Inform Future U.S. Atlantic Offshore Wind Energy Area Development under CRD-23-24539-0. The US government retains certain rights in intellectual property under CRD-23-24539-0. This publication does not necessarily reflect the views of NOWRDC or the US government, and NOWRDC nor the US government makes no representations or

warranties and has no liability for any of its contents. Timothy W. Juliano was supported by the U.S. Department of Energy Wind Technology Office Contract #DE-A05-76RL01830 to Pacific Northwest National Laboratory (PNNL). The National Center for Atmospheric Research (NCAR) is a subcontractor to PNNL under Contract #659135. NCAR is a major facility sponsored by the National Science Foundation under Cooperative Agreement No. 1852977. The research was performed using computational resources sponsored by DOE and located at the National Renewable Energy Laboratory.

References

[1] Platis A, Siedersleben S K, Bange J, Lampert A, Bärfuss K, Hankers R, Cañadillas B, Foreman R, Schulz-Stellenfleth J, Djath B, Neumann T and Emeis S 2018 *Sci Rep* **8** 2163 ISSN 2045-2322
[2] Schneemann J, Rott A, Dörenkämper M, Steinfeld G and Kühn M 2020 *Wind Energ. Sci.* **5** 29–49 ISSN 2366-7451
[3] Lee J C Y and Fields M J 2021 *Wind Energ. Sci.* **6** 311–365 ISSN 2366-7451
[4] Stieren A and Stevens R J 2022 *Flow* **2** E21 ISSN 2633-4259
[5] Doekemeijer B M, Simley E and Fleming P 2022 *Energies* **15** 1964 ISSN 1996-1073
[6] Maas O 2023 *Wind Energ. Sci.* **8** 535–556 ISSN 2366-7451
[7] Eriksson O, Baltscheffsky M, Breton S P, Söderberg S and Ivanell S 2017 *J. Phys.: Conf. Ser.* **854** 012012 ISSN 1742-6588, 1742-6596
[8] Ali K, Schultz D M, Revell A, Stallard T and Ouro P 2023 *Monthly Weather Review* **151** 2333–2359 ISSN 0027-0644, 1520-0493
[9] Fischereit J, Schaldemose Hansen K, Larsén X G, Van Der Laan M P, Réthoré P E and Murcia Leon J P 2022 *Wind Energ. Sci.* **7** 1069–1091 ISSN 2366-7451
[10] Peña A, Mirocha J D and Van Der Laan M P 2022 *Monthly Weather Review* **150** 3051–3064 ISSN 0027-0644, 1520-0493
[11] Wyngaard J C 2004 *Journal of the Atmospheric Sciences* **61** 1816–1826 ISSN 0022-4928, 1520-0469
[12] Rai R K, Berg L K, Kosović B, Haupt S E, Mirocha J D, Ennis B L and Draxl C 2019 *Monthly Weather Review* **147** 1007–1027 ISSN 0027-0644, 1520-0493
[13] Juliano T W, Kosović B, Jiménez P A, Eghdami M, Haupt S E and Martilli A 2022 *Monthly Weather Review* **150** 1585–1619 ISSN 0027-0644, 1520-0493
[14] Fitch A C, Olson J B, Lundquist J K, Dudhia J, Gupta A K, Michalakes J and Barstad I 2012 *Monthly Weather Review* **140** 3017–3038 ISSN 0027-0644, 1520-0493
[15] Volker P J H, Badger J, Hahmann A N and Ott S 2015 *Geosci. Model Dev.* **8** 3715–3731 ISSN 1991-9603
[16] Keith D W, DeCarolis J F, Denkenberger D C, Lenschow D H, Malyshev S L, Pacala S and Rasch P J 2004 *Proc. Natl. Acad. Sci. U.S.A.* **101** 16115–16120 ISSN 0027-8424, 1091-6490
[17] Fitch A C, Olson J B and Lundquist J K 2013 *Journal of Climate* **26** 6439–6458 ISSN 0894-8755, 1520-0442
[18] Nakanishi M and Niino H 2009 *Journal of the Meteorological Society of Japan* **87** 895–912 ISSN 0026-1165, 2186-9057
[19] Kosović B, Jimenez Munoz P, Juliano T W, Martilli A, Eghdami M, Barros A P and Haupt S E 2020 *J. Phys.: Conf. Ser.* **1452** 012080 ISSN 1742-6588, 1742-6596
[20] NREL 2022 Flasc. version 1.0 URL `https://github.com/NREL/flasc`
[21] Hersbach H, Bell B, Berrisford P, Biavati G, Horányi A, Muñoz Sabater J, Nicolas J, Peubey C, Radu R, Rozum I, Schepers D, Simmons A, Soci C, Dee D and Thépaut J N 2023 ERA5 hourly data on pressure levels from 1940 to present
[22] Mellor G L and Yamada T 1982 *Reviews of Geophysics* **20** 851–875 ISSN 8755-1209, 1944-9208
[23] Rybchuk A, Juliano T W, Lundquist J K, Rosencrans D, Bodini N and Optis M 2022 *Wind Energ. Sci.* **7** 2085–2098 ISSN 2366-7451
[24] Arthur R S, Juliano T W, Adler B, Krishnamurthy R, Lundquist J K, Kosović B and Jiménez P A 2022 *Journal of Applied Meteorology and Climatology* **61** 685–707 ISSN 1558-8424, 1558-8432
[25] Archer C L, Wu S, Ma Y and Jiménez P A 2020 *Monthly Weather Review* **148** 4823–4835 ISSN 0027-0644, 1520-0493
[26] Nygaard N G, Steen S T, Poulsen L and Pedersen J G 2020 *J. Phys.: Conf. Ser.* **1618** 062072 ISSN 1742-6588, 1742-6596
[27] Perkins S E, Pitman A J, Holbrook N J and McAneney J 2007 *Journal of Climate* **20** 4356–4376 ISSN 1520-0442, 0894-8755
[28] Rosencrans D, Lundquist J K, Optis M, Rybchuk A, Bodini N and Rossol M 2024 *Wind Energ. Sci.* **9** 555–583 ISSN 2366-7443

Estimating Long-Range External Wake Losses in Energy Yield and Operational Performance Assessments Using the WRF Wind Farm Parameterization

Mark Stoelinga, Ph.D.
Miguel Sanchez-Gomez, MS[1]
Gregory S. Poulos, Ph.D.
Jerry Crescenti, M.S.

ArcVera Renewables
1301 Arapahoe Street, Suite 105
Golden, Colorado 80401 USA

[1] Miguel Sanchez-Gomez is a graduate student at the University of Colorado who worked for ArcVera Renewables.

DOCUMENT HISTORY

Preparer(s): Mark Stoelinga, Lead, Atmospheric Science Innovation and Applications

Reviewer(s): Jerry Crescenti, Director, Wind Energy Analysis Team, Technical Editor, Emily Coulter

Final Review and Approval by: Greg Poulos, CEO, Principal Atmospheric Scientist

Version	Date	Comments
1.0	08/09/2022	Initial issue

Disclaimer

Report:
Document 1.0

Report Standard:
Research Result

Classification:
Confidential

Status:
Final

Key to Report Standard

Research Result: Description of the subject of the report, including methods and conclusions with review from senior-level staff

Review: A brief description without details for general use.

Key to Classification

Strictly Confidential: For recipients only

Confidential: Can be distributed within client's organization

Internal: Not to be distributed outside ArcVera Renewables

Client's Discretion: Distribution at the client's discretion

Published: No restriction

ABSTRACT

ArcVera Renewables carried out a study of long-range (> 50 rotor diameters) external wakes, with emphasis on the tendency of existing engineering wake models to greatly underpredict the strength and longevity of external wind farm wake losses on other projects under some atmospheric conditions. Three wind farm case studies are presented; two onshore in the central United States, and one offshore in the New York Bight lease areas recently auctioned for wind energy development. The first case study demonstrates the inadequacy of standard engineering wake models to capture the magnitude of long-range external wake losses. With that result as motivation, the second case study was used to demonstrate the utility of the WRF mesoscale model with the Wind Farm Parameterization (WFP) to model the wake impacts of distant external turbines more accurately than existing engineering wake models. WRF-WFP produced average external wake losses much closer to, 16% higher than, that derived from SCADA data. In contrast, two engineering wake loss models failed to come close to the actual wake loss deficit; these models under-predicted external wake losses as a small fraction, ⅓ or less, of that derived from SCADA data.

As a further demonstration of the capabilities of WRF-WFP, and to give a view into the potential for large project-to-project wake impacts in the recently auctioned New York Bight offshore lease areas, ArcVera presented a third offshore wind energy case study. ArcVera Renewables designed WRF-WFP simulations of hypothetical wind project turbine arrays that might be built in those areas approximately 5-10 years from today. The simulations were run for a set of 16 days, with winds from the prevailing southwesterly wind direction, selected to maximize the waking of arrays aligned in a southwest to northeast direction. The simulations produced dramatic hub-height project-scale wake swaths that extended over 50 km downwind, with a specific example showing a waked wind speed deficit of 7% extending 100 km downwind from the array of turbines that produced it. When averaged over the selected 16 simulation days, the energy loss at the target lease area due to external wakes from arrays to its southwest was 28.9%. While the 16-day result undoubtedly greatly exceeds the long-term external wake loss for winds from all directions, it is nonetheless illustrative of the potential for much greater external wake losses than have been accounted for in development planning for the New York Bight lease areas; and, as in the two onshore long-distance wake loss case studies, are much larger than engineering wake models predict for the same conditions.

The implications of this study of long-range wakes on the assessment of energy production (or shortfalls thereof) of existing and anticipated future wind farms is material and significant, as unexpectedly large impacts may well be present, and existing non-WRF-WFP-based engineering long-range wake loss methods are shown to be inadequate. The inadequacy of these models for long-distance wakes may be remedied in the future with further validation time-series modeling and concomitantly accurate assessment of time periods when atmospheric stability is high. Still larger implications are clear for long-term project valuation risk, the analysis and assessment of hybrid projects, battery usage risk, and around-the-clock reliable renewable energy power production. Offshore wind farms are equally strongly affected, and the extensive global plans for proximal deployment of offshore wind projects should account for such impacts.

ArcVera Renewables 1301 Arapahoe Street, Suite 105 | Golden, CO 80401 USA | +1 720.237.2929

TABLE OF CONTENTS

DOCUMENT HISTORY **2**

ABSTRACT **2**

TABLE OF CONTENTS **3**

LIST OF FIGURES **4**

LIST OF TABLES **4**

LIST OF ACRONYMS AND ABBREVIATIONS **5**

INTRODUCTION **6**

CASE STUDY 1: THE PROBLEM **7**

A POTENTIAL SOLUTION: MESOSCALE MODELING WITH A WIND FARM PARAMETERIZATION **8**

CASE STUDY 2: A DEMONSTRATION OF WRF-WFP **9**

CASE STUDY 3: EXTERNAL WAKES FROM HYPOTHETICAL WIND FARMS IN THE NEW YORK BIGHT LEASE AREAS **12**

- CONFIGURATION 12
- RESULTS 13
- SENSITIVITY TESTS 15

CONCLUSIONS **16**

REFERENCES **17**

ArcVera Renewables 1301 Arapahoe Street, Suite 105 | Golden, CO 80401 USA | +1 720.237.2929

LIST OF FIGURES

Figure 1. Schematic of the two projects studied in Case Study 1. 8

Figure 2. Schematic of the two projects studied in Case Study 2. 11

Figure 3. Waked wind speed deficit at hub height from the WRF-WFP, in m/s (color scale at bottom), at 10 pm local time on a mid-summer day at the projects in Case Study 2. 13

Figure 4. Map of New York Bight offshore lease areas (orange outlines). 16

Figure 5. Waked wind speed deficit at hub height (m/s, color scale at bottom), from the WRF-WFP simulations of the New York Bight lease areas, at 1530 EST, 24 Feb 2020. 17

LIST OF TABLES

Table 1. SCADA-derived and modeled long-range annual-average external wake losses at Target Project for Case Study 1. 9

Table 2. SCADA-derived and modeled long-range external wake losses at Target Project for Case 2 for the selected 1300 hours of northerly wind direction, with separate results by stability class. 13

Table 3. Modeled long-range external wake losses at New York Bight Lease Area 0538 for the 16 selected days of primarily southwest wind direction. 18

Table 4. Sensitivity test results. 19

LIST OF ACRONYMS AND ABBREVIATIONS

COD	Commercial Operation Date
D	Rotor Diameter
ECMWF	European Centre for Medium-Range Weather Forecasts
ERA5	ECMWF Reanalysis, Version 5
EST	Eastern Standard Time
EV-DAWM	Eddy-Viscosity / Deep Array Wake Model
IEA	International Energy Agency
LES	Large-Eddy Simulation
MW	megawatt
SAR	Synthetic aperture radar
SCADA	Supervisory Control and Data Acquisition
TKE	Turbulent Kinetic Energy
WFP	Wind Farm Parameterization
WRF	Weather Research and Forecast Model

ArcVera Renewables 1301 Arapahoe Street, Suite 105 | Golden, CO 80401 USA | +1 720.237.2929

1 INTRODUCTION

When wind energy resource assessments are conducted for planned wind energy projects, one of the most significant and uncertain contributors to that estimate is the energy loss due to wind turbine wakes. Typically, the wake losses are calculated separately for those coming from wakes generated within the project (internal wakes) and those generated by turbines outside the project (external wakes). Until recently the same models have been used for both. These models often predict negligible waked wind speed deficits just a few tens of rotor diameters downwind of the waking turbines. Aggregate effects of wakes from a large array of turbines acting in concert can extend this farm-scale wake effect, but, the general sense in the industry was that wakes from external turbines more than roughly 50D ("D" refers to the rotor diameter of the wake-generating turbine) from the project of interest could be ignored. In Brazil, for example, local renewable energy regulations require compensation for lost energy from new wind farms installed within 20 wind turbine tip-heights (~24D).

Historical work in the 1980's (Nierenberg, 1989, Nierenberg and Kline, 1989) documented significant wake effects 250D downwind in California's passes. More recently, observational evidence gathered over the last decade has begun to change this view. For onshore wakes, the "far wake" region was thought to extend no more than about 15D downwind (McCay et al. 2012). Scanning Doppler radar revealed wakes from single turbines extending at least 30D (Hirth et al. 2012). The offshore environment has always been understood to be more conducive than onshore to wake longevity, because turbines tend to be larger (producing larger wakes), atmospheric conditions tend to be more stable (which slows wake recovery), and the wind flow is less disturbed by underlying surface irregularities. Offshore wakes were thought to extend perhaps as far as 15 km (McCay et al. 2012), corresponding to approximately 125D. However, recent evidence from satellite-based synthetic aperture radar (SAR) measurements over the North Sea (Hasagar et al. 2015; Djath et al. 2018); as well as aircraft measurements in the same region (Platis et al. 2018) have shown wind farm-scale wakes with wind speed deficits of 5-10% extending 50 km or more (> 400D).

This white paper brings to light the significant impacts on energy production due to long-range wakes. We present evidence from two pairs of wind farms in the central United States, in which SCADA data from a downwind "target" wind farm is analyzed before and after a new upwind project was built. We also show the insufficiency of existing wake models to capture the energy losses caused by the distant upwind farm. We describe the accuracy potential of the Wind farm Parameterization (WFP), designed and implemented in the Weather Research and Forecast (WRF) model by Fitch et al. (2012), as a commercially viable tool for estimating the impacts of long-range external wakes and external wake production risk. For the second pair of onshore projects, we demonstrate that WRF-WFP predicts external wake losses much closer to the SCADA-derived values than the conventional engineering models.

Finally, as in recent studies focused on the lease areas offshore of Massachusetts (Rosencrans et al. 2022; Pryor et al. 2022), we apply the WRF-WFP to hypothetical future wind development in the New York Bight Lease Areas recently auctioned in February 2022, to demonstrate the

potential for strong, long-range wakes from these lease areas to negatively affect energy production at neighboring wind farms, even those many tens of kilometers away. These hypothetical simulations use the largest reference turbine defined in the IEA Wind reference turbine family, assuming that turbines of this capacity (or larger) will eventually be installed when construction begins in 5-10 years. The results are material to heretofore seldom considered wind energy resource assessment production long-range wake loss risk; in terms of distance downwind (50-100 km) wakes with speed deficits greater than 1 m/s persist and directly impact other lease areas. These predictions are preliminary, considering there is no operational history for these very large turbines with which to validate the long-range wakes they produce within the WRF-WFP. However, confidence in the WRF-WFP has been accumulating based on validation studies already conducted by the research community (see below) and the onshore results presented in the first part of this report. ArcVera already commercially utilizes this tool to assess and reduce risk, and anticipates that tools like the WFP, or other wind farm-aware mesoscale model applications, will become a key part of the wind energy resource assessment (WERA) wind farm-atmosphere interaction (WFAI)/wake loss modeling toolbox.

2 CASE STUDY 1: THE PROBLEM

The challenge of correctly estimating long-range wake impacts can be illustrated with Case Study 1, depicted schematically in Figure 1. Case Study 1 involves a smaller, new project being built 13 km north of an existing larger project in the central United States. Details of the turbine layouts, project capacities, and turbine models are withheld to maintain the projects' anonymity. The existing project is the “target project” at which the impact of external wakes from the new project is evaluated. Four years of SCADA data were available at the target project, with the first two years occurring before the COD of the new project, and the second two years after. While southerlies are the prevailing wind direction, northerlies occupy a secondary frequency peak (see wind rose in Figure 1) and would lead to a project-scale wake impinging upon the target project a substantial portion of the time.

An operational assessment was performed for the target project, using SCADA data from the two separate periods, to determine the long-term energy yield based on the performance of the target project during each period. Reasonable corrections for curtailment, availability, and windiness were made during the period assessed, relative to the long-term, to assure comparability of different periods of record. No other project development occurred within the vicinity during the 4-year study period.

In addition to the operational assessment, wake model experiments were run in which the same project wind climate was applied, but in one experiment, the new project was included, and in the other, it was excluded, and the difference in energy yield at the target project evaluated. This experiment was repeated with two wake models: The Eddy Viscosity / Deep-Array Wake Model (EV-DAWM) available in OpenWind, and the ArcVera Wind Farm-Atmosphere Interaction (WFAI) Model (Poulos et al. 2022). The WFAI model is an empirical loss model built upon and validated against numerous data sets of energy production and measured wind speeds before and after wind farm installations. It was originally developed

under the auspices of U.S. Department of Energy scientific research (DOE 1987, 1990), continually upgraded, and commercially used on numerous WERAs at ArcVera for many years.

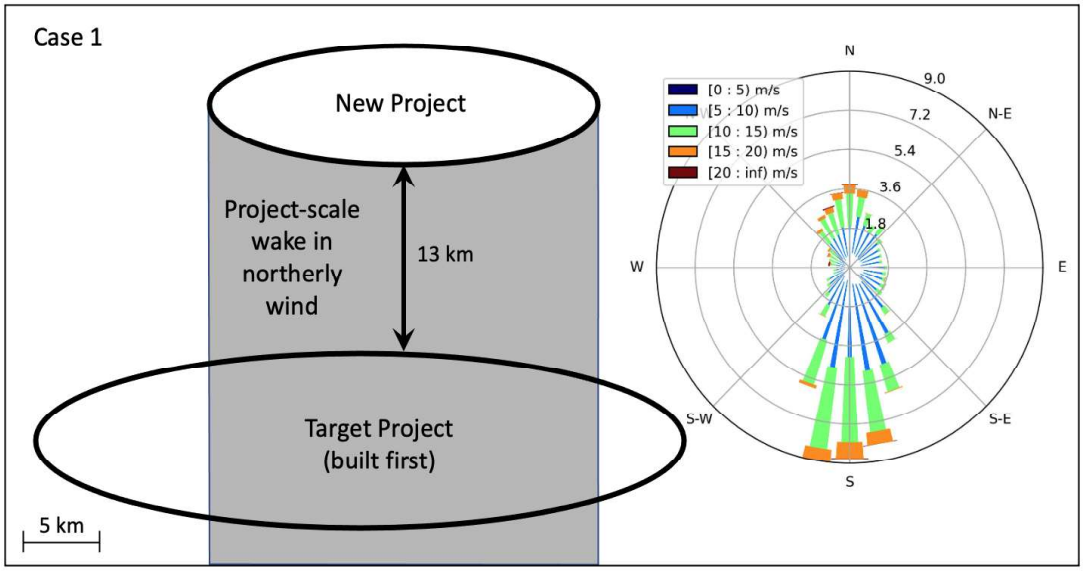

Figure 1. Schematic of the two projects studied in Case Study 1. Ellipses indicate outlines and relative locations of projects. The wind rose is derived from a hub-height met tower within the target project.

Table 1 provides the results of the before and after SCADA-based operational assessment, and the wake model predictions. While the SCADA analysis indicated that the presence of the new wind farm reduced production at the target wind farm by 3.6%, both the wake models indicated a nearly negligible impact of the new wind farm. The wake models were unable to predict even a small fraction of the observed wake loss from an external wind farm 13 km away.

Table 1. SCADA-derived and modeled long-range annual-average external wake losses at Target Project for Case Study 1. Losses are expressed as the percent of gross energy.

Source of Estimate	Long-Range External Wake Loss
SCADA	3.6%
EV-DAWM	0.1%
WFAI Model	< 0.1%

While these engineering wake loss models have been well validated against internal wake and WFAI losses of wind farms based on production data, they have been less well, or unvalidated, at long-range. This long-range wake loss weakness is exposed in this case study.

3 A POTENTIAL SOLUTION: MESOSCALE MODELING WITH A WIND FARM PARAMETERIZATION

The Weather Research and Forecasting model (WRF, Skamarock et al. 2019) is a numerical weather prediction model that has been in use globally by academic and national research institutions, national weather prediction agencies, and private companies with weather and

climate concerns since it was first developed and released in 2000. It is classified as a "mesoscale model," which means it is designed to simulate weather phenomena covering spatial scales from 2 km to 2000 km (numerically resolved with grid spacing of 200 m to 200 km Chapter 10, Pielke, 1984), but has been used successfully at both larger scales and smaller scales, in the latter case as a "large eddy simulation" or LES model, with a grid spacing of 10 m or less). It is used routinely in the wind energy industry for short-term energy forecasting and retrospective energy assessment. ArcVera Renewables has over 45 years combined experience using WRF and similar mesoscale models for various applications, including using WRF and WRF-LES in wind energy forecasting and assessment for over a decade.

In 2012, in response to the increasing interest in wind energy development and the potential physical interactions between wind farms and the weather and climate of the surrounding region, Fitch et al. (2012) developed and implemented in WRF a capability referred to as the Wind Farm Parameterization (WFP), which models the deceleration of winds by turbines within a WRF model grid box, based on the turbine thrust characteristics. The kinetic energy removed by the turbines is distributed between electric power generation and turbulence production. The wind deceleration interacts with the full atmospheric dynamics simulated by WRF, allowing for downwind transport of the waked wind speed deficits, and feedbacks to the flow such as upwind blockage from the simulated combined induction zone effects of wind turbines, flow deflection around wind farms, gravity wave development and impacts on wind flow patterns,, and the complex movement and distortion of wake swaths within time-dependent curved or sheared wind flows. Importantly, the roles of time-varying atmospheric stability, particularly stable atmospheric conditions, and turbulence on wake recovery are realistically represented in meteorological physics within WRF with WFP.

The waked wind speed deficits simulated by WRF-WFP have been validated in several research studies, mostly at North Sea offshore wind projects, including Fitch et al. (2012), Hasagar et al. (2015), Platis et al. (2018), and Siedersleben et al. (2018). In addition, many studies have conducted sensitivity and other tests with WFP, leading to improvements and recommendations for best use (Lee and Lundquist 2017; Archer et al. 2020; Siedersleben et al. 2020; Tomaszewski and Lundquist 2020; and Larsén and Fischereit 2020). Based on these studies, the WFP has been modified and improved and continues to be actively developed in the research community. Therefore, the WFP should be considered a well-validated tool that continues to improve as part of ongoing active research and development. ArcVera's work and the research cited above provides ample validating evidence that WRF-WFP captures the fundamental physics of wind turbine interactions with the atmosphere.

4 CASE STUDY 2: A DEMONSTRATION OF WRF-WFP

Case Study 2 is similar to Case Study 1, in that it involves an existing project, and a new project built to its north (Figure 2). Two key differences from Case Study 1 are that the new project is much larger than the target project; and that the new project is closer to the target project (only 5 km away, as opposed to 13 km in Case Study 1). The wind rose in Figure 2 indicates that a project-scale wake from the new project would impinge on the target project a substantial portion of the time. In Case Study 2, rather than performing a long-term-adjusted operational

assessment for the before and after periods, we evaluated 10-minute SCADA energy production data from the Target Project and ran model simulations only during a selection of days in which maximum waking of the target project by the new project was expected. Maximum waking was expected in northerly flow conditions, with wind speeds in the steep, non-linear section of the target project's power curve. Care was taken to select a set of times in which the wind speed distributions in the before and after period matched, so as not to skew the result due to different wind climates. A total of 1300 hours (~54 days) of SCADA production and simulated winds were used.

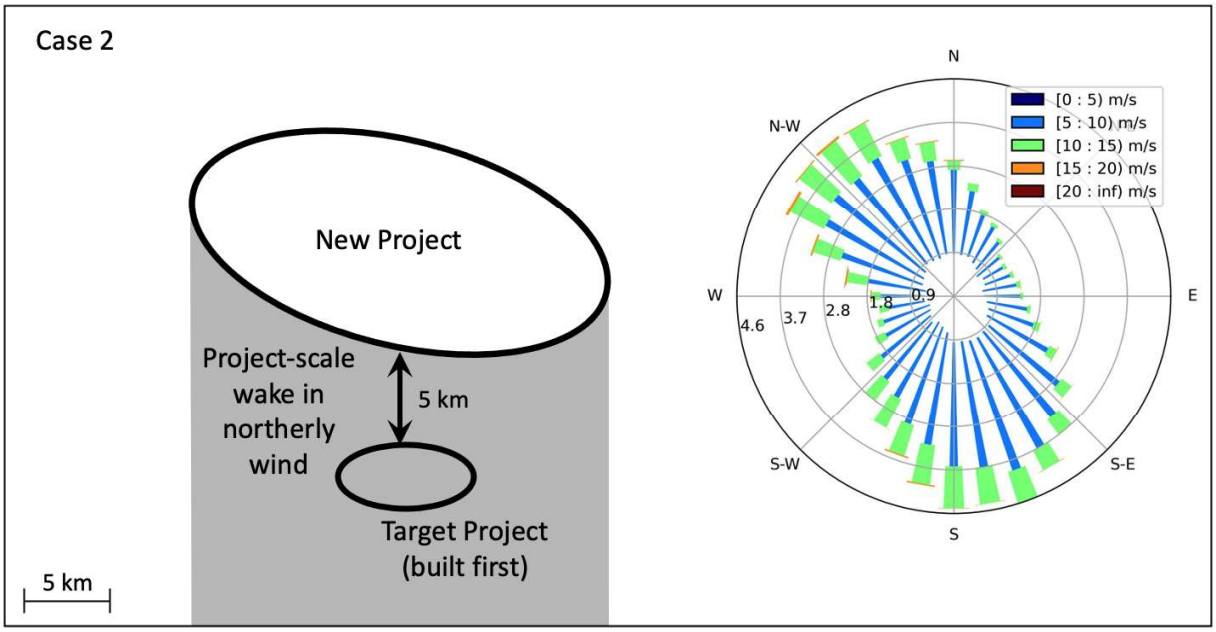

Figure 2. Schematic of the two projects studied in Case Study 2. Ellipses indicate approximate outlines and relative locations of projects. The wind rose is derived from an ERA5 Reanalysis node within the target project.

For Case Study 2, wake model simulations were also performed for the "before" and "after" periods (i.e., with and without wakes from the New Project), using both EV-DAWM and ArcVera WFAI. In addition, WRF-WFP was run for the same selected set of times, with three simulations performed for each of the selected dates, one with no turbines, one with only the target project turbines, and one with new project and target project turbines. We used WRF version 4.2.1, which includes a key code correction for the WFP identified by Archer et al. (2020).

The study used WRF model grid with 1.0-km spacing and obtained initial and boundary conditions from the ERA5 Reanalysis data set (Hersbach et al. 2020). Waked wind speed deficits due to the new project were evaluated from the difference between the "new and target turbines" run and the "only target turbines" run. For illustration, an example of waked wind speed deficit simulated by WRF-WFP at one time is shown in Figure 3. It depicts all wakes from both projects by showing the difference between the "new and target turbines" run and the "no turbines" run during a time of north-northeasterly wind flow. Note that the project-scale wake swath from the new project not only envelopes the smaller target project but continues with

substantial magnitude (at least 1 m/s) to the domain boundary over 30 km south-southwest of the new project.

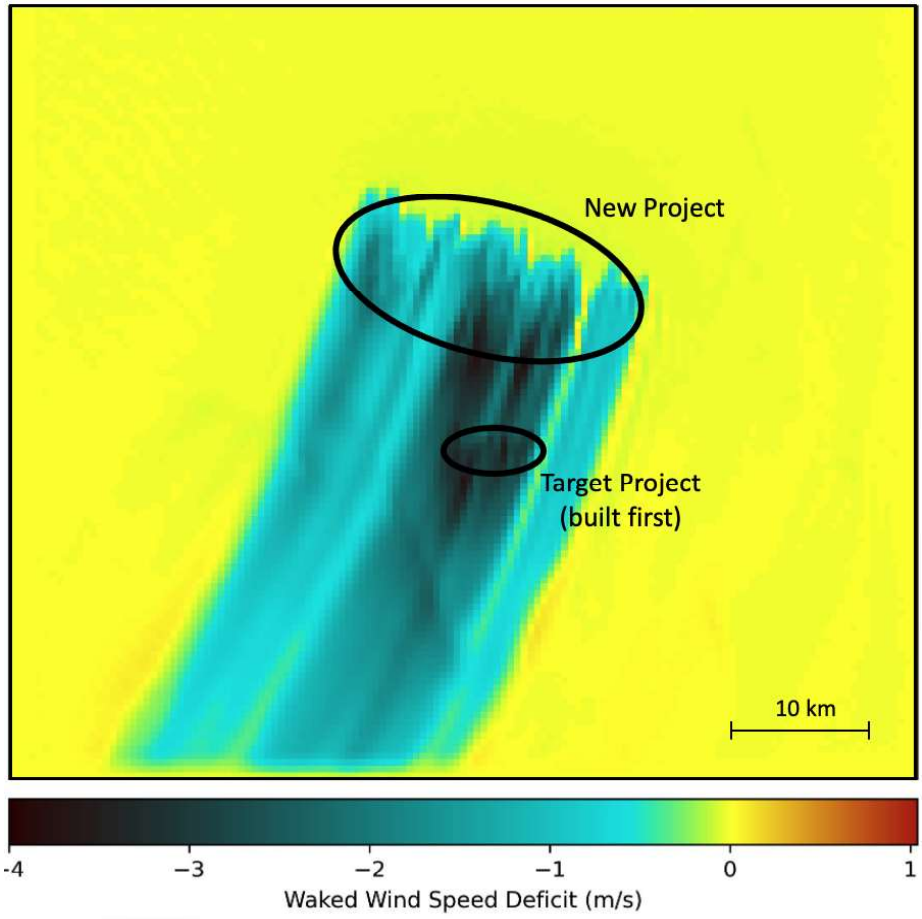

Figure 3. Waked wind speed deficit at hub height from the WRF-WFP, in m/s (color scale at bottom), at 10 pm local time on a mid-summer day at the projects in Case Study 2. Ellipses indicate approximate outlines and relative locations of projects. Hub height wind speed at this time was 9.5 m/s.

The average wake loss during the selected periods is shown in Table 2. Because the times were selected to maximize the wake impacts of the new project on the target project, the loss numbers are much higher than the long-term mean values shown for Case Study 1. Additionally, the time points were segregated into unstable and stable categories based on negative or positive values of the bulk Richardson number. The SCADA analysis indicates a large external wake impact of 23.8% by the new project on the target project, averaged over the selected time points. As expected, the SCADA analysis also shows wake impacts to be stronger during stable periods than during unstable periods. The WRF-WFP model overpredicts the external wake loss during the selected time points, but only by a factor of 1.16 (16% overprediction). It also correctly identifies the stronger wake impact during stable conditions. Meanwhile, as in Case Study 1, the engineering wake loss models underpredict the effect by a large amount; they predict only a small fraction of the SCADA-derived wake loss in energy.

Table 2. SCADA-derived and modeled long-range external wake losses at Target Project for Case 2 for the selected 1300 hours of northerly wind direction, with separate results by stability class. Losses are expressed as the percent of gross energy. Percent frequency of occurrence of stable and unstable conditions are shown in column headings.

	Long-Range External Wake Loss		
Source of Estimate	All Times	Stable Conditions (67.5%)	Unstable Conditions (32.5%)
SCADA	23.8%	29.1%	12.8%
EV-DAWM	5.7%	not tested	not tested
ArcVera WFAI Model	0.2%	not tested	not tested
WRF-WFP	27.7%	32.6%	17.5%

5 CASE STUDY 3: EXTERNAL WAKES FROM HYPOTHETICAL WIND FARMS IN THE NEW YORK BIGHT LEASE AREAS

5.1 CONFIGURATION

As a further demonstration of the capabilities of WRF-WFP, and to give a view into the potential for large project-to-project wake impacts in the recently auctioned New York Bight offshore lease areas, ArcVera Renewables ran WRF-WFP simulations of hypothetical wind projects that might be built in those areas perhaps 5-10 years from today. The hypothetical arrays, depicted in Figure 4, were designed as follows. The turbine is the IEA Wind 15-MW Reference Turbine, with a hub height of 150 m and a rotor diameter of 240 m. Turbines of this size and capacity are now starting to be commercially marketed. In 5-10 years, offshore wind energy projects may utilize turbines of this size or larger. We designed the arrays with a turbine spacing of 1.0 nautical miles (1.85 km) in the east-west direction, and 0.75 nautical miles (1.39 km) in the north-south direction, based on our current understanding of what the relevant jurisdictional agencies will require and the measured wind rose. 10 km (42D) gaps were enforced between turbine arrays; there are 3 km gaps between lease areas. Prevailing winds are southwesterly.

Three arrays were designed:

- Northern Array
  - Lease Area 0538
  - 85 turbines
  - Treated as the target project
- Central Array
  - Lease Area 0539
  - 118 turbines
  - Treated as an external project
- Southern Array
  - Lease Areas 0541 and 0542
  - 157 turbines
  - Treated as an external project

The WRF model was configured similarly to Case Study 2, except with slightly finer horizontal grid resolution (800 m). 16 case study dates were selectively chosen to provide maximum time with winds from the 190°-240° sector and speed in the range of 6-11 m/s. Under these conditions, the waking of the target array (0538) by areas 0539, 0541, and 0542 is maximum, not only because they are directionally aligned with the wind, but because in southwesterly flow (the prevailing direction, especially in the warm season), typically there is warm air moving over colder water, resulting in stabilization of the flow and longer-lived wakes. The wind speed range, positioned in the steepest part of the turbine power curve, was chosen to maximize the energy sensitivity to the waked wind speed deficits. The annual wind rose at floating lidar E06 (Figure 4, right side) indicates that the conditions described above frequently occur, though the chosen set of times have much higher wake losses than a long-term mean that accounts for the entire wind rose. For each simulation day, the model was run for 24 h starting at 7:00 AM EST, with a 6-h spin-up period from 1:00 AM to 7:00 AM EST. Model output was produced every 10 minutes.

For each chosen day, three simulations were run, which included the effects of:

1. No turbines (Simulation 1)
2. Turbines at the Southern (0541/0542) Array only (Simulation 2)
3. Turbines at both the Central (0539) and Southern Arrays (Simulation 3)

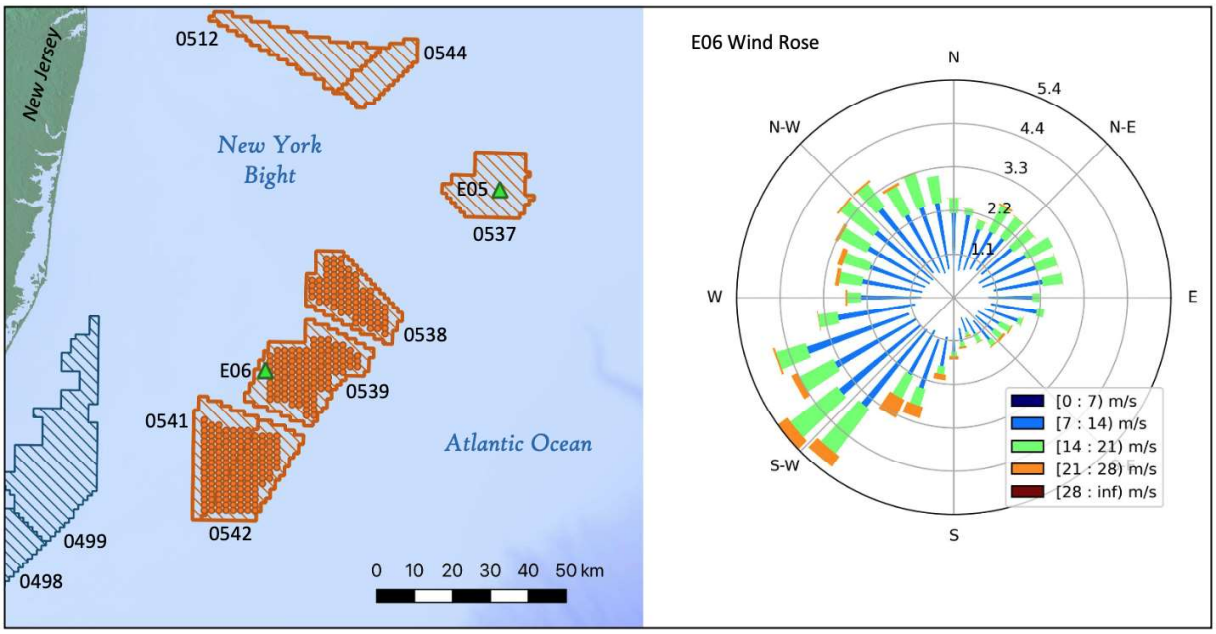

Figure 4. Map of New York Bight offshore lease areas (orange outlines). New Jersey lease areas are also shown (blue outlines). Orange dots indicate hypothetical turbine arrays in lease areas 0538, 0539, 0541, and 0542. Green triangles indicate floating lidar sites E05 and E06. The wind rose in the right panel is from lidar measurements at site E06.

Wind speed deficits on the Northern Array (Lease Area 0538) due to external wakes from the Southern Array only were evaluated from Simulation 2 minus Simulation 1. Wind speed deficits

due to external wakes from the Central and Southern Arrays only were evaluated from Simulation 3 minus Simulation 1.

5.2 RESULTS

An example of waked wind speed deficit from the WRF-WFP simulations is shown in Figure 5. The left panel shows the effect of turbines in only the Southern Array, whereas the right panel shows the effect of turbines in both the Southern and Central Arrays. The dominant feature of these plots is the long-range project-scale wake swath extending from the arrays to the north-northeast. Even at the northern edge of the domain, over 100 km downwind of the Southern Array, the long-range wake from the Southern Array only (left panel) maintains a 0.7 m/s (or 7%) hub-height wind speed deficit; and 80 km downwind of the Central Array, the long-range wake from the Southern and Central Arrays combined (right panel) maintains a 1.0 m/s (or 10%) wind speed deficit. The waked speed deficits within the target (0538, Northern) array are 1.6 m/s (16%) from the Southern Array only, and 2.5 m/s (25%) from the combination of the Southern and Central Arrays. Note that no turbines from the Northern Array were included in the simulations, so the entire speed deficit within the Northern array is due to external wakes from the Southern and Central Arrays.

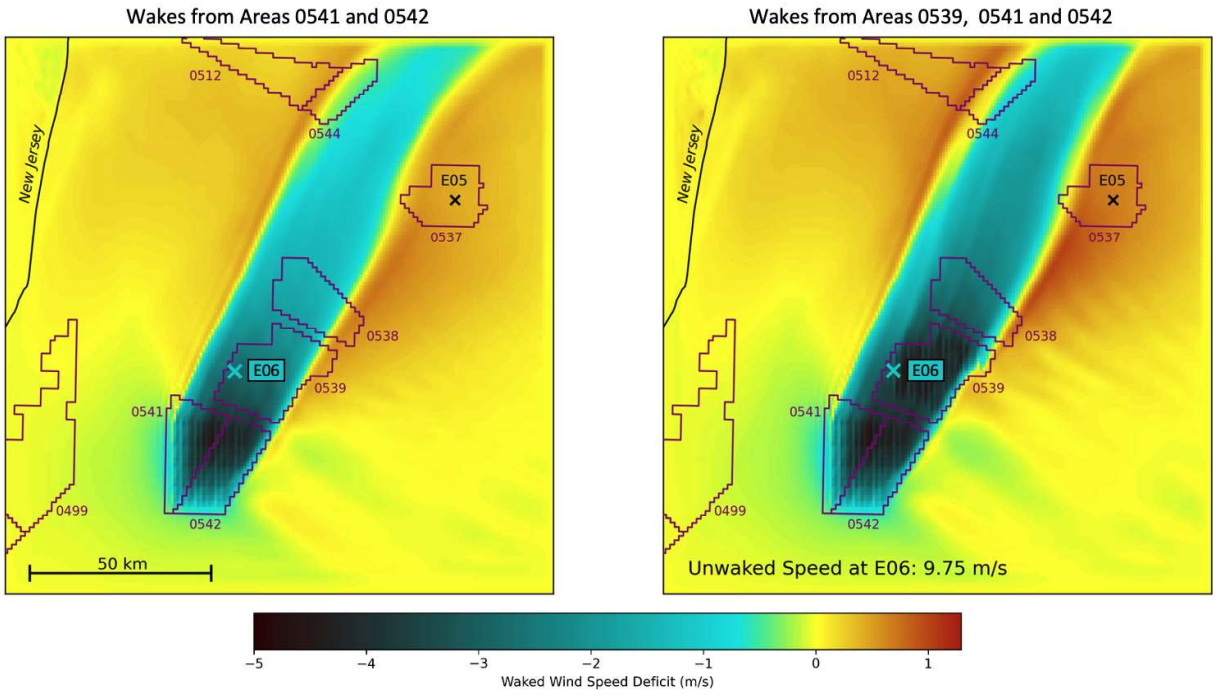

Figure 5. Waked wind speed deficit at hub height (m/s, color scale at bottom), from the WRF-WFP simulations of the New York Bight lease areas, at 1530 EST, 24 Feb 2020. "x" symbols indicate the locations of floating lidars.

In addition to the project-scale wake, other prominent WFAI features emerge in these plots. A region of speed deficit upwind of the projects indicates project-scale blockage, up to 0.5 m/s in some locations, with wave-like structures embedded in it. Downwind, the wake swath is flanked by areas of significant speed enhancement (> 0.5 m/s), which are a subject of future

scientific study. Over the long term, when these flanking wind acceleration zones pass over downwind projects, the accelerations partially offset the wake losses incurred at other times, reducing the long-term mean external wake loss.

Energy-based losses at the Northern Array due to external wakes at the Central and Southern Arrays for the 16 days of the simulation were calculated, along with corresponding predictions from the EV-DAWM and ArcVera WFAI models. Results are shown in Table 3. No validation of the results is possible due to the hypothetical nature of the turbine arrays. However, the results illustrate the potential for large external wake losses. Even if the long-term mean external wake loss at the Northern Array is, for example, one-quarter of the loss from this set of 16-days with enhanced waking conditions, that still represents a very large loss due only to external wakes. But equally important is the result, consistent with those of the first two case studies, that the engineering wake models estimate only a small fraction of the external wake loss predicted by the WRF-WFP.

Table 3. Modeled long-range external wake losses at New York Bight Lease Area 0538 for the 16 selected days of primarily southwest wind direction, with separate results for wakes from Lease Area 0539 only, and from the combination of Lease Areas 0539, 0541, and 0542. Losses are expressed as the percent of gross energy.

	Long-Range External Wake Loss at Area 0538	
Source of Estimate	From 0539 only	From 0539, 0541, & 0542
EV-DAWM	0.5%	5.3%
ArcVera WFAI Model	< 0.1%	0.2%
WRF-WFP	13.0%	28.9%

5.3 SENSITIVITY TESTS

Considering the large magnitude and length of wakes predicted by WRF-WFP in the New York Bight lease areas, and lack of validating data for the large hypothetical wind turbines used in the simulations, ArcVera consulted with Professor Julie Lundquist's research group at the University of Colorado to consider the uncertainty in these model predictions of large, long-range wakes. A suggestion that emerged was to test the sensitivity of the wakes to two configurable parameters that recent studies have demonstrated are important for the magnitude of wakes predicted by WRF-WFP: the number of vertical levels beneath the rotor layer, and the amount of turbine-produced turbulence that is injected into the model simulation.

Tomaszewski and Lundquist (2020) found that using more vertical levels reduces mixing and increases wake longevity (though they found the sensitivity modest). We used only 2 vertical levels beneath the rotor, so we tested increasing that to 4 levels.

The turbulent kinetic energy (TKE) factor (a tunable parameter) scales the amount of turbine-induced turbulence injected into the model flow. A value of 0.0 injects no turbine-induced turbulence, whereas a value of 1.0 injects the full amount consistent with the turbine power and thrust curves. The appropriate amount is not a settled matter, with the original Fitch (2012) paper injecting the full amount (but testing sensitivity to half or double the

full amount). Archer et al. (2020) recommended only one-quarter of the full amount be injected to best match large-eddy simulations that they conducted, and Larsén and Fischereit (2021) found that a value of 1.0 validated better than 0.25. Others have argued that none of the turbine-induced turbulence should be injected into the model flow at the scales resolved by the model (Jacobson and Archer 2012; Volker et al. 2015). In our simulations for both Case Studies 2 and 3, we used a TKE factor of 0.0, so we tested higher values, up to 1.0.

Table 4 shows the parameter values tested in the sensitivity experiments, and the resulting relative change in wake strength compared to the control experiment (green highlight, 0.0%), which used the configuration indicated in the upper left cell of the table (zero turbulence injected, and two model vertical levels below the rotor layer). The wake strength was defined as the area-integrated wind speed difference within the wind speed deficit swath north and east of lease area 0539 . This definition yields a higher value if either the wake's magnitude or areal size increases.

Table 4. Sensitivity test results. The control configuration (green highlight) is the upper left cell in the table, with 2 model levels beneath the rotor layer, and a TKE factor of 0.0%. The value in each cell represents the change in wake strength relative to that of the control configuration. All values are positive, meaning that all sensitivity tests produced stronger wakes than in the control configuration.

		Turbine TKE Injection Factor			
		0.00	0.25	0.50	1.00
Number of model levels beneath rotor	2	0.0%	not tested	not tested	8.0%
	4	0.7%	6.6%	7.7%	8.4%

The increase in vertical levels beneath the rotor slightly increased the wake strength, consistent with Tomaszewski and Lundquist (2020). The increase in turbulence also increased the wake strength. The latter result is counterintuitive considering that greater turbulence would be expected to enhance wake recovery, and this does occur within the waking turbine array, but downwind of it the opposite occurs: the wake is enhanced. Fitch et al. (2012) and Rybchuk et al. (2021) found the same counterintuitive result. In summary, the original configuration actually produced the *weakest* wakes of all the configurations tested. A TKE injection factor of 0.0 was found to produce rather accurate results in Case Study 2, and an increase in TKE injection factor could reduce accuracy based on these sensitivity tests.

6 CONCLUSIONS

ArcVera Renewables carried out a study of long-range (> 50 rotor diameters) external wakes, with emphasis on the tendency of existing engineering wake models to greatly underpredict the strength and longevity of external wind farm wake losses on other projects under some atmospheric conditions. Three wind farm case studies are presented; two onshore in the central United States, and one offshore in the New York Bight lease areas recently auctioned for wind energy development. The first case study demonstrates the inadequacy of standard engineering wake models to capture the magnitude of long-range external wake losses. With

that result as motivation, the second case study was used to demonstrate the utility of the WRF mesoscale model with the Wind Farm Parameterization (WFP) to model the wake impacts of distant external turbines more accurately than existing engineering wake models. WRF-WFP produced average external wake losses much closer to, 16% higher than, that derived from SCADA data. In contrast, two engineering wake loss models failed to come close to the actual wake loss deficit; these models under-predicted external wake losses as a small fraction, ⅓ or less, of that derived from SCADA data.

As a further demonstration of the capabilities of WRF-WFP, and to give a view into the potential for large project-to-project wake impacts in the recently auctioned New York Bight offshore lease areas, ArcVera presented a third offshore wind energy case study. ArcVera Renewables designed WRF-WFP simulations of hypothetical wind project turbine arrays that might be built in those areas approximately 5-10 years from today. The simulations were run for a set of 16 days, with winds from the prevailing southwesterly wind direction, selected to maximize the waking of arrays aligned in a southwest to northeast direction. The simulations produced dramatic hub-height project-scale wake swaths that extended over 50 km downwind, with a specific example showing a waked wind speed deficit of 7% extending 100 km downwind from the array of turbines that produced it. When averaged over the selected 16 simulation days, the energy loss at the target lease area due to external wakes from arrays to its southwest was 28.9%. While the 16-day result undoubtedly greatly exceeds the long-term external wake loss for winds from all directions, it is nonetheless illustrative of the potential for much greater external wake losses than have been accounted for in development planning for the New York Bight lease areas; and, as in the two onshore long-distance wake loss case studies, are much larger than engineering wake models predict for the same conditions.

The implications of this study of long-range wakes on the assessment of energy production (or shortfalls thereof) of existing and anticipated future wind farms is material and significant, as unexpectedly large impacts may well be present, and existing non-WRF-WFP-based engineering long-range wake loss methods are shown to be inadequate. The inadequacy of these models for long-distance wakes may be remedied in the future with further validation time-series modeling and concomitantly accurate assessment of time periods when atmospheric stability is high. Still larger implications are clear for long-term project valuation risk, the analysis and assessment of hybrid projects, battery usage risk, and around-the-clock reliable renewable energy power production. Offshore wind farms are equally strongly affected, and the extensive global plans for proximal deployment of offshore wind projects should account for such impacts.

REFERENCES

Archer, C. L., Wu, S., Ma, Y., & Jiménez, P. A., 2020: Two Corrections for Turbulent Kinetic Energy Generated by Wind Farms in the WRF Model. Mon. Wea. Rev., 148, 4823–4835, https://doi.org/10.1175/MWR-D-20-0097.1.

Brower, M. C., and N. M. Robinson, 2012: The Openwind Deep-Array Model—Development and Validation. AWS Truepower Report.

DOE SBIR Program U.S. Department of Energy. "United Industries Report No. 8701: Numerical Model for Predicting Turbine Array Performance in Complex Terrain, Phase 1." Washington D.C., 1987.

DOE SBIR Program U.S. Department of Energy. "United Industries Report No. 8917: Numerical Model for Predicting Turbine Array Performance in Complex Terrain, Phase 2: Final Technical Report." Washington D.C., 1990.

Djath, B., Schulz-Stellenfleth, J., and Cañadillas, B., 2018: Impact of atmospheric stability on X-band and C-band synthetic aperture radar imagery of offshore windpark wakes, J. Renew. Sustain. Ener., 10, 043301, https://doi.org/10.1063/1.5020437.

Fitch, A. C., Olson, J. B., Lundquist, J. K., Dudhia, J., Gupta, A. K., Michalakes, J., and Barstad, I., 2012: Local and Mesoscale Impacts of Wind Farms as Parameterized in a Mesoscale NWP Model, Mon. Weather Rev., 140, 3017–3038, https://doi.org/10.1175/MWRD-11-00352.1.

Hasager, C., P. Vincent, H. Vincent, R. Husson, A. Mouche, M. Badger, A. Peña, P. Volker, J. Badger, A Di Bella, A. Palomares, E. Cantero, P. Correia, 2015: Comparing satellite SAR and wind farm wake models. Journal of Physics: Conference Series. 625. 10.1088/1742-6596/625/1/012035.

Hersbach, H., and Coauthors, 2020: The ERA5 global reanalysis. Quart. J. Roy. Meteor. Soc., 146, 1999–2049, https://doi.org/10.1002/qj.3803.

Hirth, B. D., J. L. Schroeder,W. S. Gunter, and J. G. Guynes, 2012: Measuring a utility-scale turbine wake using the TTU Ka mobile research radars. J. Atmos. Oceanic Technol., 29, 766–771.

Jacobson, M. Z., and C. L. Archer, 2012: Saturation wind power potential and its implications for wind energy. Proc. Natl. Acad. Sci., 109(39), 15681.

Larsén, X.G., and J. Fischereit, 2021: A case study of wind farm effects using two wake parameterizations in the Weather Research and Forecasting (WRF) model (V3. 7.1) in the presence of low-level jets. Geoscientific Model Development, 14(6): 3141-3158.

Lee, J. C. Y., and Lundquist, J. K., 2017: Evaluation of the Wind Farm Parameterization in the Weather Research and Forecasting Model (Version 3.8.1) with meteorological and turbine power data, Geoscientific Model Development, 10, 4229–4244, https://doi.org/10.5194/gmd-10-4229-2017.

Mckay, P., R. Carriveau, D. S-K Ting, and T. Newson, 2012: Turbine Wake Dynamics. Advances in Wind Power: 65-84. INTECH. Web.

Nierenberg, R. and J. Kline, 1989: Macro-scale wake effects. WindStats Newsletter. Spring 1989. Vol. 2, No. 2, ISSN 0903-5648, 2 pp.

Nierenberg, R., 1989: Macro-scale wake effects. Windpower, 1989, San Francisco, CA, September, 9 pp.

Pielke, R. A., 1984: Mesoscale Meteorological Modeling. New York, N. Y.: Academic Press, 612 pp.

Platis, A., Siedersleben, S. K., Bange, J., Lampert, A., Baerfuss, K., Hankers, R., Canadillas, B., Foreman, R., Schulz-Stellenfleth, J., Djath, B., Neuman, T., and Emeis, S., 2018: First in situ evidence of wakes in the far field behind offshore wind farms, Sci. Rep., 8, 2163, https://doi.org/10.1038/s41598-018-20389-y.

Poulos, G. S., E. Jones, and J. Crescenti, 2022: Validation: Replacing wake loss modeling with wind farm-atmosphere interaction loss modeling. Journal of Energy in Southern Africa, August, 28 pp.

Pryor, S. C., R. J. Barthelmie, T. J. Shepherd, A. N. Hahmann, and O. M. Garcia Santiago, 2022: Wakes in and between very large offshore arrays. J. Phys.: Conf. Ser. 2265 022037

Rosencrans, D. J., J. K. Lundquist, M. Optis, and N. Bodini, 2022: Quantifying the uncertainty of wake impacts across the Atlantic outer continental shelf. 13th Conference on Weather, Climate, and the New Energy Economy. Houston, Texas, American Meteor. Soc. https://ams.confex.com/ams/102ANNUAL/meetingapp.cgi/Session/60432

Rybchuk, A., T. Juliano, J. Lundquist, D. Rosencrans, N. Bodini, M. Optis, 2021: The sensitivity of the Fitch wind farm parameterization to a three-dimensional planetary boundary layer scheme. 10.5194/wes-2021-127.

Siedersleben, S. K., Platis, A., Lundquist, J. K., Djath, B., Lampert, A., Bärfuss, K., Cañadillas, B., Schulz-Stellenfleth, J., Bange, J., Neumann, T., and Emeis, S., 2020: Turbulent kinetic energy over large offshore wind farms observed and simulated by the mesoscale model WRF (3.8.1), Geoscientific Model Development, 13, 249–268, https://doi.org/10.5194/gmd-13-249-2020.

Siedersleben, S. K., Platis, A., Lundquist, J. K., Lampert, A., Bärfuss, K., Cañadillas, B., Djath, B., Schulz-Stellenfleth, J., Bange, J., Neumann, T., and Emeis, S., 2018: Evaluation of a wind farm parametrization for mesoscale atmospheric flow models with aircraft measurements, Meteorol. Z., 27, 401–415, https://doi.org/10.1127/metz/2018/0900.

Skamarock, W. C., J. B. Klemp, J. Dudhia, D. O. Gill, Z. Liu, J. Berner, W. Wang, J. G. Powers, M. G. Duda, D. M. Barker, and X.-Y. Huang, 2019: A Description of the Advanced Research WRF Version 4. NCAR Tech. Note NCAR/TN-556+STR, 145 pp. doi:10.5065/1dfh-6p97.

Tomaszewski, J. M., and Lundquist, J. K., 2020: Simulated wind farm wake sensitivity to configuration choices in the Weather Research and Forecasting Model Version 3.8.1, Geoscientific Model Development, 13, 2645–2662, https://doi.org/10.5194/gmd-13-2645-2020.

Volker, P. J. H., J. Badger, A. N. Hahmann, and S. Ott, 2015: The Explicit Wake Parametrisation V1.0: a wind farm parametrisation in the mesoscale model WRF, Geosci. Model Dev., 8, 3715–3731, https://doi.org/10.5194/gmd-8-3715-2015, 2015.